Verifying and improving the estimation of NO_x-O_3 effects of aviation using Uncertainty Quantification (UQ) techniques

Rao, P.V.

DOI
10.4233/uuid:2ab0f5bd-b8cf-46b7-b56a-6606ec99c377

Publication date
2024

Document Version
Final published version

Citation (APA)
Rao, P. V. (2024). *Verifying and improving the estimation of NO_x-O_3 effects of aviation using Uncertainty Quantification (UQ) techniques*. [Dissertation (TU Delft), Delft University of Technology].
https://doi.org/10.4233/uuid:2ab0f5bd-b8cf-46b7-b56a-6606ec99c377

Important note
To cite this publication, please use the final published version (if applicable).
Please check the document version above.

Verifying and improving the estimation of NO_x-O_3 effects of aviation using Uncertainty Quantification (UQ) techniques

Verifying and improving the estimation of NO_x-O_3 effects of aviation using Uncertainty Quantification (UQ) techniques

Dissertation

for the purpose of obtaining the degree of doctor
at Delft University of Technology,
by the authority of Rector Magnificus prof. dr. T.H.J.J. van der Hagen,
chair of the Board for Doctorates,
to be publicly defended on,
Wednesday 16 October 2024 at 10:00 o'clock

by

Pratik Vijay Rao

Master of Science in Aerospace Engineering,
Delft University of Technology, Delft, the Netherlands,
born in Bangalore, India.

This dissertation has been approved by the promotors. I gratefully acknowledge their invaluable guidance for the completion of my research, with thanks to Dr. F. Yin (Delft University of Technology) for the supervision related to Chapters 3 and 4.

Composition of the doctoral committee:

Rector Magnificus,	chairperson
Prof. dr. V. Grewe,	Delft University of Technology German Aerospace Center (DLR), promotor
Dr. R.P. Dwight,	Delft University of Technology, promotor
Independent members:	
Prof. dr. T. Butler,	Freie Universität Berlin, Germany
Prof. dr. ing. V. Gollnick,	Technische Universität Hamburg, Germany
Dr. M. Soler,	Universidad Carlos III de Madrid, Spain
Prof. dr. G. D. Weymouth,	Delft University of Technology
Prof. dr. L. L. A. Vermeersen,	Delft University of Technology, reserve member

Keywords: Aviation, aircraft emissions, chemistry-climate models, surrogate models, uncertainty quantification, Gaussian processes

Printed by: ...

Front & Back: ...

ISBN ....

An electronic version of this dissertation is available at
http://repository.tudelft.nl/.

To my family, who probably will not read this.

Contents

Summary

Reducing anthropogenic climate change is a significant challenge requiring a global response to prevent tipping points in the climate system, such as the disintegration of ice sheets, and thawing of permafrost, among others. The rapidly growing air transport sector, which carried 4.5 billion passengers in 2019, is projected to emit nearly 2 Gt CO_2 by 2050—about 2.6 times the emissions in 2021. Decarbonising aviation is challenging due to its reliance on fossil fuels, and while technological, operational, and regulatory measures have reduced fuel consumption, they are insufficient to mitigate aviation's overall climate impact. The non-CO_2 effects are significant, accounting for about two-thirds of aviation's warming impact in terms of Effective Radiative Forcing (ERF). These effects include contrails, contrail-induced cirrus clouds, nitrogen oxides (NO_x), and water vapour emissions, collectively contributing to approximately 4% of anthropogenic forcing since the pre-industrial era. Given their spatio-temporal variability, climate-optimised flight planning can mitigate these impacts by avoiding sensitive regions, but this faces several challenges. These include the inherent chaos of weather, low scientific understanding of non-CO_2 effects, and the large computational expense of calculating sensitive regions using climate change functions (CCFs).

To address these issues, this thesis first analyses algorithmic climate change functions (aCCFs), a simple surrogate model obtained by regressing the CCFs against local atmospheric variables. The aCCFs are computationally inexpensive to run since they only use few meteorological inputs to estimate climate impact, enabling real-time flight trajectory optimisation on arbitrary days. However, aCCFs are applicable only in parts of the Northern Hemisphere and require thorough verification before implementation. The focus is narrowed down on local aviation NO_x effects on climate change, which largely causes warming via short-term increase in tropospheric ozone (O_3) and is characterised by large variability. This necessitates a detailed investigation of NO_x-O_3 effects in isolation and its mitigation, which is a previously unexplored area. After verifying the O_3 aCCFs through complex climate-chemistry model simulations, it is concluded that while it enables a reasonable first estimate, there are a few discrepancies.

The O_3 aCCFs are replaced by using a more comprehensive dataset comprising global NO_x-O_3 impacts, identifying additional physical variables that influence this impact, and using this information to train stochastic surrogates based on homoscedastic and heteroscedastic Gaussian processes. These models provide mean and uncertainty estimates for the climate impact of NO_x on O_3, for the first time. The heteroscedastic model more accurately reproduces the data distribution and its ease of use in predicting the climate impact of individual flights is demonstrated. Defined as probabilistic aCCFs (paCCFs), these models demonstrate superior accuracy over aCCFs, provide valuable insights for aviation's non-CO_2 effects, and offer broader implications for climate-optimised flight planning. The thesis concludes with limitations and recommendations to further mitigate aviation's environmental impact.

Samenvatting

Het terugdringen van antropogene klimaatverandering is een belangrijke uitdaging die een wereldwijde reactie vereist om omslagpunten in het klimaatsysteem te voorkomen, zoals het uiteenvallen van ijskappen en het ontdooien van permafrost. De snel groeiende luchtvaartsector, die in 2019 4,5 miljard passagiers vervoerde, zal tegen 2050 naar verwachting bijna 2 Gt CO_2 uitstoten - ongeveer 2,6 keer zoveel als in 2021. Het koolstofvrij maken van de luchtvaart is een uitdaging vanwege de afhankelijkheid van fossiele brandstoffen, en hoewel technologische, operationele en regelgevende maatregelen het brandstofverbruik hebben teruggedrongen, zijn ze onvoldoende om de algemene impact van de luchtvaart op het klimaat te beperken. De niet-CO_2 -effecten zijn aanzienlijk en zijn goed voor ongeveer tweederde van het effect van de luchtvaart op de opwarming in termen van Effectieve Stralingsforcering (ERF). Deze effecten omvatten contrails, door contrails veroorzaakte cirruswolken, stikstofoxiden (NO_x) en waterdampemissies, die gezamenlijk bijdragen aan ongeveer 4% van de antropogene forcering sinds het pre-industriële tijdperk. Gezien hun variabiliteit in ruimte en tijd kan een voor het klimaat geoptimaliseerde vluchtplanning deze effecten beperken door gevoelige gebieden te vermijden, maar dit gaat gepaard met verschillende uitdagingen. Deze uitdagingen zijn onder andere de inherente chaos van het weer, het geringe wetenschappelijke inzicht in niet-CO_2 effecten en de grote rekenkosten voor het berekenen van gevoelige gebieden met behulp van klimaat verandering functies (CCF's).

Om deze problemen aan te pakken, worden in dit proefschrift eerst algoritmische klimaat verandering functies (aCCF's) geanalyseerd, een eenvoudig surrogaatmodel dat wordt verkregen door de CCF's te regresseren tegen lokale atmosferische variabelen. De aCCF's zijn computationeel goedkoop om uit te voeren omdat ze slechts enkele meteorologische inputs gebruiken om de klimaatimpact te schatten, waardoor vluchttrajectoptimalisatie in realtime op willekeurige dagen mogelijk is. De aCCF's zijn echter alleen toepasbaar in delen van het noordelijk halfrond en moeten grondig worden geverifieerd voordat ze kunnen worden geïmplementeerd. De nadruk ligt op lokale NO_x-effecten van de luchtvaart op klimaatverandering, die grotendeels opwarming veroorzaken via een kortdurende toename van troposferisch ozon (O_3) en gekenmerkt worden door een grote variabiliteit. Daarom is een gedetailleerd onderzoek nodig naar de geïsoleerde NO_x-O_3-effecten en de beperking ervan, een gebied dat tot nu toe nog niet is verkend. Na verificatie van de O_3 aCCF's door middel van complexe klimaatchemische modelsimulaties, wordt geconcludeerd dat het weliswaar een redelijke eerste schatting mogelijk maakt, maar dat er enkele discrepanties zijn.

De O_3 aCCF's worden vervangen door gebruik te maken van een uitgebreidere dataset met wereldwijde NO_x-O_3 effecten, aanvullende fysische variabelen te identificeren die deze invloed beïnvloeden en deze informatie te gebruiken om stochastische surrogaten te trainen op basis van homoscedastische en heteroscedastische Gaussische processen. Deze modellen geven voor het eerst gemiddelde en onzekerheidsschattingen

voor de klimaatimpact van NO_x op O_3. Het heteroscedastische model reproduceert de gegevensverdeling nauwkeuriger en het gebruiksgemak ervan bij het voorspellen van de klimaatimpact van individuele vluchten wordt aangetoond. Deze modellen, probabilistische aCCF's (paCCF's) genoemd, tonen een grotere nauwkeurigheid dan aCCF's, bieden waardevolle inzichten in de niet-CO_2 effecten van de luchtvaart en bieden bredere implicaties voor een voor het klimaat geoptimaliseerde vluchtplanning. Het proefschrift sluit af met beperkingen en aanbevelingen om de milieueffecten van de luchtvaart verder te beperken.

1

Introduction

Philosophers of the world have only interpreted the world in various ways.
The point, however, is to change it.

Karl Marx

1

1.1. Greenhouse gas emissions and their climate impact

Greenhouse gases absorb and re-emit terrestrial infrared radiation from the earth, thereby trapping heat in the atmosphere and preventing a bulk of it going into space. Without this natural greenhouse effect, the earth's average temperature would be below freezing levels and therefore render itself uninhabitable for most species. However, with the advent of the industrial revolution from the mid 18th century in Great Britain, continental Europe, and the United States of America, there has been a precipitous rise in greenhouse gas emissions as there was a transformation from agrarian to industrial society. The main sources of greenhouse gases are (the burning of) fossil fuels for transportation, heating, and electricity; animal agriculture; cement production; land-use changes; and forestry. The concentrations of greenhouse gases in 2005 were reported to be much higher than any time during the preceding 650,000 years [1]. Between 2011-2020, the global surface temperature reached 1.1°C above 1850-1900 levels due to the continued increase of emissions, with unequal historical and ongoing contributions arising from unsustainable energy-use, lifestyles, consumption and production patterns across regions, between and within countries, and among a small percentage of individuals [2]. In 2019, the richest 1% of people were responsible for as much global carbon emissions as the poorest 66% [3]. These increases in greenhouse gases trap greater amounts of heat, and are causing the atmosphere and oceans to grow dangerously warmer over time by increasing the frequency and intensity of hot extremes, floods and droughts induced by changing precipitation patterns, and storms[4]. These events are an existential threat to existing and future biodiversity. Strong global cooperation and systemic change based on eco-socialist principles is paramount [5–7] in order to avoid tipping points in the climate system such as the disintegration of the Greenland and Antarctic ice sheets, thawing of Permafrost, die-back of the Amazon rainforest, etc. [8]. As of November 2023, the current status with respect to climate change is shown in Fig. 1.1, taken from the Copernicus website. This indicates that global warming is expected to reach 1.5° by 2034, without sharp and consistent reductions in emissions.

1.2. Comparing different greenhouse gases: the role of climate metrics

In order to mitigate the impact of climate change, various technical, operational and political measures are necessary. The potential of climate mitigation methods such as generating energy from alternative sources (nuclear, solar, wind, geothermal energy, etc.), use of electric vehicles, climate-friendly aircraft, and less climate-intensive agriculture need to be measured. This is where climate metrics become convenient; they can be used to translate emissions in terms of kg per year to a parameter relevant to climate change such as the change in global mean surface temperature, change in sea levels or frequency of extreme weather events. The simplest climate metric used is the total mass of an individual emission, but this is not very useful for comparing it with other emitted species. For instance, the impact from 1 ton of methane (CH_4) differs from 1 ton of water vapour (H_2O). Thus, another climate metric, called equivalent CO_2 emissions or CO_2-eq is required to put these different species on the same scale. For this example, 1 (metric) ton of CH_4 and H_2O can be converted to CO_2-eq. Here, this means the

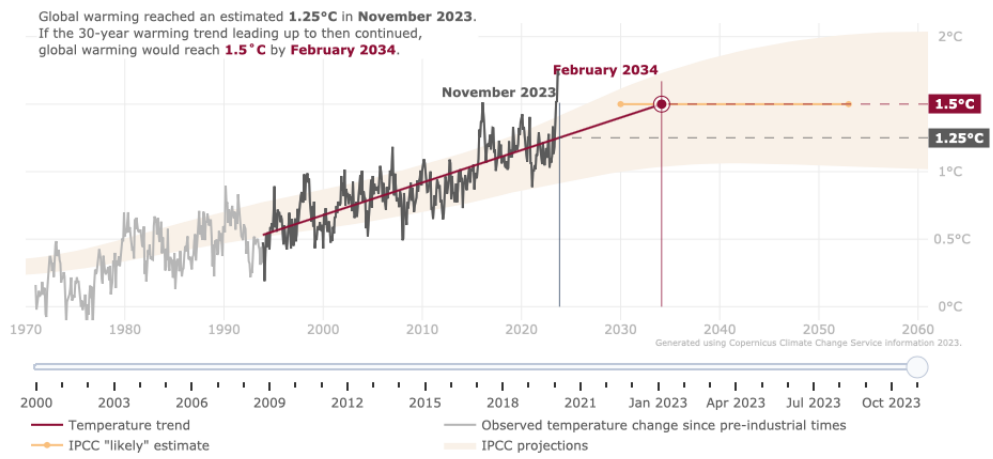

Figure 1.1: Reaching 1.5°C of global warming as per the Paris agreement is closer than anticipated, falling short of the Paris agreement [9].

number of tons of CO_2 emissions with the same global warming potential (GWP, see Section 1.2) as 1 ton of CH_4 and H_2O. To obtain the GWP, one requires to calculate radiative forcing (RF, see Section 1.2), which measures the radiation change as a result of the change in concentration of emissions relative to (say) pre-industrial atmosphere, and is significant in the field of climate science. RF is used as a base metric, to compute other climate metrics such as GWP, Global Temperature Potential (GTP) and Average Temperature Response (ATR) over a chosen time horizon, to overcome other limitations [10]. The question one would like to answer defines an emission scenario, the choice of a climate metric, and to some extent, the time horizon [11]. It is difficult to agree upon a single metric in a legislative framework [12], and the development of a suitable metric for short-lived species (non-CO_2 effects) is certainly a major challenge [13]. As will be clear later, a significant part of this dissertation pertains to the general class of non-CO_2 effects of aviation and analysing an operational measure called climate optimised-flight planning using the ATR over a time horizon of 20 years as the appropriate climate metric [14]. Ultimately, the integral aspect of any assessment study is to determine the possible damage based on the chosen climate metric in terms of welfare and monetary costs, but these are characterised by higher uncertainties as shown in Fig. 1.2.

1.3. Aviation's contribution to climate change

Aviation contributed to 3.5% of anthropogenic climate change in terms of effective radiative forcing (Section 2.1.3.1) in 2018 and the climate impact is expected to grow rapidly due to the growth of the air transport sector in most regions of the world [15]. The impact of the COVID-19 pandemic was only temporary [16] and the demand for air travel is already recovering. There is a strong case to abate the climate impact of aviation and that requires a thorough understanding of how aircraft emissions impact the environ-

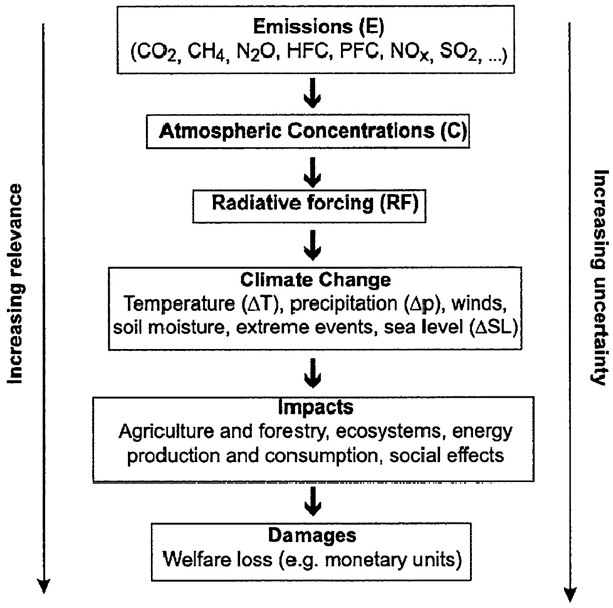

Figure 1.2: Increasing relevance down the chain is characterised by increasing uncertainty [10].

ment via CO_2 and non-CO_2 effects before the implementation of effective policies. The latter include contributions from water vapour (H_2O) [17, 18], nitrogen oxides (NO_x = NO + NO_2) [19–22], sulphur oxides (SO_x) [23], aerosols such as soot [24, 25], sulphates [26] and lastly via the formation of contrails [27, 28]. The climate impact of the major aviation emissions and effects as a result of direct emissions from fuel combustion are shown in Fig. 1.3. These include CO_2 which contributes to warming, NO_x which contributes to net warming by inducing an increase in O_3 in the short term and decrease in CH_4 in the long-term. The decrease in CH_4 also reduces O_3 in the long term which is called primary mode ozone (PMO), and decreases the amount of stratospheric water vapour (SWV). Additionally, H_2O and aerosols have a direct and indirect impact on the radiative balance. The indirect impact is via contrails, which produce net warming. With respect to aerosols, soot has a warming effect while sulphates have a cooling effect but the net impact is cooling. Collectively, these non-CO_2 effects from aviation have been found to contribute to nearly 70% of the total climate impact from aviation, but have not been addressed in international agreements such as the Paris climate agreement [29, 30].

The climate impact of CO_2 is dependent on the quantity of CO_2 released in the atmosphere and since CO_2 is a long-lived and relatively well-mixed gas, the impact is independent of the emission location. Additionally, the climate impact of CO_2 has been determined with a high confidence level. On the contrary, emitted non-CO_2 species and contrail cirrus have shorter atmospheric residence times and are not well-mixed in the atmosphere. For each non-CO_2 emission, it is not just the quantity that is important but also the location of the emission, the associated timescale, chemical background condition, etc. [31–33]. Consequently, the confidence levels are much lower and associated

uncertainties are much higher for these non-CO_2 effects. Because non-CO_2 effects show strong spatial and temporal variations, the weather situation and subsequent transport pathways play a major role in their climate impact.

There are a number of technical and operational measures to mitigate the impact of aviation. The former includes improved aerodynamics for aircraft (blended-wing-body design), efficient engines, the use of sustainable fuel, and hydrogen or battery powered aircraft. Many of these measures are a long way from being conceived, making the pursuance of operational measures crucial along with a general reduction in the number of flights. Some suggested operational measures include more direct flights, intermediate-stop operations for long-haul flights, sustainable ground operations, efficient flight profiles, and climate-optimised flight-planning. Conventionally, flight trajectories are optimised with respect to economic costs which primarily include reduction in flight time and fuel burnt by taking advantage of e.g. tail winds. On the other hand, climate-optimised trajectories involve flying in regions where aviation emissions have lower climate impact. Various studies e.g., [34, 35] investigated the effect of carefully assessing the relation between a change in altitude and the consequent net climate impact. Other studies have evaluated the possibilities of applying climate-optimised routing for real flight data. Matthes [36] and Sridhar *et al.* [37] addressed weather-dependent trajectory optimisation using real flight routes and showed that it has a large climate mitigation potential. On the other hand, Grewe *et al.* [38] optimised flight trajectories based on avoiding climate sensitive regions [39] and showed that large reductions in the climate impact of up to 25% can be achieved by only a small increase in economic costs of less than 0.5 %, but these are not based on real flight data. In a similar manner, a couple of studies e.g., [40, 41] investigated the mitigation of contrail impact in particular, but no studies assessed the mitigation of local aviation NO_x warming via ozone (O_3) formation in isolation. Since this is the second largest contributor to warming in aviation, this dissertation is primarily motivated by this aspect.

1.4. Algorithmic climate change functions (aCCFs)

The climate impact of non-CO_2 effects from aviation is strongly dependent on location, such that climate impact can potentially be reduced by strategic routing of flights. The climate effect of an aviation emission at a location may be summarised by a single Climate Change Function (CCF) representing a global ATR over a defined time horizon e.g., 20 years, measured in K/kg emitted or K/km contrail coverage [33, 39]. Essentially, the CCFs indicate where aviation emissions have a larger impact on climate change in comparison to other regions. The CCF depends on the species, local weather pattern, chemical background, and spatio-temporal location of the emission, and is obtained using high-fidelity chemistry-climate model simulations. Once CCFs are calculated at predefined locations, they may be used as inputs for air traffic optimisation, such that climate sensitive regions may be avoided as shown in [38]. Although the mitigation potential in this particular study is promising, the computational expense of calculating CCFs makes real-time calculations unfeasible, rendering operational application impractical. This issue is circumvented by using algorithmic climate change functions (aCCFs, [42]), a simple surrogate model that provides approximate estimates of the global climate impact from local aviation emissions and effects (CO_2, NO_x, H_2O, and contrails). The aC-

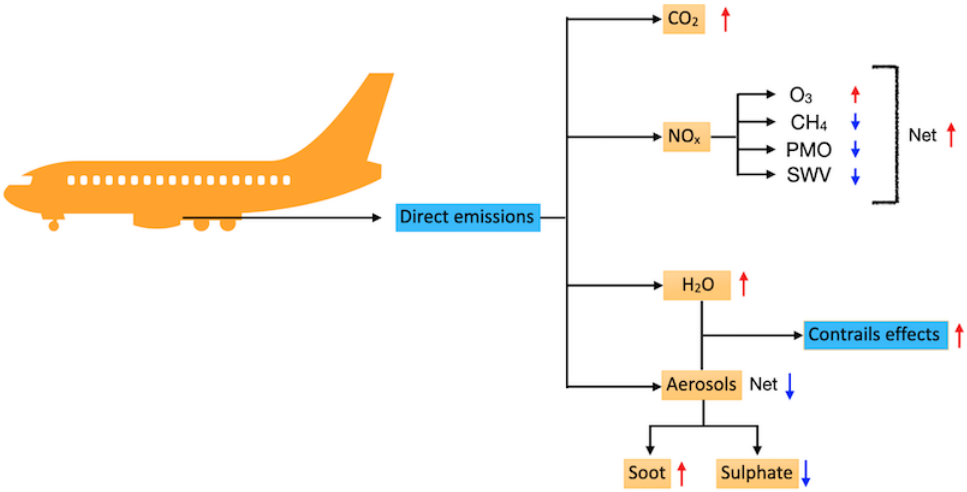

Figure 1.3: The climate impact of aviation from jet fuel combustion. The red and blue arrows indicate warming and cooling effects, respectively. Nitrogen oxide (NO_x) emissions from aviation increase O_3 in the short-term and decrease CH_4 concentrations. The latter results in a decrease of O_3 in the long-term (PMO), and a reduction in stratospheric water vapour (SWV). The net impact is still significant warming. Water vapour (H_2O) and aerosols from aviation also impact climate change directly and via contrail formation and persistence.

CFs were formulated by regressing the CCF data with weather variables as predictor variables, which enables real-time prediction of climate impact using instantaneous forecast data. The adjusted regression coefficients [43], which is used as a proxy to demonstrate the effectiveness of the aCCFs in representing the CCFs, are 0.59, 0.42, and 0.17 for H_2O, NO_x-O_3, and NO_x-CH_4, respectively. The findings indicate that the meteorological conditions at the time of emission predominantly influence the fate of the emitted species, with the quality of the aCCF diminishing as the lifetime of the respective species increases. Currently, the aCCFs are available as a submodel called ACCF [14] in a climate modelling framework called Modular Earth Submodel System (MESSy) [44]. In this dissertation, the focus is on verifying NO_x-O_3 aCCFs for air traffic optimisation and subsequently, its replacement with probabilistic algorithmic climate change functions (paCCFs) based on heteroscedastic Gaussian processes. The paCCFs concept is more accurate than the aCCFs and enables climate impact estimation along with the associated confidence interval. This also makes it useful to measure risks involved with re-routing and contributes towards the forthcoming EU-wide Monitoring, Reporting, and Verifying (MRV) initiative, targeting non-CO_2 aviation impacts.

1.5. Research questions and dissertation structure

The present dissertation has the goal of verifying and improving the estimation of NO_x-O_3 effects of aviation using Uncertainty Quantification (UQ) techniques. The ACCF submodel enables the prediction of the climate impact of aviation emissions and effects (CO_2, NO_x, H_2O, contrails) using weather forecast data. Climate-optimised planning, in

the context of this work, is associated with predicting climate-sensitive regions associated with aviation NO_x-O_3 impacts and avoiding them to minimise the climate impact of trajectories. For instance, emitting NO_x at specific locations can transport the species to regions where the subsequent climate impact via O_3 formation is much lower. Here, the ability of the aCCFs in predicting NO_x-O_3 impacts is verified, and the limitations are identified, before building a more accurate model, based on stochastic principles that in addition, offer uncertainty estimates in predictions.

This dissertation thus aims to provide answers to the following main research question, which can be broken down into two sub-questions:

How effective is the prediction of aviation's climate impact in real-time to enable climate-optimised flight planning?

(i) *Are algorithmic climate change functions (aCCFs) a reliable tool for predicting and abating aviation's climate impact?*

(ii) *What kind of uncertainty quantification (UQ) techniques are conducive to improving this predictive power?*

In order to provide the necessary background and answer these questions, the dissertation is divided into six chapters and the structure is presented in Fig. 1.4.

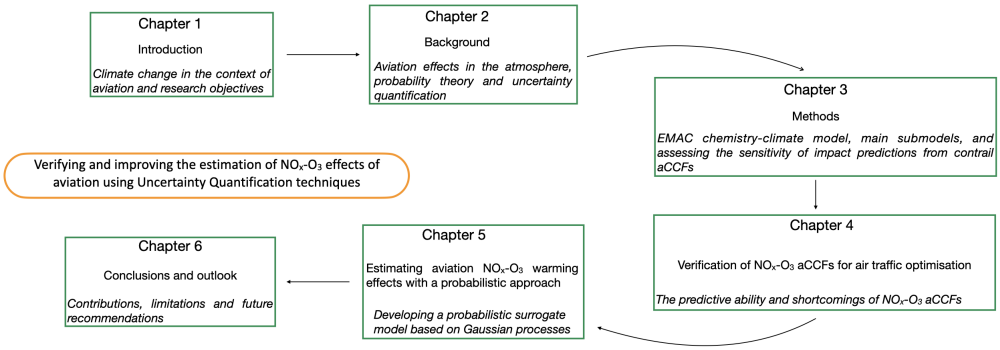

Figure 1.4: Overview of dissertation

The chapters of this dissertation deal with the following: Chapter 2 provides the required background required to carry out the research in this dissertation. It entails the discussion of the climate effects of aviation, uncertainty quantification, essentials of probability theory, and, deterministic and stochastic surrogate modelling. Chapter 3 deals with the used climate modelling framework, discussion of the global chemistry-climate model EMAC, the modular framework of submodels, the aCCFs, the analysis of the sensitivity of contrail aCCFs to meteorological conditions in the prediction of contrail impact, and the derivation of a simple temperature correction term. Chapter 4 tests the validity of existing NO_x-O_3 aCCFs for climate-optimised flight planning via complex

simulations on EMAC. Chapter 5 uses the most comprehensive dataset on global aviation NO_x impacts on O_3, and develops and evaluates a new surrogate model based on stochastic principles for the prediction of short-term NO_x-O_3 effects in terms of instantaneous radiative forcing measured at the tropopause. This model is called probabilistic algorithmic climate change functions (paCCFs) and serves as a replacement for NO_x-O_3 aCCFs. Lastly, chapter 6 offers a brief summary of the dissertation, the gaps in the research, and future recommendations.

2

Background

Never regard your study as a duty, but as the enviable opportunity to learn the liberating beauty of the intellect for your own personal joy and for the profit of the community to which your later work will belong.

Albert Einstein

2.1. Aviation and the atmosphere

The Earth's climate system comprises a complex framework of five key interacting components, namely, the atmosphere (gases), hydrosphere (water bodies), cryosphere (ice and permafrost), lithosphere (earth's outer crust) and biosphere (living species). Climate can be defined as the mean and variability of weather variables such as temperature, humidity, precipitation, etc. typically over a time span of 30 years. The Sun is the main driver for Earth's climate by providing energy in the form of electromagnetic radiation and for the Earth's temperature to be stable, there has to be a balance between the influx of energy and the outflux to space. The climate system can change due to natural processes within the interacting components and external forcings. These external forcings can be natural, such as variations in solar intensity and volcanic eruptions, or caused by the anthropogenic release of greenhouse gases and aerosols. The speed at which various components of the climate system react to these forcings is different and the perturbation will propagate to adjacent systems, driving the earth's climate system to a new state of equilibrium. These interactions between various systems are complex, and beyond the scope of the present work. This chapter is primarily motivated by the influence of aviation emissions within the atmosphere, and provides the necessary background for the reader.

2.1.1. The atmosphere

The Earth's atmosphere is a complex and dynamic envelope of gases that surrounds the Earth's surface, held in place by gravity, and plays a crucial role in supporting life and regulating the planet's climate. It is primarily composed of nitrogen (about 78%) and oxygen (about 21%), with trace amounts of other gases such as carbon dioxide, argon, and water vapour. Aerosols and particulate matter are also present in minute quantities, but play an important role in the climate system by consequence of influencing chemical reactions, and processes such as condensation and radiation scattering. The air temperature is determined by the incoming solar radiation and other physical processes related to heat transfer. The atmosphere extends several hundred kilometers above the Earth's surface and consists of four distinct layers based on temperature variations with altitude. Figure 2.1 depicts the vertical temperature profile as defined by the International Standard Atmosphere (ISA) at a typical mid-latitude. The troposphere, which is closest to the Earth's surface, is characterised by meteorological events and contains the majority of the atmosphere's mass (80%). Air traffic occurs mainly in the upper troposphere and lower tropopause, which is the boundary between the troposphere and the next layer, the stratosphere. As one ascends through the stratosphere, mesosphere, thermosphere, and exosphere, temperatures and atmospheric composition change. The temperature (T) in the troposphere generally decreases with increase in altitude (h) with an average lapse rate ($\mathrm{d}T/\mathrm{d}h$) of -6.5° C/km until reaching the tropopause. The tropopause has a nearly constant (average) temperature of -58°C and is a stable layer that prevents most of the vertical mixing of air masses between troposphere and stratosphere [45]. Although some ozone is present in the troposphere, and contributes to warming along with CO_2 and water vapour, close to 90% of ozone lies in the stratosphere, forming a layer and absorbing harmful solar UV radiation. Thus, the stratosphere is heated from above, predominantly by ozone, while the troposphere is heated from below, predominantly by

water vapour. In the mesosphere, temperature decreases again with altitude due to a reduced absorption of solar radiation from above, and limited heat transfer from below as the density of molecules in this layer is relatively low. The temperature rises once again from the lower levels of the thermosphere due to the absorption of solar radiation at the top of the atmosphere. Furthermore, this absorbed energy gets rapidly redistributed throughout the layer due to molecular collisions and the dissociation and ionisation of atmospheric constituents. Excluding the thermosphere, the highest temperatures are seen at the top of the stratosphere and at the bottom of the troposphere (ground level).

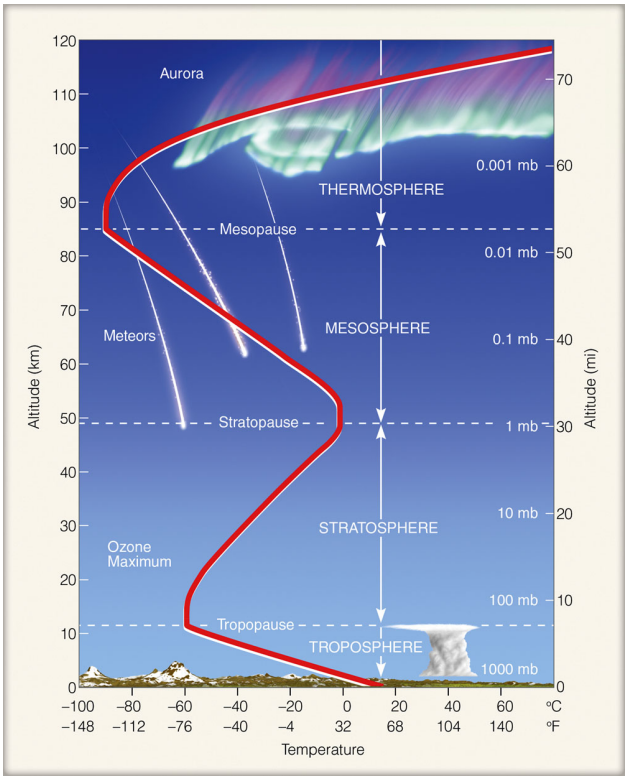

Figure 2.1: The structure of the atmosphere and the variation of air temperature, taken from https://ghsearth.weebly.com/atmosphere.html (last accessed on 23rd February 2024).

2.1.2. Global energy budget of the climate system

The Sun is the primary source of energy on Earth. On average, the Earth receives 341 W/m^2 of energy at the top of atmosphere, but only part of it heats the Earth's surface. Solar radiation from the sun consists mainly of visible light (44%), near-infrared (37%), and ultraviolet (7%), whereas Earth's radiation is predominantly far-infrared [46]. Some of the incoming solar radiation is reflected back to space, while some of it is absorbed and re-emitted by the atmosphere and the Earth's surface. The radiation balance or the energy budget of the Earth system is the algebraic sum of the incoming and outgoing

components of radiation, as depicted in Fig. 2.2. Major parts of the short-wave radiation are reflected directly by clouds or by parts of the Earth's surface (snow and ice cover) while a significant portion is absorbed by the atmosphere. Incoming radiation contrasts with surface long-wave outgoing radiation of around 396 W/m^2. Via convection and evapo-transpiration, the surface releases an additional 100 W/m^2, potentially leading to a negative energy balance for the surface, assuming the absence of the greenhouse effect. This effect, induced by gases like water vapour, CO_2, CH_4, etc., and other trace gases, leads to approximately 333 W/m^2 of infrared back-radiation. This establishes an energy balance, maintaining a global mean surface temperature of approximately 14 °C. These components are balanced over long-time periods without which the Earth would be continually cooling or warming. However, over shorter periods of time, radiant energy is unequally distributed. For instance, during 2005 to 2019, the Earth's energy imbalance averaged about 0.90 ± 0.15 W/m^2 globally [47].

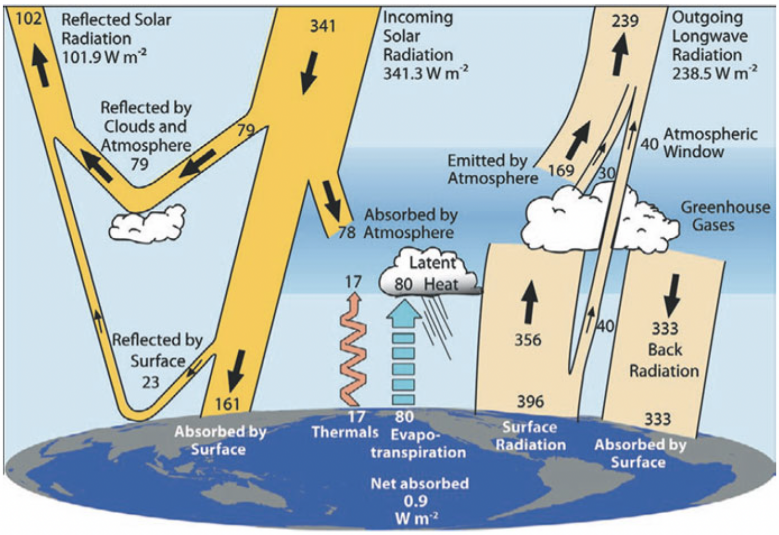

Figure 2.2: Global energy fluxes associated with the radiation balance of the Earth. Taken from Trenberth *et al.* [48].

2.1.3. Climate effects of aviation

Radiative forcing and climate impacts

Air traffic climate impact results either from the direct emission of greenhouse gases (GHGs), the influence of emissions on the amount of GHGs or the formation of contrails and contrail cirrus or the modification of natural cloud cover. All of these effects alter the Earth's radiation budget, which triggers a new equilibrium surface temperature and thus influences global climate. Radiative forcing (RF) is defined as a change imposed on the earth's radiation balance, measured by the net radiative flux change, at some level in the atmosphere calculated to occurring response to the perturbation which may be a change due to natural conditions (e.g., incident solar radiation, planetary surface properties) or

anthropogenic conditions (e.g. atmospheric concentration changes of GHGs). The net radiative flux change ΔF at an atmospheric level is given by,

$$\Delta F = \left[\left(\tilde{F}^{\downarrow}_{SW} - \tilde{F}^{\uparrow}_{SW} + \tilde{F}^{\downarrow}_{LW} - \tilde{F}^{\uparrow}_{LW}\right) - \left(F^{\downarrow}_{SW} - F^{\uparrow}_{SW} + F^{\downarrow}_{LW} - F^{\uparrow}_{LW}\right)\right] .$$

Here, $\tilde{F}$ and F represent the perturbed and the initial radiative fluxes respectively and vary in (x, y, t). The subscripts SW and LW are short-wave and long-wave fluxes and the arrows $\uparrow, \downarrow$ indicate whether the flux is upward or downward. The RF is then commonly expressed as the global annual mean of ΔF,

$$\mathrm{RF} = \frac{1}{V} \int_{\text{year}} \iint_{\text{globe}} \Delta F \, \mathrm{d}x \, \mathrm{d}y \, \mathrm{d}t \, ,$$

where V is the total integration volume measured as the product of the surface area of the globe and the duration of a year, in seconds. A positive RF leads to warming and a negative RF leads to cooling in terms of the steady-state surface temperature change. The RF concept helps in comparing the influence of forcing agents on this temperature change (Figure 2.3). There are various definitions of RF in use, as shown in Figure 2.3, but they all quantify the global mean radiative imbalance following a perturbation before the atmosphere returns to a new equilibrium. Each definition is characterised by a calculation procedure, with every subsequent one serving as an improved revision. The simplest definition (Figure 2.3 a) measures the instantaneous flux change at the climatological tropopause following a perturbation while keeping all atmospheric variables fixed, and is defined as instantaneous RF. A more accurate measure (Figure 2.3 b) called stratospheric adjusted RF involves allowing the stratospheric temperature to adjust to the presence of the perturbation without changes in tropospheric variables and stratospheric dynamics [49]. This definition is more accurate, as the timescale for the stratosphere to adjust is relatively short (few months). Effective radiative forcing (ERF) includes rapid adjustments of the Earth's surface and troposphere, and serves as a more accurate metric for quantifying climate response [8]. Here, the entire atmosphere is allowed to adjust by either fixing the global mean surface temperature (Figure 2.3 c) or the ocean temperature (Figure 2.3 d) and calculating the net flux change at the top of the atmosphere (TOA). For GHGs, the ERF and RF are similar, and thus RF may be used to ease the computational burden. However, for aerosols, ERF and RF differ significantly owing to their influence on albedo (snow, sea ice and clouds), and the former should be used.

There is an approximately linear relationship between the global mean radiative forcing (RF) from a perturbation and a change in global mean surface temperature ($\Delta \mathrm{T}_s$) when the system has reached a new equilibrium,

$$\Delta \mathrm{T}_s = \lambda \cdot \mathrm{RF} \, ,$$

where λ is the climate sensitivity parameter [K m^2/W], and comprises the impact of radiative feedbacks within the climate system. The feedbacks are positive, if they amplify the initial effect of the perturbation, and negative is they dampen it. This value is

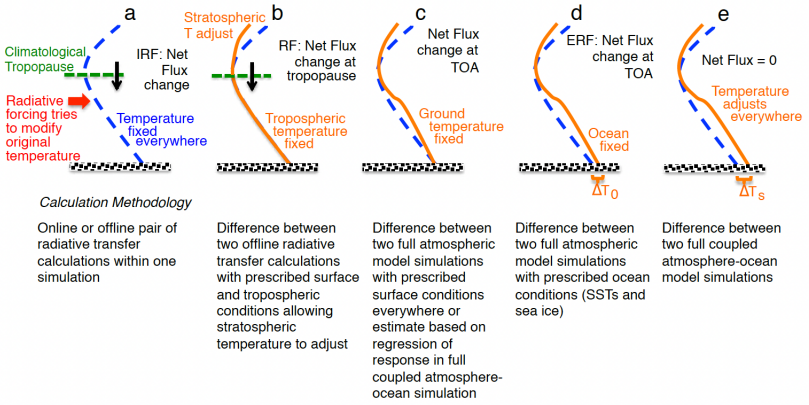

Figure 2.3: Comparing various definitions for RF: (a) instantaneous RF, (b) stratospheric adjusted RF, (c) flux change when the surface temperature is fixed, enabling a calculation of ERF, (d) ERF allowing atmosphere and land temperature to adjust while keeping ocean conditions such as Sea Surface Temperature (SST) and sea ice fixed, and (e) the equilibrium response to the perturbation. The methodology for calculating each RF is highlighted. ΔT_0 represents land temperature response while ΔT_s represents the temperature response of Earth's entire surface. This figure is taken from IPCC [8], which is adapted from Hansen [50].

model specific and stable but within the kind of forcing considered [15]. Thus, it is not a physical law, but an empirical relation. This concept works well for well mixed GHGs such as CO_2 and CH_4, but is more difficult for species such as O_3, since it is highly dependent on the location of the perturbation. These perturbations may have a stronger or weaker impact on global temperature change as shown in various studies e.g., [50–52]. The IPCC report [8] shows that for a doubling of CO_2, the mean value of $\lambda = 1.0 \pm 0.5$ K/Wm^2, based on roughly 30 climate model studies. To account for variations from other climate forcing agents, the efficacy concept is useful [50] and is defined as $r_i = \lambda_i / \lambda_{CO_2}$. For any forcing agent, i, we have,

$$\Delta T_s^i = r_i \cdot \lambda_{CO_2} \cdot \mathrm{RF}\,.$$

This implies that r_i and RF can be independently used to describe the same perturbation, and both of these have to be determined to calculate ΔT_s^i . Efficacies which can only be calculated by running numerous simulations with complex climate models have been suggested for the climate impact of aviation [53, 54]. The RF provides a meaningful shortcut to estimate global mean surface temperature change, but it is a backward looking metric, since it provides the net radiation change relative to e.g., pre-industrial times resulting from concentration change due to past emissions. The RF concept can also be used as a basis to formulate other climate metrics that may be more useful. A climate metric is obtained by combining the three ingredients of emission evolution, time horizon, and climate indicator (defined below).

1. Global Warming Potential (GWP) of a forcing agent i, can be expressed relative to CO_2 or in absolute terms (A) and is defined over a time horizon H in the future, as

[10]:

$$\mathrm{AGWP}_i(H) = \int_0^H \mathrm{RF}_i(t)\,\mathrm{d}t\,, \qquad \mathrm{GWP}_i(H) = \frac{\mathrm{AGWP}_i(H)}{\mathrm{AGWP}_{\mathrm{CO_2}}(H)}\,.$$

Since the RF is integrated over a time horizon, typically 20, 50, and 100 years, the (A)GWP is less dependent on time horizon compared to RF. However, it does not take the climate sensitivity into account, and is thus not directly related to temperature change. Also, while it may be used for long-lived emissions, it is not suitable for short-lived emissions [55]. This metric has been used before in e.g., the Kyoto protocol.

2. Global Temperature Potential (GTP) of a forcing agent i, can be expressed relative to CO_2 or in absolute terms (A) and quantifies temperature change at a time horizon H. It is thus, an endpoint climate metric [56]:

$$\mathrm{AGTP}_i(H) = \int_0^H \mathrm{RF}_i(t)\,\mathcal{G}(H-t)\,\mathrm{d}t\,, \qquad \mathrm{GTP}_i(H) = \frac{\mathrm{AGTP}_i(H)}{\mathrm{AGTP}_{\mathrm{CO_2}}(H)}\,.$$

Here, $\mathcal{G}(H-t)$ is a response function that yields the surface temperature response at time H due to the radiative forcing at time t. The response function for a simplified climate model with three parameters including climate sensitivity λ, the time scale of the climate response τ, and the heat capacity of the climate system C, such that $\tau = C\lambda$. For this model, $\mathcal{G}(H-t) = \frac{1}{C}\exp\left(\frac{t-H}{\lambda C}\right)$, and a closed form solution exists for AGTP_i. While this metric takes the climate sensitivity into account, and thus has a link to temperature change, it is sensitive to the chosen time horizon.

3. Average Temperature Response (ATR) is the mean temperature change induced by a forcing agent i, over a time horizon H:

$$\mathrm{ATR}_i(H) = \frac{1}{H}\int_0^H \Delta T_i(t)\,\mathrm{d}t\,.$$

The ATR is less dependent on the time horizon and includes climate sensitivities and thermal inertia of the climate system, thereby combining the advantages of GWP and GTP [57]. ATR has not been used in any current climate policies yet, but has been extensively used by various institutions for aviation related climate impact.

Aviation emissions and effects

Kerosene is the dominant fuel used for civil aviation. During its combustion with ambient air in the jet engine, CO_2, H_2O along with a host of traces gases such as nitrogen oxides (NO_x), SO_2, CO, hydrocarbons, and soot particles are released. The H_2O is also a precursor for the production of contrails and contrail induced cirrus clouds. This combination of CO_2 and non-CO_2 contributions lead to significant net warming. Lee *et al.* [52] attributes a net ERF of 100.9 mW/m^2 in 2018 based on emissions from 1940, when all contributions are considered, as shown in Fig. 2.5. Aviation contributions are complex to quantify since it involves a range of atmospheric processes including transport, chemical reactions, microphysics, and radiation.

1. Carbon dioxide (CO_2)

   CO_2 is transparent to visible light but absorbs and re-emits terrestrial infrared radiation, making it a greenhouse gas, and has a residence time of several centuries. The long residence time is attributed to low chemical reactivity, which prevents it from being a part of important conversion and reduction processes. The natural removal processes including uptake from oceans and plants occurs on long time scales. For a pulse emission of CO_2, it takes about 30 years for 50% removal, a few centuries for a further 30% removal, while the rest remains in the atmosphere for many thousand years [58]. Around 3160 g of CO_2 is released per kg of fuel burnt [59] for complete combustion. CO_2 is a well mixed and relatively non-reactive gas, so its release location is unimportant, it is the quantity that counts. More importantly, the impact of CO_2 is well-understood and has been assigned a 'very high' level of confidence in its contribution to net anthropogenic forcing [8]. From aviation itself, Lee *et al.* [52] provides an ERF estimate of 34.3 mW/m^2 in 2018 considering emissions since 1940 with a high confidence level. For non-CO_2 effects, the confidence level in general is low.

2. Nitrogen oxides (NO_x)

   The most abundant byproducts of jet fuel combustion in terms of nitrogen (N) containing compounds are nitric oxide (NO) and nitrogen dioxide (NO_2). This mixture of NO and NO_2 is represented as NO_x and the lifetime ranges from a few hours to weeks, but is highly reactive. NO_x indirectly contributes to climate change via the formation of ozone (O_3) and the destruction of methane (CH_4). The former leads to warming, while the latter leads to cooling (i.e., reduced warming). Subsequently, the reduction in CH_4 due to NO_x, which is a precursor for O_3, leads to a decrease in background O_3, which is called Primary Mode Ozone (PMO) [60] and entails a cooling effect. Additionally, a smaller amount of CH_4 enters the stratosphere and it decomposes to CO_2 and H_2O. There is a reduced amount of stratospheric water vapour (SWV), resulting in net cooling [61]. However, the net climate effect for this chain of reactions is warming [62–64] and was found to have an ERF estimate of 17.5 mW/m^2 from 1940 to 2018 [52], characterised with a low confidence level. The lifetime of the O_3 perturbation is for a few weeks, but the CH_4 and PMO perturbations have a lifetime of about 12 years. The short term warming effect from O_3 production dominates resulting in net warming from aviation NO_x, and is more dependent on emission location than the other impacts. These effects are discussed further in Section 2.1.3.3. The effects of NO_x are non-linear and exhibit a clear seasonal, altitudinal, and latitudinal dependence.

3. Water vapour (H_2O)

   Water vapour is mostly a natural greenhouse gas and predominantly a part of the water cycle. The atmospheric lifetime of H_2O increases with altitude, ranging from several hours to days in the troposphere to few months in the lower stratosphere. H_2O is also released during complete combustion of jet fuel and has a short mean residence time of 8 to 10 days for subsonic flights [65]. The additional amount of H_2O emitted from combustion is negligible in comparison and has a small warm-

ing contribution to the total aviation impact. However, if supersonic flights are considered in the future, this would involve the emission of H_2O at high altitudes and can significantly perturb the (dry) stratosphere, where it can have a lifetime up to few months [31] and causing significant warming [55]. The RF resulting from emitted H_2O depends on both, the background concentration of H_2O as well as the lifetime, which increases with altitude [55].In 2018, the ERF estimate for stratospheric H_2O was found to be 2 mW/m^2 with a medium confidence level.

4. Contrail cirrus

   Contrails or condensation trails are line-like ice clouds formed in the exhaust and the wake of aircraft at cruise levels. These trails are formed due to the combination of the warm water vapour from the jet exhaust and the cold dry ambient air at high altitudes transiently achieving saturation with respect to liquid water. If 100% relative humidity is reached as a result of the mixing, droplets are formed and they freeze if the atmospheric threshold temperature (T_c) is low enough ($< -38°C$). Subsequently, the persistence of these contrails occurs if the ambient air is ice-supersaturated. The Schmidt-Appleman Criterion (SAC) [66, 67] predicts the *formation* of contrails based on thermodynamic principles associated with T_c, pressure, specific fuel energy content, propulsion efficiency of the jet engine and water vapour emissions. Here, the mixing process between the exhaust and ambient air is assumed to take place isobarically. Figure 2.4 shows a $T-e$ graph, where T is the absolute temperature and e is the partial pressure of water vapour in the mixture. Here, the mixing phase trajectory appears as a straight line due to the isobaric assumption. The slope of the phase trajectory, G [Pa/K], can be shown to be [68],

$$G = \frac{\mathrm{EI}_{\mathrm{H_2O}}\, p\, c_p}{\epsilon\, Q\, (1-\eta)},$$

   where $\mathrm{EI}_{\mathrm{H_2O}}$ is the emission index of H_2O representing the mass of emitted water vapour per unit of burnt jet fuel, p [Pa] is the ambient air pressure, c_p [J/(kg K)] is the isobaric heat capacity of air, ϵ is the molar mass ratio of water vapour and dry air, Q [MJ/kg] is the specific fuel energy content, and η is the overall propulsion efficiency.

   For aircraft with modern engines and higher propulsion efficiency, T_c is higher, implying that contrails can form over a larger range of cruise altitudes [70]. Most contrails have a short atmospheric lifetime from few minutes to hours but under conditions of ice-supersaturation, they persist, mix with other contrails or cirrus clouds, and increase the cloudiness. The transition to contrail cirrus has a lifetime of about 18 hours [71]. In 2018, the ERF estimate for contrail cirrus in high-humidity regions was found to be 57.4 mW/m^2 with a low confidence level. Contrails can have a cooling effect by reflecting short-wave radiation during the day and a warming effect by trapping long-wave infrared radiation at night.

5. Aerosols

   An aerosol is a liquid or solid atmospheric particle other than water and ice and few examples include soot, sulphates, nitrates and pollen. They are commonly

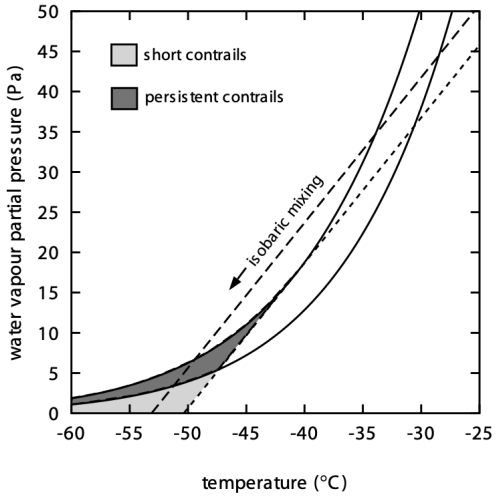

Figure 2.4: SAC criterion for contrail formation. The upper solid curve represents saturation with respect to liquid water while the lower curve is with respect to ice. The phase trajectory of the mixing of exhaust gases and the ambient air is a straight dashed line (from upper right to lower left) in the e-T diagram. The trajectory tangent to the water saturation curve (small dashed line) marks the warmest temperatures for which contrail formation is possible. If the trajectory reaches an ice-supersaturated state, persistent contrails will form and could spread into contrail cirrus. If not, contrails live only for a few minutes. Taken from Gierens *et al.* [69].

characterised by their size, chemical composition, mass-concentration, number density, etc and have an atmospheric residence time of about 1-2 weeks in the troposphere. Aircraft engines directly emit soot (solid particles) and precursors for sulphate and nitrate along flight tracks via engine fuel combustion. Both, soot and sulphates have an impact ob the radiative budget and come under the term aerosol-radiation interactions. Soot has low albedo and absorbs short-wave solar radiation resulting in net warming, while sulphate aerosols scatter this radiation, leading to net cooling [55] but the estimates are characterised by high uncertainties [52]. Furthermore, aerosols also impact cloud formation, and are termed aerosol-cloud interactions. Sulphate aerosols from aviation act as cloud condensation nuclei for low-altitude liquid clouds in a homogeneous manner and likely have a net cooling effect. On the other hand, the effect of soot particles on cloud physics is even more uncertain because of both homogeneous and heterogeneous ice nucleation, and a general lack of knowledge regarding the ice nucleating ability. In both instances, ice crystals and cloud droplets nucleate on aerosol particles, leading to changing cloud microphysics and potentially impacting the radiative effects of clouds, which is hard to measure accurately. In general, aerosol-cloud interactions contribute the largest uncertainty in estimating the radiative forcing [8, 52].

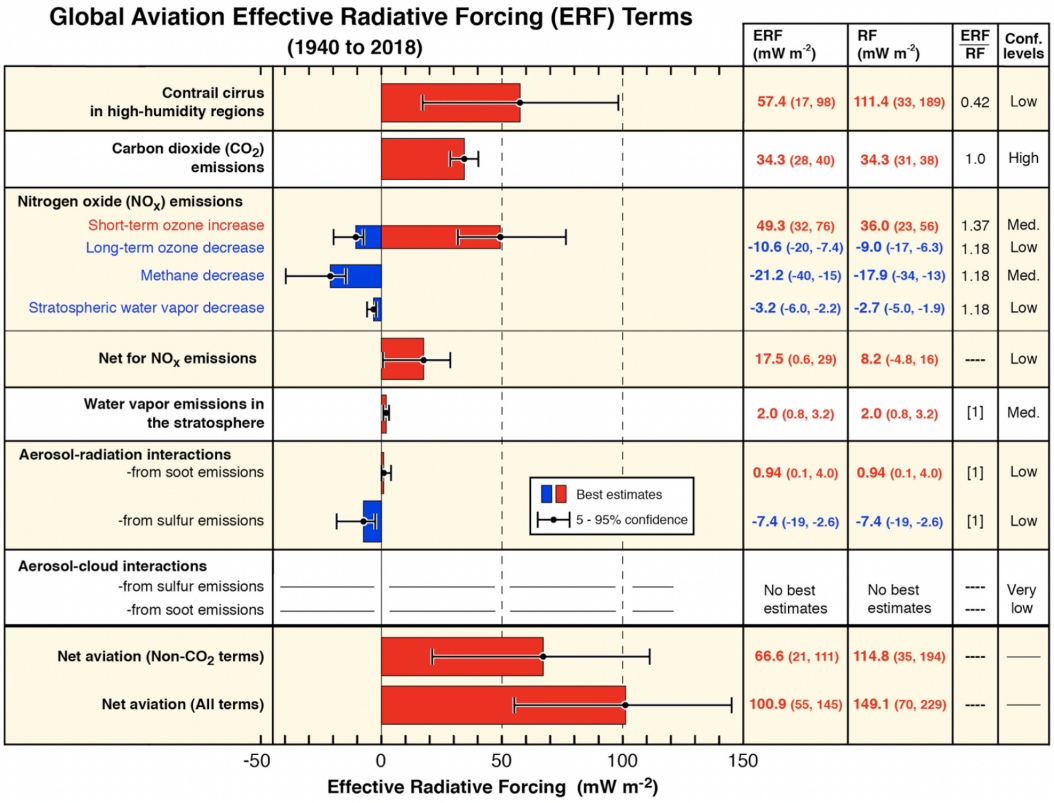

Figure 2.5: Best-estimates for effective radiative forcing in 2018 from global aviation emissions and effects. The figure is taken from Lee *et al.* [52].

NO_x-O_3 effects

The focus of this dissertation lies predominantly aviation's NO_x-O_3 effects and this is discussed here in more detail. Cruise aviation releases both NO and NO_2, and due to their close interconnection by formation at high temperatures, they are commonly grouped together under the term, nitrogen oxides (NO_x). The NO_x-O_3 chemistry is complex due to various interacting chemical reactions occurring on different time scales and influenced by background concentrations of various chemical species. NO_x from subsonic aviation is released in the troposphere and behaves as catalyst for O_3 formation through an increased oxidation of predominantly ambient carbon monoxide (CO) as shown in reaction 2.R1:

$$CO + OH + O_2 \rightarrow HO_2 + CO_2 \tag{2.R1}$$

$$NO + HO_2 \rightarrow NO_2 + OH \tag{2.R2}$$

Through photolysis of NO_2 in reaction 2.R3 at wavelengths < 424 nm, oxygen radical O is formed, which in turn reacts with O_2 to form O_3 (In reaction 2.R4):

$$NO_2 \xrightarrow{h\nu} NO + O \tag{2.R3}$$

$$O + O_2 \rightarrow O_3 \tag{2.R4}$$

The O_3 is in turn partly depleted by NO, resulting in NO_2:

$$O_3 + NO \rightarrow NO_2 + O_2 \tag{2.R5}$$

The reactions 2.R3, 2.R4, and 2.R5 form a cyclical process in which O_3 is continuously produced and depleted. During the day, NO_2 undergoes photolysis to create O_3, but during the night, no O_3 is produced. As a result, reaction 2.R5 almost depletes NO completely during the night. Additionally, O_3 loss occurs when it reacts with NO_2, resulting in the formation of nitrate (NO_3):

$$O_3 + NO_2 \rightarrow NO_3 + O_2 \tag{2.R6}$$

Thus, during night time, O_3 concentrations decrease while NO_2 and NO_3 increases due to reactions 2.R5 and 2.R6. Additionally, O_3 loss also occurs via reactions with hydrogen oxides (HO_x):

$$O_3 + OH \rightarrow HO_2 + O_2 \tag{2.R7}$$

$$O_3 + HO_2 \rightarrow OH + 2O_2 \tag{2.R8}$$

The reaction rates for O_3 formation depend on background concentration of NO_x and HO_x on latitude and altitude [55]. NO_x concentration varies considerably in the atmosphere. For example, for regions where NO_x concentration exceeds 0.2 to 0.3 nmol/nmol, O_3 formation rate decreases due to the formation of nitric acid (HNO_3) and peroxynitric acid (HNO_4) [72]:

$$NO_2 + OH \rightarrow HNO_3 \tag{2.R9}$$

$$NO_2 + HO_2 \rightarrow HNO_4 \tag{2.R10}$$

The unstable HNO_4 gets decomposed to HNO_3, which is washed off as acid rain. The formed O_3 triggered by Eq. (2.R2) is a precursor for OH. This enhancement of OH result in a depletion of CH_4. For additional details, the reader is referred to Grewe [73] and Rosanka *et al.* [74] and Figure 2.6, where the main chemical mechanisms surrounding changes in O_3 and CH_4 in the troposphere are depicted. The NO_x effects are characterised by significant seasonal and spatial variability due to the dependence on incoming solar radiation and background chemical (especially NO_x) concentrations [75]. Frömming *et al.* [33] found that not only the emission region is relevant; in fact, the main driver for the enhanced climate sensitivity is the transport pathways of emissions within the first week(s) after emissions are released. The transport pathways are in turn driven by the meteorological situation. The detailed impact of weather patterns and related transport processes on aviation's contribution to O_3 is also reported by Rosanka *et al.* [74]. Lee *et al.* [52] provides an ERF estimate of 49.3 mW/m^2 in 2018 for the short-term O_3 increase from global aviation. Aviation NO_x-O_3 chemistry is clearly non-linear and depends on several factors, as discussed here. Predicting these effects accurately is a major challenge that can be taken on using uncertainty quantification techniques that are suitable in climate modelling, which will be discussed in subsequent sections.

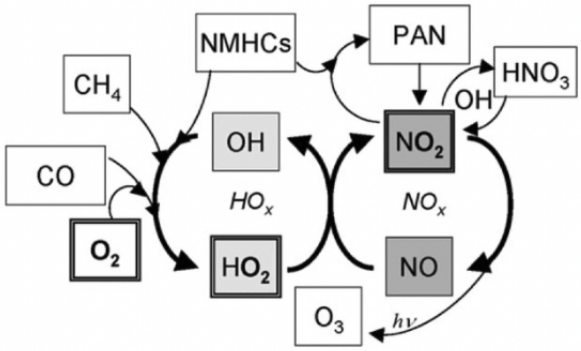

Figure 2.6: Scheme of the main tropospheric chemical mechanism influencing O_3. NMHC are non-methane hydrocarbons, PAN is peroxyacetyl nitrate, which serves as a reservoir for NO_x. Taken from Grewe [73].

2.2. Uncertainty quantification

Uncertainty quantification (UQ) is a broad field of study that focuses on quantifying and managing uncertainty in mathematical models, simulations, and observations from experiments. It involves assessing and characterising uncertainties arising from various sources, such as input data, model parameters, and numerical approximations using random variables. The primary goal of UQ is to provide a more complete understanding

of the limitations of our approach in predicting a particular Quantity of Interest (QoI), depending on the application under study. In the context of climate modelling, the QoI can be e.g., radiative forcing, average surface temperature change, sea level rise, etc. Its use is motivated by much needed improvements in predicting the climate impact from aviation and this is achieved by focusing on numerical and statistical methods. Thus, some background is first provided on probability theory (Appendix A) and surrogate modelling before stating its application in this dissertation.

2.2.1. Surrogate modelling

When a certain QoI is not readily available, or expensive to compute, an approximate model or surrogate can be used to emulate this quantity. Consider a limited number of samples of $\{y_i | i = 1, \ldots, n\}$, obtained from a black box or simulation code $f(\boldsymbol{\theta})$, dependent on the feature vector $\boldsymbol{\theta} \in \mathbb{R}^p$. Since f is expensive to run, we would like to construct a surrogate $\hat{f}(\boldsymbol{x})$, using the available samples with the help of a reduced feature space $\boldsymbol{x} \in \mathbb{R}^m$, where $m < p$. Ideally, a surrogate should be able to predict unseen data reasonably well; or in other words, it should generalise well. The task of constructing a surrogate to make a *quantitative* prediction (e.g. expected precipitation for an arbitrary weather forecast) and *qualitative* prediction (e.g. classifying whether a given image is that of a horse or pony) is called regression and classification, respectively. In this dissertation, we deal with regression.

Frequentist linear regression

Given a set of n data pairs $\mathcal{D} = \{(\boldsymbol{x}_i, y_i) | i = 1, \ldots, n\}$, we look for the *optimal linear* function $\hat{f}$ that can best reproduce observations y from f. To generate a linear function of $\boldsymbol{x}_i$ containing m predictors, we would need $(m+1)$ parameters,

$$\hat{f}(\boldsymbol{x}_i; \hat{\boldsymbol{w}}) = \boldsymbol{x}_i^\top \hat{\boldsymbol{w}}, \quad y_i = \hat{f}(\boldsymbol{x}_i) + \varepsilon_i, \tag{2.11}$$

where $\hat{\boldsymbol{w}} \in \mathbb{R}^{m+1}$ is a vector of parameters which includes an intercept term (called bias) and m slopes. Thus, the input vector $\boldsymbol{x}_i \in \mathbb{R}^{m+1}$, where an additional element of value one is included for m features. We assume that each observation deviates from $\hat{f}(\boldsymbol{x}_i)$ by additive Gaussian noise $\varepsilon_i \sim \mathcal{N}(0, \sigma_n^2)$ that is iid. For these parameters to be optimal, we choose the least squares approach, which minimises the residual sum of squares,

$$\hat{\boldsymbol{w}} = \arg\min_{\boldsymbol{w}} [\mathrm{RSS}(\boldsymbol{w})] = \arg\min_{\boldsymbol{w}} \left[\sum_{i=1}^{n} \left(y_i - \boldsymbol{x}_i^\top \boldsymbol{w} \right)^2 \right].$$

Since $\mathrm{RSS}(\boldsymbol{w})$ is a convex function of $\boldsymbol{w}$, a minimum always exists and it can be shown that,

$$\hat{\boldsymbol{w}} = (X^\top X)^{-1} X^\top \boldsymbol{y}.$$

where X is the design matrix $\in \mathbb{R}^{n \times (m+1)}$ and $\boldsymbol{y} \in \mathbb{R}^n$ is the vector of observations, obtained by combining the n cases. Thus we can denote the dataset as $\mathcal{D} = (X, \boldsymbol{y})$. For any new test vector $\boldsymbol{x}_*$, the constructed linear regression surrogate offers new predictions $\hat{f}(\boldsymbol{x}_*)$ using the parameters $\hat{\boldsymbol{w}}$ that were optimal for the original data. Note that this surrogate is deterministic.

Bayesian linear regression

The Bayesian approach to linear regression assumes an initial probability distribution over the parameters $\boldsymbol{w}$, called prior or hypothesis. It is denoted by $\rho(\boldsymbol{w})$ and is representative of what is known about $\boldsymbol{w}$ before looking at the data. The likelihood is the probability distribution of the data, given the parameters, $\rho(\boldsymbol{y}|X,\boldsymbol{w})$. This is obtained by using the statistical model $\forall\ y_i$, which is part of Eq. (2.11). Finally, the posterior is the updated probability distribution of the parameters, after looking at the data, which is obtained using Bayes' theorem (Appendix A.1.5),

$$\rho(\boldsymbol{w}|X,\mathbf{y}) = \frac{\rho(\boldsymbol{w})\,\rho(\boldsymbol{y}|X,\boldsymbol{w})}{\rho(\boldsymbol{y}|X)} = \frac{\rho(\boldsymbol{w})\,\rho(\boldsymbol{y}|X,\boldsymbol{w})}{\int_{\boldsymbol{w}}\rho(\boldsymbol{w})\,\rho(\boldsymbol{y}|X,\boldsymbol{w})\,\mathrm{d}\boldsymbol{w}}\ . \tag{2.12}$$

When not much is known about $\boldsymbol{w}$ before hand, we can make an assumption, $\rho(\boldsymbol{w}) = \mathcal{N}(\boldsymbol{\mu}_p, \Sigma_p)$. The likelihood can be calculated as,

$$\begin{aligned}\rho(\boldsymbol{y}|X,\boldsymbol{w}) &= \prod_{i=1}^{n}\rho(y_i|\boldsymbol{x}_i,\boldsymbol{w}) = \prod_{i=1}^{n}\frac{1}{\sigma_n\sqrt{2\pi}}\exp\left(-\frac{(y_i-\boldsymbol{x}_i^\top\boldsymbol{w})^2}{2\sigma_n^2}\right)\\ &= \frac{1}{(2\pi\sigma_n^2)}\exp\left(-\frac{1}{2\sigma_n^2}|\boldsymbol{y}-X^\top\boldsymbol{w}|^2\right) = \mathcal{N}\left(X^\top\boldsymbol{w},\Sigma_l\right)\ .\end{aligned}$$

Here, the likelihood factorises over all n cases since we have assumed that the observations are independent. Also, the covariance matrix of the likelihood, $\Sigma_l = \sigma_n^2 I$. For a Gaussian prior and Gaussian likelihood, the posterior is also Gaussian and determined using Eq. (2.12). It simplifies to,

$$\rho(\boldsymbol{w}|X,\boldsymbol{y}) = \mathcal{N}\left(\hat{\boldsymbol{\mu}},\hat{\Sigma}\right), \tag{2.13}$$

with posterior mean, $\hat{\boldsymbol{\mu}} = \boldsymbol{\mu}_p + K(\boldsymbol{y} - X\boldsymbol{\mu}_p)$ and posterior covariance, $\hat{\Sigma} = (I-KX)\,\Sigma_p$ where $K = \Sigma_p X^\top\left(\Sigma_l + X\Sigma_p X^\top\right)^{-1}$ is called the Kalman gain matrix. The posterior mean is also called the Maximum a posteriori (MAP) estimate of $\boldsymbol{w}$ [76]. To make predictions $\hat{f}_* := \hat{f}(\boldsymbol{x}_*)$ for any new test case, we average over all possible parameter predictive distribution values, weighted by their posterior probability,

$$\rho(\hat{f}_*|X,\boldsymbol{x}_*,\boldsymbol{y}) = \int_{\boldsymbol{w}}\rho(\hat{f}_*|\boldsymbol{x}_*,\boldsymbol{w})\rho(\boldsymbol{w}|X,\boldsymbol{y})\,\mathrm{d}\boldsymbol{w} = \mathcal{N}\left(\boldsymbol{x}_*^\top\hat{\boldsymbol{\mu}},\boldsymbol{x}_*^\top\hat{\Sigma}\boldsymbol{x}_*\right). \tag{2.14}$$

Now, samples can be taken from Eq. (2.14) or the posterior mean estimate may be used.

Example

Consider 100 noisy samples generated from two true functions $f(x) = 3x+4$ and $g(x) = 3x^2 + x$ where $x \in [0,3]$. The noise is assumed to be Gaussian with $\varepsilon \sim \mathcal{N}(0,1)$. Here, we use 80% of the samples for training the frequentist (least squares) and Bayesian linear regression models and predictions are made on 20% of the remaining data. Fig. 2.7 visually compares the two models for a linear ground truth (Fig. 2.7a) and a quadratic ground truth (Fig. 2.7b). The posterior mean is similar to the least squares prediction qualitatively and quantitatively (similar R^2 values) in both cases. In the Bayesian approach,

there is an entire distribution from which samples can be taken and Fig. 2.7 shows 1000 of them (in grey).

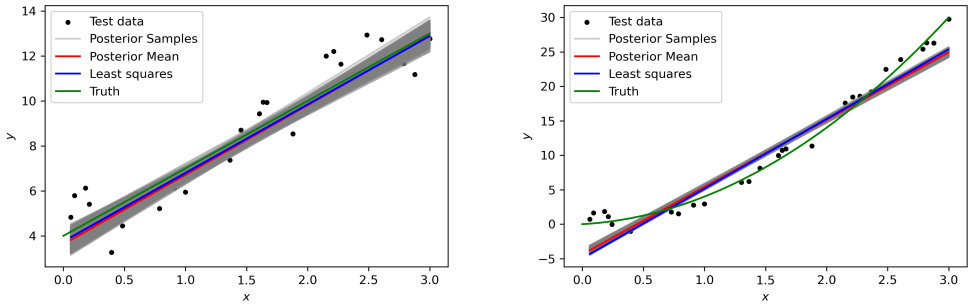

(a) (b)

Figure 2.7: Comparing the two linear regression models for **(a)** a linear ground truth, $f(x)$, and **(b)** a quadratic ground truth, $g(x)$.

Gaussian process regression

In linear regression, a finite set of parameters, $\boldsymbol{w}$, are used to find an optimal linear relationship between the data and the features. Once these parameters are determined, future predictions are independent of the observed data, $P(\hat{f}_*|\boldsymbol{w},\mathcal{D}) = P(\hat{f}_*|\boldsymbol{w})$. Non-parametric surrogates assume that the data distribution cannot be defined in terms of such a finite set of parameters. But they can often be defined by assuming an infinite dimensional $\boldsymbol{w}$, which can be thought of as a function. The number of parameters used in the model increases, as the amount of data increases, making them flexible in capturing non-linear trends. The parameters and data points are intrinsically linked to each other, thus future predictions from the underlying model are dependent on the observed data, $P(\hat{f}_*|\boldsymbol{w},\mathcal{D}) \neq P(\hat{f}_*|\boldsymbol{w})$. Gaussian process regression (GPR) models belong to the class of non-parametric models with the key assumption that the underlying function f that generates the data is a Gaussian process (GP).

Definition 2.2.1 (Random process)**.** A random process is a collection $Y = \{Y_x : x \in T\}$ of random variables, all of which are defined on the same probability space $(\Omega, \mathcal{F}, P)$, indexed over a set $T \subset \mathbb{R}$, and take up values on a function space S.

An example of a random process is a GP in which, any subset of the collection of random variables has a joint Gaussian distribution. Analogous to Gaussian distributions, a Gaussian Process $f(\boldsymbol{x})$ is characterised by a mean function, $\mu(\boldsymbol{x})$ (taken to be zero, here) and a covariance or kernel function, $k(\boldsymbol{x},\boldsymbol{x'})$. In order to use it in a Bayesian framework, a prior is defined as,

$$p(\boldsymbol{f}) = \mathcal{N}\left(\mu(\boldsymbol{x}), k(\boldsymbol{x},\boldsymbol{x'})\right),$$

with $\boldsymbol{f} := f(\boldsymbol{x})$ and the kernel function computes the covariance between pairs of

random variables such that the generated covariance matrix K is positive semi-definite. Here, we use the squared exponential kernel,

$$k(\boldsymbol{x}, \boldsymbol{x'}) = \sigma_k^2 \exp\left(-\frac{1}{2}\sum_{j=1}^{m}\frac{|x_j - x'_j|^2}{l_j^2}\right), \tag{2.15}$$

where σ_k^2 represents the overall variance of the function, and $\boldsymbol{l} = \{l_j\}_{j=1}^m \in \mathbb{R}^m$ is the length scale, which informally represents the distance to move in the feature space for a significant change in function values. They are both termed as hyperparameters of the kernel. Samples, i.e., functions drawn from this GP, will be smooth and infinitely differentiable with characteristics based on the hyperparameters. Given a set of training data, the prior distribution $\rho(\boldsymbol{f})$ is updated using Bayes' theorem to obtain a posterior distribution $\rho(\boldsymbol{f}|\mathcal{D})$ over the space of possible functions that is conditioned on the observed data. This posterior distribution represents the updated belief about the true function that generated the data, and we can make a new prediction y_* for unobserved inputs $\boldsymbol{x}_*$, using the posterior predictive distribution $\rho(y_*|\mathcal{D}, \boldsymbol{x}_*)$. First, the pdf of observations $\boldsymbol{y}$ and test prediction y_* is Gaussian,

$$\rho(\boldsymbol{y}, y_*|X, \boldsymbol{x}_*) = \mathcal{N}\left(\begin{bmatrix}\mu(X)\\ \mu(\boldsymbol{x}_*)\end{bmatrix}, \begin{bmatrix}K(X,X)+\sigma_n^2 I & K(X,\boldsymbol{x}_*)\\ K(\boldsymbol{x}_*,X) & K(\boldsymbol{x}_*,\boldsymbol{x}_*)+\sigma_n^2 I\end{bmatrix}\right).$$

Conditioning this on $\boldsymbol{y}$, we get the posterior predictive distribution which is Gaussian,

$$\rho(y_*|\boldsymbol{y}, X, \boldsymbol{x}_*) \equiv \rho(y_*|\mathcal{D}, \boldsymbol{x}_*) = \mathcal{N}(\tilde{\mu}(\boldsymbol{x}_*), \tilde{\Sigma}(\boldsymbol{x}_*)), \quad \text{where,} \tag{2.16}$$

$$\tilde{\mu}(\boldsymbol{x}_*) = \mu(\boldsymbol{x}_*) + K(\boldsymbol{x}_*, X)\left(K(X,X)+\sigma_n^2 I\right)^{-1}\left(\boldsymbol{y} - \mu(X)\right), \tag{2.17}$$

$$\tilde{\Sigma}(\boldsymbol{x}_*) = K(\boldsymbol{x}_*,\boldsymbol{x}_*) - K(\boldsymbol{x}_*, X)\left(K(X,X)+\sigma_n^2 I\right)^{-1} K(X,\boldsymbol{x}_*) + \sigma_n^2 I, \tag{2.18}$$

The hyperparameters $\boldsymbol{\theta}$ can be either be chosen arbitrarily, or using the ARD approach [77] assigns values to each input dimension, and are optimised during the training process by minimising the negative log marginal likelihood,

$$\boldsymbol{\theta}_{\text{opt}} = \underset{\boldsymbol{\theta}=\{\sigma_k^2, \boldsymbol{l}, \sigma_n^2\}}{\arg\min}\left[-\log\left(\rho(\boldsymbol{y}|X,\boldsymbol{\theta})\right)\right] = \underset{\boldsymbol{\theta}}{\arg\min}\left[\frac{1}{2}\left(\boldsymbol{y}-\mu(X)\right)^T K_y^{-1}\left(\boldsymbol{y}-\mu(X)\right) + \frac{1}{2}\log|K_y| + \frac{n}{2}\log 2\pi\right], \tag{2.19}$$

where $K_y = K(X,X) + \sigma_n^2 I$ and the data noise σ_n^2 is also estimated as a hyperparameter. Solving Eq. (2.19) involves computing $K_y^{-1} \in \mathbb{R}^{n\times n}$ which requires $\mathcal{O}\left(n^3\right)$ time and gradients which require $\mathcal{O}\left(n^2\right)$ time for each θ_i, making it advantageous to use gradient-based optimisers. The L-BFGS-B algorithm [78] is used to solve this optimisation problem and the aforementioned procedure is implemented using a machine learning library called Scikit learn (version 1.2.1, [79]). The optimization algorithm yields the hyperparameters $\boldsymbol{\theta}_{\text{opt}}$ and features with large length scales can be discarded.

Example

Consider 100 noisy samples generated from a true function $f(x) = x\sin(x)+\cos(x)$ where $x \in [0, 10]$. The noise is assumed to be Gaussian with $\varepsilon \sim \mathcal{N}(0, 1)$. Here, we consider two cases: a) using 10% of the samples for training, and b) using 80% of the samples for training a GPR model. Predictions are made over x as shown in Fig. 2.8 for the two cases. The posterior mean is much closer to the truth when 80% rather than 20% the noisy data is used for training. Also, the 95% confidence interval is much narrower and this is logical because the model can predict with greater confidence in the presence of more data. Thus, the predictive power of GPR is evident, especially when there is a non-linear trend between the input and output variable.

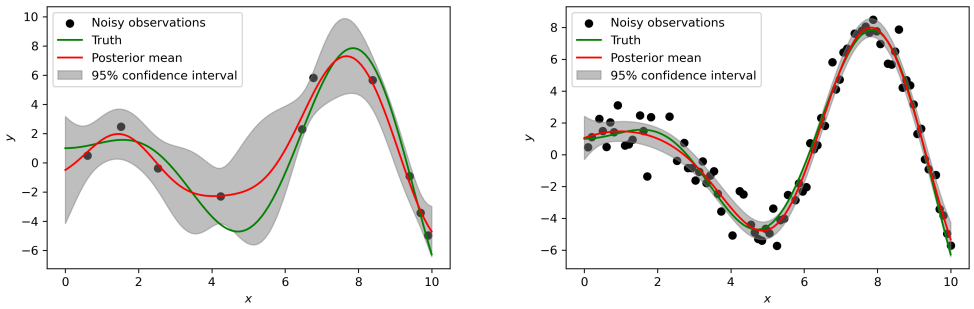

(a) (b)

Figure 2.8: Comparing GPR when **(a)** using 10% training data, and **(b)** 80% training data.

So far, we have concerned ourselves with a constant noise level (variance), σ_n^2, in the entire dataset. This is known as homoscedasticity. However, in most physical applications, the variance varies, as the input changes, and is known as heteroscedaticity. In chapter 5, we describe a methodology where modelling heteroscedastic noise with an additional Gaussian process is useful in better understanding and predicting the climate impact from aviation NO_x on O_3.

3

Methods

History shows that where ethics and economics come in conflict, victory is always with economics. Vested interests have never been known to have willingly divested themselves unless there was sufficient force to compel them.

Bhimrao Ramji Ambedkar

Model description is from Yin *et al.* [14] and Rao *et al.* [80]; Analysis of the ACCF submodel from Yin *et al.* [14]. These articles correspond to items 1 and 2 in the list of peer-reviewed journal articles.

3.1. Introduction

Climate models contain physical descriptions of all the components of the climate system (atmosphere, hydrosphere, cryosphere, lithosphere, and biosphere) and essentially simulate the transfer of matter and energy through these components. One class of climate models are called General Circulation Models (GCMs) which are often based on Numerical Weather Prediction models (NWPs) and mainly govern the modelling of atmospheric processes. Since the 1990s until the present [45], climate models have evolved to include processes related to land surface, ocean and sea ice, dynamic vegetation, carbon cycle, aerosols and atmospheric chemistry. These are often called Earth System models (ESMs) and running climate models in general is computationally expensive since this involves solving several partial differential equations governing physical processes and computing the radiative fluxes in 3D. This requires the use of powerful supercomputers which are accompanied with large storage requirements. After obtaining the radiative fluxes, it is trivial to calculate the global mean instantaneous RF. To tackle the first research sub-question defined in Chapter 1, the aCCFs have to be analysed and verified, which can be done with the use of an ESM. This ESM comprises the ECHAM/MESSy Atmospheric Chemistry (EMAC) chemistry-climate model (Section 3.2) along with several submodels. The main submodels pertinent to verify the ozone aCCFs are discussed in Sections 3.3 and 3.7 to 3.9. Owing to the significance of the aCCFs in this dissertation, the reader is provided with the necessary background regarding the modelling chain and their conception (Section 3.6). Since the aCCFs rely on meteorological inputs, adapting them in the EMAC framework is crucial since there is a natural difference in input values for weather forecasts (e.g., ECMWF) and climate models (e.g., EMAC). Furthermore, contrail cirrus aCCFs have a slightly different methodology compared to other aCCFs. For these reasons, contrail cirrus aCCFs are evaluated using these two different input sources and a correction term is determined to make more accurate predictions (Section 3.7.5). Lastly, Section 3.7.6 deals with uncertainties with respect to contrail cirrus aCCFs.

3.2. Global chemistry climate model EMAC

The ECHAM/MESSy Atmospheric Chemistry (EMAC) model is a state-of-the-art global atmospheric chemistry climate simulation system which contains submodels describing tropospheric, stratospheric and mesospheric processes. Interaction with oceans, land and human influences (e.g. anthropogenic emissions) are also implemented [44]. In this work, EMAC is used for an aviation climate assessment and utilises the second version of the Modular Earth Submodel System (MESSy 2.54) to link multi-institutional computer codes. The core atmospheric model bases on the 5th generation European Centre Hamburg general circulation model (ECHAM5; [81]). The atmospheric model ECHAM5 and the Modular Earth System Model MESSy [44], are the fundamental blocks of EMAC, which are briefly described before proceeding to the describing the source of the algorithmic climate change functions (aCCFs), which describe the climate impact of aviation emissions. These are part of the Algorithmic Climate Change Function (ACCF) submodel [14], which is described subsequently, along with other submodels such as AirTraf (an air traffic simulator [82]), Tagging (calculates the contribution of emissions

to concentrations, [83]), RAD (calculates the radiative forcing of GHGs, [84]), and CONTRAIL (calculates the potential coverage of persistent contrails, [39]). Subsequently, the sensitivity of contrail impact as predicted by the ACCF submodel is analysed.

The EMAC model has undergone extensive validation [44, 85] to assess its performance and accuracy in simulating various aspects of the atmosphere. Validation in this case involves comparing model output with observational data to evaluate how well the model represents real-world conditions. For example, Jöckel *et al.* [86] evaluated the background chemistry setup against the observations of tropospheric O_3 and its precursors made by Emmons *et al.* [87] for the years between 1983 and 2001 and found significant agreement. Additionally, Søvde *et al.* [35] performed a comprehensive evaluation across multiple models to assess the impact of aircraft NO_x emissions on the atmosphere by shifting cruise altitudes down or up one flight level. Along with EMAC, these included four other models that were employed to include detailed representations of tropospheric and stratospheric chemistry to cover the upper troposphere-lower stratosphere (UTLS) region. The models were found to be in good agreement with other studies (e.g., [19, 32, 34]) with respect to chemical perturbations in O_3 and the sensitivity to aircraft NO_x emissions to altitudinal changes.

3.2.1. Atmospheric model ECHAM5

The atmospheric model ECHAM5 has been developed from the European Centre for Medium-Range Weather Forecasts (ECMWF) operational forecast model cycle 36 [88]. Further developments were made at the Max-Planck Institute for Meteorology in Hamburg in order to adapt the model for climate simulations. ECHAM5 has a spectral dynamical core which solves the primitive equations for the hydrostatic approximation: continuity equation, conservation of momentum and thermal energy equation. The prognostic variables which include vorticity, divergence of the wind field, air temperature and the logarithm of surface pressure are given in spectral space (truncated series of spherical harmonics). The prognostic water species such as vapour, liquid, and solid are represented in Gaussian grid space. To define the vertical model structure, ECHAM5 applies an hybrid sigma-pressure system. Close to the surface, the hybrid coefficients follow the orography, whereas at higher altitudes (above 35 hPa), they describe pressure levels. The reader is referred to Roeckner *et al.* [81] for a detailed description of ECHAM5.

3.2.2. Modular Earth Submodel Sytem (MESSy)

The Modular Earth Submodel System (MESSy) [44] is a software and a framework used to link various submodels to a base model which leads to an Earth System Model (ESM). The MESSy software provides a modular kit with generalised interfaces for the standardised control and coupling of ESM components. These components describe individual processes in the troposphere and middle atmosphere and also feedback with ocean, land and anthropogenic influences. They are called submodels in MESSy and comprise currently about 110 submodels. MESSy provides the full hierarchy of model systems ranging from idealised box model setups, simplified climate model configurations, GCMs including atmospheric chemistry, to fully coupled representations of the Earth system including coupling with an interactive ocean. The most used model configuration is the EMAC model, whose underlying base model is ECHAM5. Note however that updates

have been made for physical parameterisations in the form of MESSy-compatible submodels.

The MESSy framework, shown in Figure 3.1, contains four layers, namely: base model layer (BML), base model interface layer (BMIL), submodel interface layer (SMIL), and submodel core later (SMCL). The BML serves as a 'power supply' and contains the base model, which is ECHAM5 in this dissertation. The BMIL facilitates in providing a means of exchanging information between the base model and the submodels compatible with it. In a way, it behaves as 'multiple socket outlet'. The SMIL can be regarded as the 'connector' by allowing information exchange between the submodels themselves, as well as with the base model via the BMIL. The final layer, SMCL, hosts the code describing the scientific aspects of the specific submodel and is independent of the base model and other submodels as a code structure.

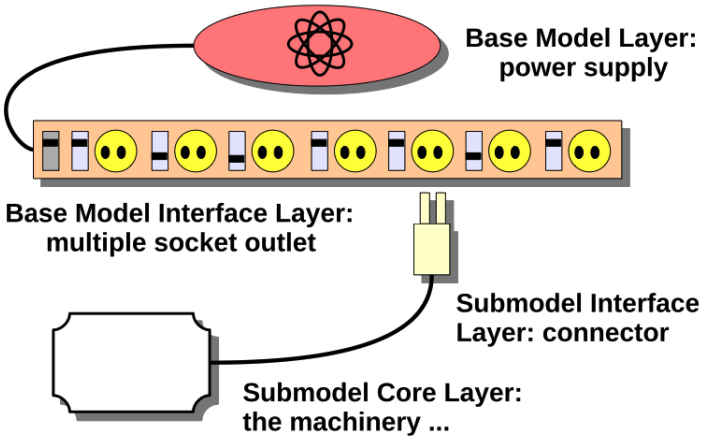

Figure 3.1: Sketch of the MESSy framework containing four layers. Taken from Kerkweg & Jöckel [89].

3.3. Contribution of Emissions to Concentrations Submodel: TAGGING

The assessment of the contribution of individual emissions of precursors on atmospheric composition necessitates a detailed analysis of the chemical conversion, transport and deposition of these species in numerical chemistry climate simulations. A frequently used method for this is called tagging and a generalised approach is described by Grewe [90]. The objective of the tagging scheme is to determine the contribution of emissions from various sectors to chemical species such as O_3, NO_y, HO_x, carbon monoxide (CO), non-methane hydrocarbons (NMHCs) and peroxyacyl nitrates (PANs). For instance, NO_x is a precursor of tropospheric O_3 (see Chapter 2) but has several anthropogenic emission sources, such as road traffic, shipping, industry and air traffic, and non-anthropogenic sources, such as lightning, emissions from soils, etc. In a similar vein, in order to calculate the impact of aviation emissions, coming from air traffic opti-

misation via the AirTraf submodel (Section 3.8), a category is created for this and denoted as `atf`. This allows and answer to the question "What is the contribution of air traffic emissions from AirTraf to O_3 mixing ratios and corresponding RF?" and is answered in Chapter 4. The tagging approach is implemented as a submodel (TAGGING 1.1, [83, 91]) within MESSy. As an example, eleven categories for the tagging method, as implemented in EMAC, are shown in Table 3.1. The tagging method for long-lived tracers (O_3, NO_y,NMHCs, and PANs) and short-lived tracers (HO_x) have different implementations which are covered in detail by Rieger [92].

Table 3.1: Overview of categories for the tagging submodel.

Category	Description	Origin
`air`	emissions from air traffic	anthropogenic
`atf`	emissions from AirTraf	anthropogenic
`bb`	emissions from biomass burning	anthropogenic and natural
`bio`	biogenic emissions	natural
CH_4	decomposition of CH_4	natural
`ind`	anthropogenic emissions excluding traffic	anthropogenic
`lig`	NO_x emissions from lightning	natural
N_2O	decomposition of N_2O	natural
`shp`	emissions from ships	anthropogenic
`str`	stratospheric O_3 production	natural
`tra`	emissions from road traffic	anthropogenic

3.4. AIRTRAC submodel

The AIRTRAC submodel uses a Lagrangian tagging approach to simulate the contribution of local NO_x and H_2O emissions to the composition of atmospheric constituents along air parcel trajectories. It was developed specifically to calculate a multitude of climate change function (CCF, Section 3.6.1) calculations in a single EMAC simulation, thereby making it computationally efficient. This way, independent cases can be directly compared with ease. Two shortcomings however, are that AIRTRAC uses linearised reaction rates for NO_x-O_3 chemistry and does not track all chemical processes that are discussed in Chapter 2.

3.5. CONTRAIL submodel

The Schmidt-Appleman criterion (SAC, [66, 67]) is a robust thermodynamic theory which uses the air temperature, relative humidity and ambient air pressure to determine the possibility of contrail formation and has been verified [93]. In addition, the persistence of contrails is dependent on conditions of ice-supersaturation, as discussed in Chapter 2. The CONTRAIL submodel incorporates these conditions to determine contrail formation. If the contrails are formed, the potential contrail coverage (PCC) is the fraction of an EMAC grid box which can be maximally covered by contrails and given by,

$$\mathrm{PCC} \equiv b_{\mathrm{con}} = b_{\mathrm{con+cir}} - b_{\mathrm{cir}} \,.$$

This represents the difference between the maximum possible combined coverage of contrails and cirrus ($b_{\mathrm{con+cir}}$) and the coverage of only natural cirrus (b_{cir}). Here, we have,

$$b_{\mathrm{con+cir}} = \begin{cases} \frac{r - r_{\mathrm{con}}}{r_{\mathrm{sat}} - r_{\mathrm{cir}}} - b_{\mathrm{cir}}(1 - b_{\mathrm{cir}}) & \text{if } r_{\mathrm{con}} \leq r \leq r^* \\ 1 & \text{if } r > r^* \text{ , and,} \end{cases}$$

$$b_{\mathrm{cir}} = 1 - \sqrt{\frac{r - r_{\mathrm{cir}}}{r_{\mathrm{sat}} - r_{\mathrm{cir}}}}\,.$$

In the equations above, r denotes the mean relative humidity of the EMAC grid, while r_{cir} and r_{con} denote the critical relative humidities above which a fraction of the EMAC grid box is covered by cirrus and is ice-supersaturated, respectively. The value of $r_{\mathrm{sat}} = 1$ for relative humidity at saturation. The relative humidity $r^* = r_{\mathrm{sat}} - \frac{(r_{\mathrm{cir}} - r_{\mathrm{con}})^2}{(r_{\mathrm{sat}} - r_{\mathrm{cir}})}$. Additional details for relative humidity and calculating the maximum possible coverage and available in and Burkhardt *et al.* [94] and Grewe *et al.* [39], respectively. The use of the CONTRAIL submodel in the calculation of aCCFs is discussed in Section 3.6.

3.6. Modelling chain for aCCFs

To facilitate the mitigation of the non-CO_2 effects of aviation via climate-optimised flight planning, "climate-sensitive regions" must be detected and avoided. This was the primary motivation behind the Reducing Emissions from Aviation by Changing Trajectories for the benefit of Climate (REACT4C, `https://www.react4c.eu/`, last accessed on 20 November 2023) project [36]. The project led to the development of CCFs [33, 39] that quantify the climate impact for a unit emission at a given longitude, latitude, altitude and time. The effects take into account the CO_2 emissions and non-CO_2 effects from the NO_x and H_2O emissions and contrail formation in the North-Atlantic Flight Corridor (NAFC). These CCFs enable the assessment of aircraft routing options with reduced climate impact and serve as the data source for the aCCFs. The calculation of CCFs using EMAC is discussed in detail in Grewe *et al.* [39], and here the main characteristics are discussed before proceeding to the concept of aCCFs, and their inclusion as a submodel (ACCF) in the MESSy framework.

3.6.1. Calculation of CCFs

The CCFs were calculated for NO_x and H_2O emissions for eight days that represent the eight weather patterns classified by Irvine *et al.* [95] for the NAFC. There are five distinct patterns for winter (WP1-5) and three for summer (SP1-3), which differ mainly by the position and strength of the jet stream. These patterns were found to be statistically significant in their frequency of occurrence based on 21 years of winter and summer meteorological re-analysis data. To calculate the CCFs, a pulse emission of NO_x (5×10^5 kg(NO)) and H_2O (1.25×10^7 kg(H_2O)) is released within one model time step of 15 minutes for each pre-defined location [33, 39]. The grid of these locations comprises seven latitudes (30 to 80°N), six longitudes (315 to 360°E) and four pressure altitudes (200 to 400 hPa), for each weather pattern and at 12 UTC, as shown in Fig. 3.2 (a). In total, there are 168 grid points or emission locations per selected day (red triangles in Fig. 3.2 (a)). To

account for the impact of these emissions without them feeding into background concentrations, the tagging approach by Grewe [90] is used. This is facilitated by Lagrangian submodel ATTILA [96] which transports emissions based on the EMAC wind field via 50 air parcel trajectories (magenta lines in Fig. 3.2 (a)) randomly over the EMAC grid (black grid in Fig. 3.2 (a)).

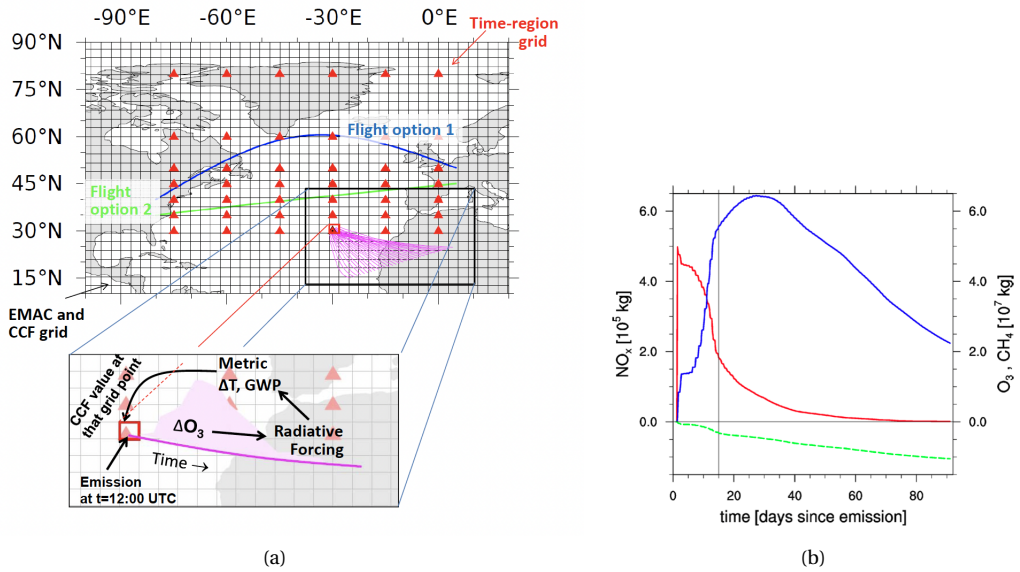

Figure 3.2: **(a)** Latitude–longitude grid of the climate change function (CCF) and EMAC grid (black) and location of the time-region centres (red triangles). Air parcel trajectories are started from the EMAC grid cell in which the time-region grid point is located; these trajectories are given in magenta for one grid point only. Two flight options are shown as examples in blue and green. Inlay: the climate cost function calculation is shown as an example for one air parcel trajectory. Taken from Grewe *et al.* [39]. **(b)** Temporal evolution of NO_x (red), O_3 (blue), and CH_4 (green) due to the release of NO_x emissions at an arbitrary time region over a simulation period of 90 days. Taken from Frömming *et al.* [33].

The subsequent contribution from NO_x emissions to concentration changes of chemical species is calculated for each of the trajectories with the AIRTRAC submodel [39]. AIRTRAC addresses a simplified system of chemical equations along air parcel trajectories by utilising the determined production (P) and loss (L) terms obtained from the kinetic solver (MECCA) [97] representing the background chemistry. Simultaneously, it computes the proportional contributions of emitted species to the atmospheric mixing ratios of all active nitrogen species (NO_y), nitric acid (HNO_3), O_3, HO_x, and CH_4 for each air parcel trajectory. The tagging method by Grewe [90] separates these emissions into distinct categories: background (b) and additional emissions (e) for computing the CCFs. For example, for the O_3 production from released NO_x emissions, the chemical reaction $HO_2 + NO \rightarrow NO_2 + OH$ (see Chapter 2), can be solved as [98]:

$$P^{e}_{O_3} = P^{b}_{O_3} \cdot \frac{1}{2} \cdot \left(\frac{HO^{e}_{2}}{HO^{b}_{2}} + \frac{NO^{e}}{NO^{b}} \right),$$

where P_{O_3} is the O_3 production rate in [mol/(mol s)] and all species are in [mol/mol]. Similarly, one of the O_3 loss reactions $HO_2 + O_3 \rightarrow OH + 2O_2$ (see Chapter 2), can be solved as:

$$L^{e}_{O_3} = L^{b}_{O_3} \cdot \frac{1}{2} \cdot \left(\frac{HO^{e}_{2}}{HO^{b}_{2}} + \frac{O^{e}_{3}}{O^{b}_{3}} \right),$$

where L_{O_3} is the O_3 loss rate in [mol/(mol s)]. The net O_3 contribution in [mol/mol] caused by NO_x is calculated by solving a differential equation using all the production and loss terms. Similarly for CH_4, the most relevant chemical reactions with regard to HO_x are taken into account. The temporal evolution of the contributions due to the emitted NO_x to the atmospheric burden of NO_x, O_3, and CH_4 at an arbitrary grid point is depicted in Fig. 3.2 (b). The NO_x is almost completely consumed within 40 days, while the O_3 peaks in about 30 days following which there is a gradual decline. The CH_4 decreases as a result of increase in OH due to increase in NO_x in the beginning and resulting increase in O_3, later (see Chapter 2). Atmospheric processes, such as wash-out and dry deposition, are also proportionally taken into account on the air parcel trajectories.

For H_2O emissions, only loss processes are considered: $\frac{dH_2O}{dt} = -\frac{pr}{H_2O^{tot}} H_2O$, where pr is the precipitation rate and implies water vapour loss [mol mol^{-1} s^{-1}] in the corresponding EMAC grid in the form of rain and snowfall. In the same grid, H_2O^{tot} represents the total amount of water vapour [mol mol^{-1}]. In this EMAC setup, at every time step, the atmospheric ability to form contrails is evaluated following the work of Burkhardt *et al.* [94] and Burkhardt & Kärcher [99]. The potential contrail coverage (PCC) is a measure of this atmospheric ability and indicates the largest fraction of a grid box that can be covered by contrails. This calculation is performed by the CONTRAIL submodel (Section 3.5) where the actual contrail coverage is determined only if air traffic occurs in the respective grid box. The temporal development of contrails according to spreading, sublimation, and sedimentation of ice particles is parameterised.

Subsequently, radiative changes are computed by transforming the required quantities that were calculated for the air parcels onto the EMAC grid. These radiation changes are then averaged to obtain the global annual instantaneous radiative forcing (iRF, see Chapter 2) as a result of the local emissions. Using a metric, iRF is first converted to adjusted RF and then to CCF, which represents the global average temperature response (ATR) over a time horizon (e.g. 20 years), measured in K/kg emission of K/km for effects from contrail coverage ([33, 39]). ATR over 20 years is chosen because it is a suitable climate metric to answer the question “What potential reduction in climate impact could be achieved in the next few decades, by steadily applying climate optimised aircraft routing ?". Finally, Grewe *et al.* [38] used the CCFs as an objective function in an air traffic optimisation routine to avoid climate sensitive regions in the NAFC. They quantitatively show that a reduction potential of up to 25% in climate impact for a small increase in cost (0.5%) is possible relative to conventional flights that are optimised to maximise profits for airlines. However, these results were computationally intensive for real-time calculation and also restricted to the Trans-Atlantic airspace. This makes the practical use of these tools in climate-optimised flight planning a major obstacle, which motivates the use of general and practical tool, discussed in Section 3.6.2.

While a direct validation of CCFs is not possible since most of the simulated effects cannot be measured directly. Also, a direct inter-comparison with other numerical studies is difficult due to a difference in objectives and emission scenarios. However, various sensitivity studies were performed by Grewe *et al.* [38] on the basis of temporal and horizontal resolutions, and the number of air parcel trajectories used. As far as the chemistry is concerned, comparisons of the temporal evolution and lifetimes of NO_x and O_3 were found to be roughly in agreement with Stevenson [75]. The resulting RF of O_3 and CH_4 (from NO_x) and H_2O were also found to be well within the range of other studies e.g. [15, 63]. Finally, even results for contrail properties and radiative impacts were found to agree reasonably well with Myhre *et al.* [100].

3.6.2. Conception of aCCFs

The project “Air Traffic Management 4 Environment" (ATM4E, https://www.atm4e.eu/, accessed on 20 November 2023) project explored the feasibility of a concept for environmental assessment of ATM operations working towards environmental optimisation of air traffic operations in the European airspace [101]. The project aimed to overcome the restrictive nature of calculating CCFs (see above), by formulating algorithmic approximations of the global impact based on the correlation with weather variables. These expressions, called aCCFs, are derived by regressing CCFs against 2 or 3 local atmospheric variables at the time of emission with simple regression techniques. The aCCFs are based on data limited to the North Atlantic region, but owing to a similar meteorology along latitudes, it is expected to be applicable in the entire northern extra-tropics. The aCCFs are formulated separately for the NO_x effect on O_3 (NO_x-O_3) and methane (NO_x-CH_4), CO_2, H_2O [42], as well as contrail cirrus (supplement of [14]). For each of these effects, literature was reviewed to pre-select atmospheric variables and scatter plots between CCFs and the variables were visualised to pick the most influential variables. The aCCFs, obtained by regressing the CCFs against the chosen variables, serve as a computationally inexpensive and fairly general surrogate model to predict the climate impact in terms of ATR20 as a function of the emission concentration (for CO_2) or meteorological inputs (for non-CO_2 effects). The ATR20 is for a pulse emission scenario (release of a large and instantaneous amount of a greenhouse gas) and denoted as P-ATR20. This can be converted to F-ATR20 for future emission scenarios (e.g., Fa1 scenario, [102]). The form of each of the aCCFs in the submodel is discussed briefly in Section 3.7. A general comparison between the characteristics of the CCFs and aCCFs is listed in Table 3.2. Firstly, CCFs can only be used for the specific days it was calculated for, while aCCFs can be calculated using weather forecasts for any arbitrary day. Secondly, the CCFs are applicable only in the regions they were calculated for (North Atlantic), while the methodology used for aCCFs makes it applicable for more parts in the Northern hemisphere. Thirdly, CCFs cannot be implemented in real-time, because they are computationally expensive to generate, while the aCCFs are simple models that can be implemented using Numerical Weather Prediction models (NWPs). Lastly, CCFs have been validated by Grewe *et al.* [39] by comparing them with earlier modelling studies. On the other hand, the aCCFs are implemented as a submodel called ACCF in EMAC (Section 3.7), to enable its use and verification via chemistry-climate model simulations and the use of an air traffic optimisation submodel called AirTraf (Section 3.8). The veri-

fication of O_3 aCCFs is performed in Chapter 4.

Table 3.2: Comparison of crucial characteristics of CCFs and aCCFs. NWPs stands for Numerical Weather Prediction models.

Parameters	**CCFs**	**aCCFs**
Weather	5 specific winter days and 3 specific summer days	Arbitrary days
Geographical applicability	North Atlantic region	30-90° N
Real-time implementation	Limited due to expensive computations	Easily implemented in NWPs
Verification process	Comparison of general patterns with literature	Climate-chemistry model simulation with flight optimisation tool

3.7. ACCF submodel

The aCCFs, as discussed above, estimate the climate impact of local aviation CO_2 emissions, H_2O emissions, NO_x emissions and contrail cirrus based on meteorological inputs. This complete set, is coded as a submodel called ACCF [14] according to the MESSy standard (Section 3.2.2) to enable its use in climate model simulations with EMAC. Each of the aCCFs are discussed in this section.

3.7.1. CO_2 aCCF

Since CO_2 is a long-lived gas, its climate impact is directly proportional to its emitted quantity. Assuming 1 Tg of fuel was burnt by the aviation industry in 2017, the corresponding impact is calculated using a chemistry-climate response model called AirClim [31]. The resulting CO_2 aCCF is 7.48×10^{16} K/kg(fuel) and represents the pulse average temperature response of CO_2 emissions from 2017 to 2036 (P-ATR20 of CO_2). For the same amount of CO_2 emissions in 2017, but assuming an annual growth rate according to a Business As Usual (BAU) future scenario as specified by Grewe *et al.* [29], the CO_2 aCCF is 7.03×10^{-15} K/kg(fuel) and represents the average temperature response of the future scenario (F-ATR20 of CO_2).

3.7.2. H_2O aCCF

Water vapour (H_2O) is a greenhouse gas, that is already present in large concentrations in the troposphere. Subsonic aviation releases H_2O mostly in the troposphere, and the small amounts that reach the lower stratosphere are swiftly returned to the troposphere [103]. The life time of H_2O has a strong correlation with altitude, and hence, distance to the tropopause is a good indicator of the climate impact from H_2O. After considering different definitions for tropopause height, van Manen & Grewe [42] found potential vorticity (PV) to be the most useful definition and derived the following formula for H_2O aCCF [K/kg(fuel)] for a point in space-time (x, y, z, t),

$$\mathrm{aCCF}_{\mathrm{H_2O}}(PV) = 4.05 \times 10^{-16} + \left(1.48 \times 10^{-16}\right)|PV|, \tag{3.1}$$

and represents F-ATR20 of H_2O. PV is a useful concept that combines the physical processes of vorticity and stratification. The PV is larger in the stratosphere than in the troposphere, so it has been commonly used to track cross-tropopause transport in meteorology [104]. PV is expressed in potential vorticity units (PVU) and has the form 10^{-6} $[(\mathrm{K\,m^2})/(\mathrm{kg\,s})]$. The adjusted R^2 for the H_2O aCCF based on the training data is 0.59, and thus statistically significant.

3.7.3. NO_x aCCF

Nitrogen oxide (NO_x = NO + NO_2) is an indirect greenhouse gas that influences the atmospheric concentrations of O_3, CH_4 and stratospheric H_2O, as described in Chapter 2. The NO_x aCCF includes specific formulae for all effects, except stratospheric H_2O.

O_3 aCCF

The chemical reaction of NO with HO_2 produces NO_2 which undergoes photolysis to form $O(^3P)$ and subsequently, O_3, in the short term (within few weeks). This corresponds to a strong warming effect. van Manen & Grewe [42] use temperature (T) and geopotential (ϕ) as the meterorological variables with the following formula for O_3 aCCF [K/kg(NO_2)] for a point in space-time (x, y, z, t),

$$\begin{aligned} \mathrm{aCCF}_{O_3}(T,\phi) = &-5.20\times10^{-11} + \left(2.30\times10^{-13}\right)T + \left(4.85\times10^{-16}\right)\phi \\ &- \left(2.04\times10^{-18}\right)T\phi\,, \end{aligned} \tag{3.2}$$

and represents F-ATR20 of O_3. If a certain input (T,ϕ) results in a negative value for Eq. (3.2), the result is converted to zero, since no cooling effect is expected from O_3 production. The adjusted R^2 on the training data is 0.42, and the following chapter looks at a detailed verification procedure of O_3 aCCF in terms of its mitigation potential through flight re-routing. An example of O_3 aCCFs is shown in Figure 3.3 for an arbitrary weather situation, where a clear connection is seen between the two panels in terms of the patterns. In general, higher values of temperature and geopotential are associated with higher values of O_3 aCCFs.

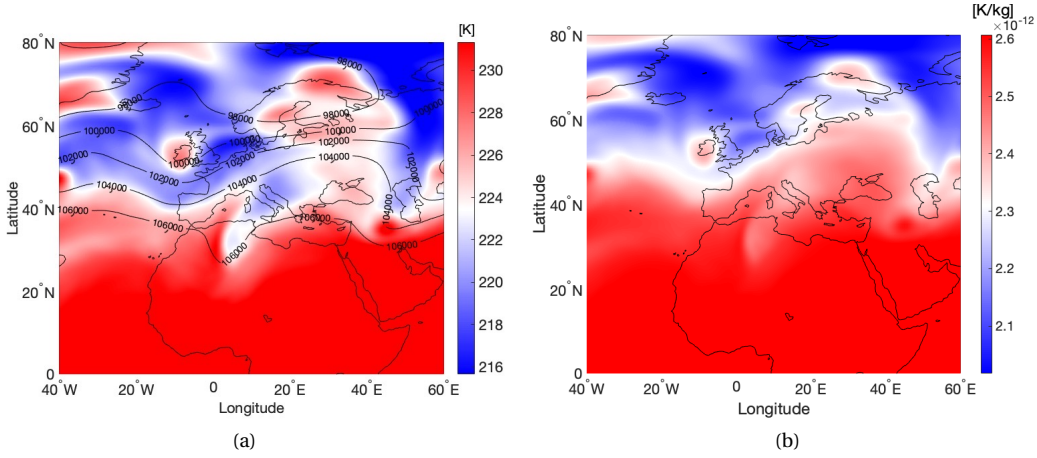

Figure 3.3: Meteorological parameters and O_3 aCCFs at 250 hPa: (**a**) geopotential (isolines, m^2/s^2) and temperature (isolines, K), (**b**) O_3 aCCFs (colour contours, K/kg(NO_2)).

CH_4 aCCF

The production of O_3 from NO_x, enhances the OH concentration, that then enables the oxidation of CH_4. The reduction in the concentration of CH_4 in the troposphere, induces

a cooling effect. After a detailed analysis of various predictors, van Manen & Grewe [42] find that geopotential (ϕ) and solar irradiance (S_r) are most suitable. The formula for CH_4 aCCF [K/kg(NO_2)] for a point in space-time (x, y, z, t) is,

$$\begin{aligned} \mathrm{aCCF}_{\mathrm{CH_4}}(\phi, S_r) = &-9.83\times10^{-13} + \left(1.99\times10^{-18}\right)\phi - \left(6.32\times10^{-16}\right)S_r \\ &+ \left(6.12\times10^{-21}\right)\phi S_r\,, \end{aligned} \tag{3.3}$$

and represents F-ATR20 CH_4. If a certain input (ϕ, S_r) results in a positive value for Eq. (3.3), the result is converted to zero, since no warming effect is expected from CH_4 depletion. The adjusted R^2 on the training data is 0.17, and thus statistically insignificant.

PMO aCCF

The depletion of CH_4 leads to a reduced O_3 production rate and called primary mode ozone (PMO) [60]. This PMO effect, while significantly smaller than the initial O_3 production, has a longer lifetime since it is bound to the CH_4 perturbation. The PMO effect can be linked to the CH_4 perturbation by a linear scaling factor [105]. Furthermore, the decrease in CH_4 entails a smaller transport to the stratosphere, which reduces the SWV. Both PMO and SWV are cooling effects and the former is modelled by scaling Eq. (3.3),

$$\mathrm{aCCF}_{\mathrm{PMO}} = 0.29\times\mathrm{aCCF}_{\mathrm{CH_4}}, \tag{3.4}$$

which represents P-ATR20 of CH_4, and can be converted to F-ATR20 of CH_4, [14].

3.7.4. Contrail cirrus aCCF

Day and night contrails have contrasting effects on shortwave and longwave radiation, thus separating their climate impact is logical. The contrail cirrus aCCF is classified into day-time and night-time impacts that depend on outgoing long-wave solar radiation (OLR) and dry air temperature (T), respectively. These relations are captured in Eq. (3.5) and Eq. (3.6) which were derived using re-analysis data (supplement of Yin *et al.* [14]),

$$\mathrm{RF}_{\mathrm{day\,contrail}}(OLR) = 10^{-10}\cdot(-1.7 - 0.0088\cdot OLR)$$

$$\mathrm{aCCF}_{\mathrm{day\,contrail}}(OLR) = 0.0151\cdot\mathrm{RF}_{\mathrm{day\,contrail}}(OLR) \tag{3.5}$$

$$\mathrm{RF}_{\mathrm{night\,contrail}}(T) = \begin{cases} 10^{-10}\cdot\left(0.0073\cdot10^{0.0107\cdot T} - 1.03\right) & \text{if } T > 201\mathrm{K} \\ 0 & \text{otherwise} \end{cases}$$

$$\mathrm{aCCF}_{\mathrm{night\,contrail}}(T) = 0.0151\cdot\mathrm{RF}_{\mathrm{night\,contrail}}(T) \tag{3.6}$$

Here, the contrail cirrus aCCF [K/km] has been obtained by first calculating the global and annual mean RF [W/m^2] using the parametric equation of Schumann [106] and scaling it by 0.0151 K/W/m^2 (derived using AirClim [14]) to represent it as P-ATR20 of contrail cirrus. Thus, unlike the other aCCF formulae, it does not calculate the P-ATR20 directly.

During the day, contrails can produce a net cooling effect by reflecting incoming solar radiation. Consequently, Eq. (3.5) predict negative values of RF when $OLR < -193$ W/m^2. On the other hand, night-time contrails only cause warming, due to their effectiveness in trapping infrared radiation. Thus, negative values of RF are avoided by setting $T > 201$ K in Eq. (3.6).

3.7.5. Adaptation of aCCFs in EMAC

The aCCFs are heavily dependent on meteorological parameters such as temperature. If they are to be used for generating climate-optimised trajectories in day-to-day operations, the source of meteorological data becomes crucial. Typically, the aCCFs have been tested with EMAC, which is a climate model. Climate models do not directly use weather forecast data, but can be “nudged" towards data from NWPs, observations or reanalysis forecasts to give a realistic representation of the atmosphere at a given time. In the simulation setup, certain variables such as temperature (T) in EMAC are nudged towards meteorological re-analysis data from the ECMWF database. Thus, the impact of differences between temperature used by EMAC, and weather forecasts can have implications on climate impact estimates from aCCFs. Additionally, the derivation of contrail cirrus aCCFs follows a slightly different methodology compared to other aCCFs. Since contrail cirrus aCCFs depend on T as well OLR, the influence of these variables based on their source is can be tested. By coupling the CONTRAIL submodel (Section 3.5) to the ACCF model (Section 3.7) using the MESSy framework, the PCC is first calculated by the former and if the SAC criterion is met for contrail formation, the ACCF submodel estimates the climate impact from contrails provided they are persistent (i.e., PCC > 0). It is shown in this section that a correction term for temperature in EMAC impacts both PCC as well as climate impact estimates from contrail cirrus aCCFs.

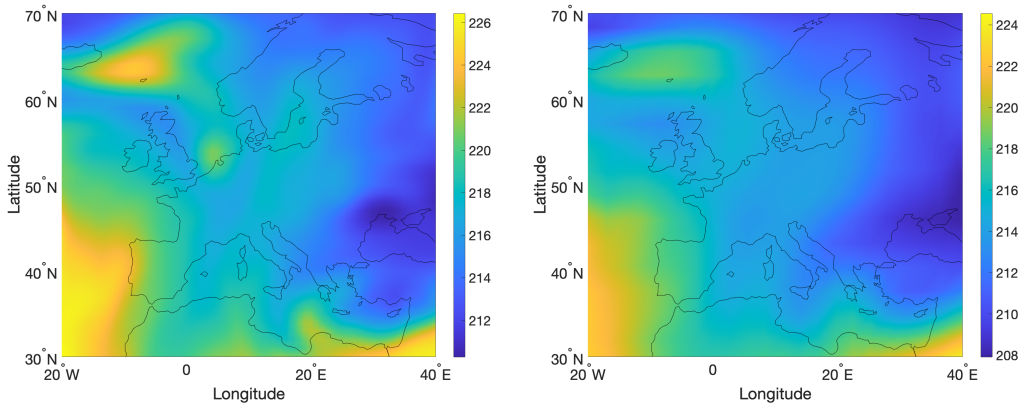

(a) ECMWF dataset

(b) EMAC dataset

Figure 3.4: Temperature data corresponding to pressure level of 250 hPa at 06:00 UTC on 18th December 2015 for **(a)** ECMWF dataset and **(b)** EMAC dataset.

Temperature

As a result of nudging, there is a natural difference in the temperature dataset for the data nudged by EMAC and the original ECMWF data as shown in Fig. 3.4. Since the relationship of the climate impact with temperature is modelled to be exponential (Eq. (3.6)), the difference in the result for the two temperature datasets is considerable (Fig. 3.6a). This motivated an attempt to determine a correction factor for the nudged EMAC temperature with the help of standard linear regression techniques. No statistically significant relation was found between the EMAC dataset and the difference in temperature corresponding to a given time (Fig. 3.5a) as well as for a fixed pressure level (Fig. 3.5b). However, it was found that the mean temperature difference is about 3 Kelvin lower for the nudged EMAC data considering the available pressure levels and times in the dataset. The case of 250 hPa at 06:00 UTC is shown in Fig. 3.6b. The idea is to first test the impact of the correction term (by increasing EMAC temperature by this amount) in EMAC only on the potential contrail coverage (PCC). Subsequently it is also applied to the input temperature used by the ACCF submodel.

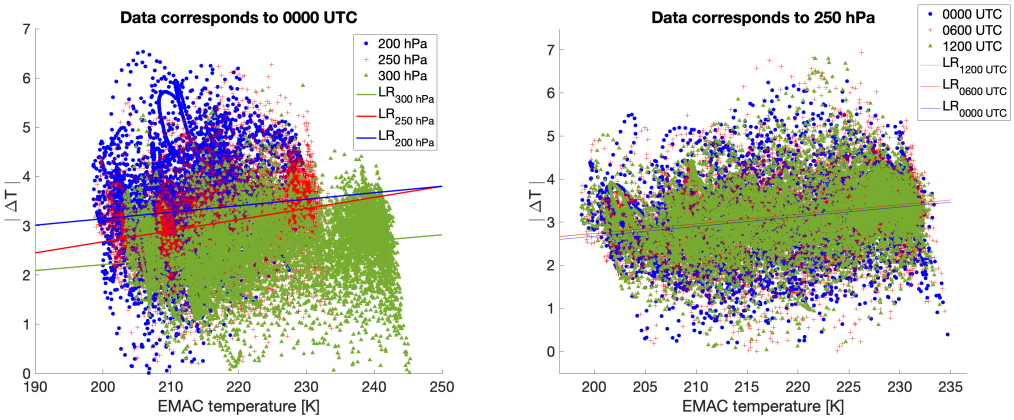

(a) Data at 00:00 UTC

(b) Data at 250 hPa

Figure 3.5: Linear regression analysis of the EMAC data set and absolute difference between datasets. The solid lines represents the best least squares fit for each pressure level in **(a)** and for each time in **(b)**. The R^2 coefficient for all fits are extremely poor.

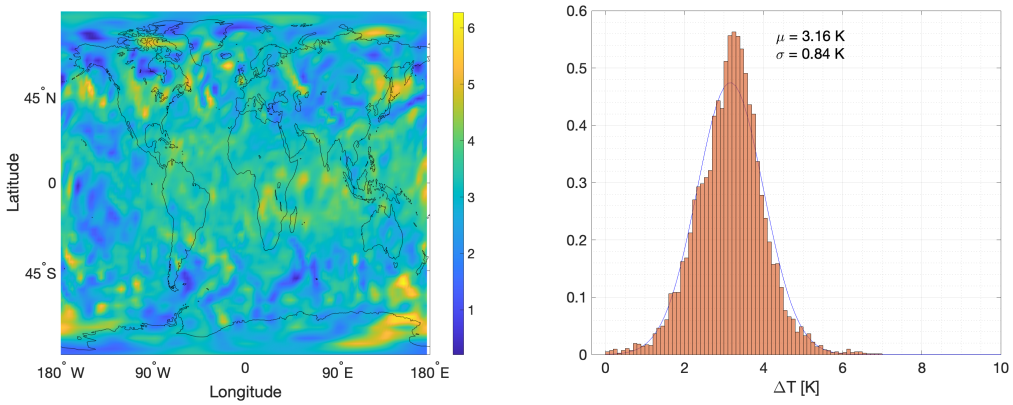

(a) Absolute difference in temperature

(b) Mean difference in temperature

Figure 3.6: Quantitative analysis of temperature difference between data sets corresponding to a pressure level of 250 hPa and at 06:00 UTC.

Figures 3.7 and 3.8 compare the original PCC and corrected PCC for 18th December 2015 at 250 hPa at two different times. Note that the PCC has significantly decreased with lower peak values for the latter. This is attributed to the corrected temperature being higher than the default temperature.

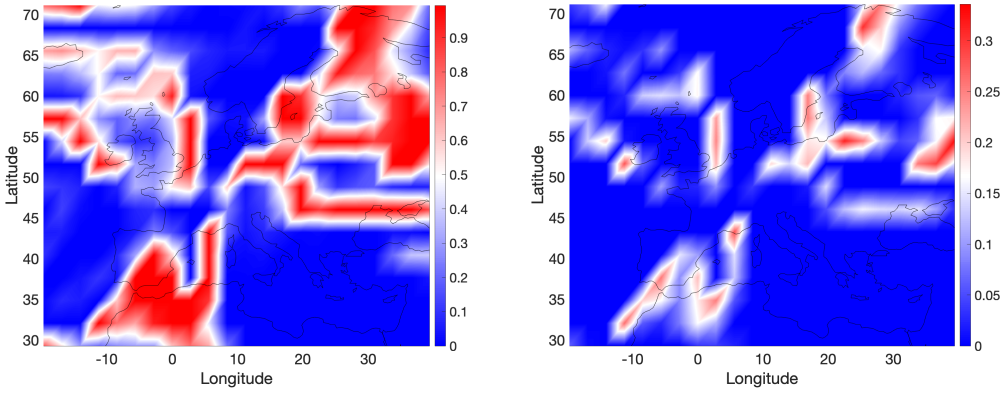

(a) Original temperature

(b) Adjusted temperature

Figure 3.7: PCC at 00:00 UTC.

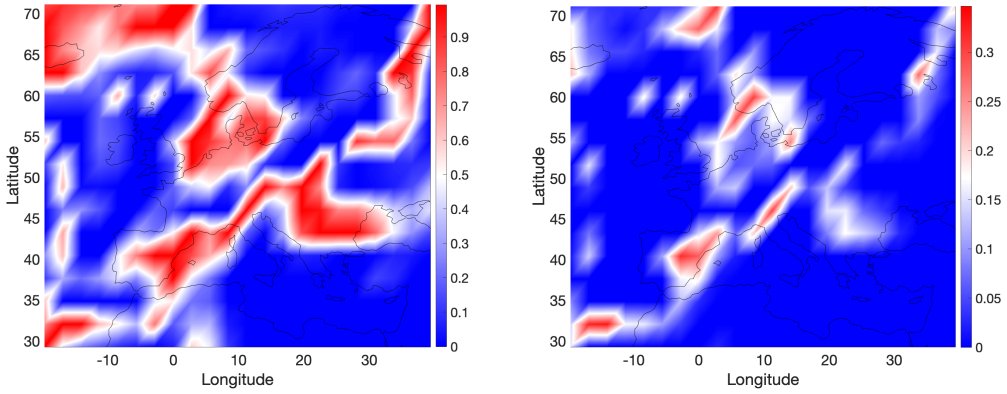

(a) Original temperature

(b) Adjusted temperature

Figure 3.8: PCC at 12:00 UTC.

Next we can compare the estimated climate impact of contrails in terms of ATR20 by the contrail aCCFs for the original condition and when the bias is applied to PCC. The results for 18th December at 250 hPa for two different times are illustrated in Figs. 3.9 and 3.10. Since the PCC shrinks because of the warmer temperature, the contrail impact is also spread over a smaller area.

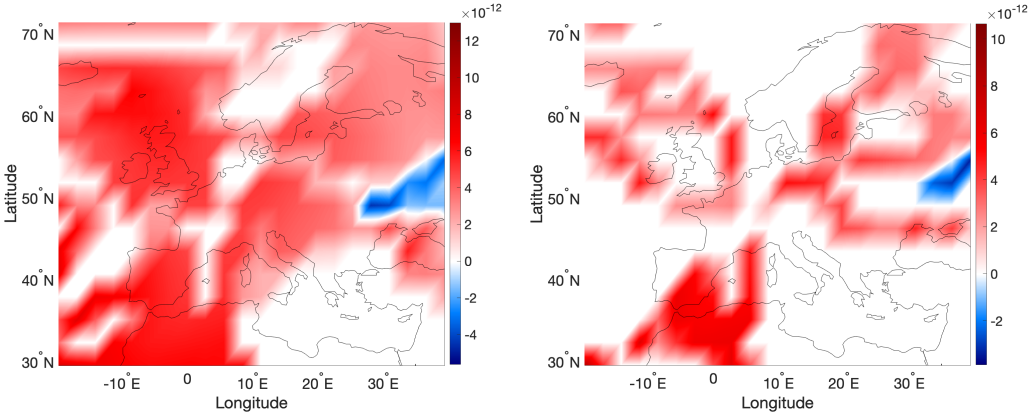

(a) Original temperature

(b) Adjusted temperature

Figure 3.9: ATR20 from contrails at 00:00 UTC.

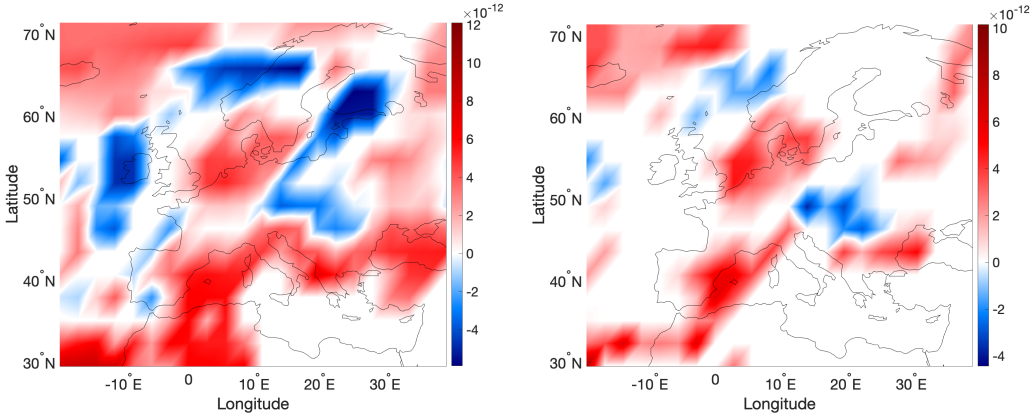

(a) Original temperature

(b) Adjusted temperature

Figure 3.10: ATR20 from contrails at 12:00 UTC.

Finally, we compare the effect of the bias temperature term when applied only for PCC and when it is also applied to the temperature term for contrail aCCFs (Eq. (3.6)). This is illustrated in Figs. 3.11 and 3.12. It can be seen that since the PCC is common for both cases, the patterns are identical. However, the contrail impact itself is higher, because the increase in temperature through the bias term increases the climate impact of night contrails.

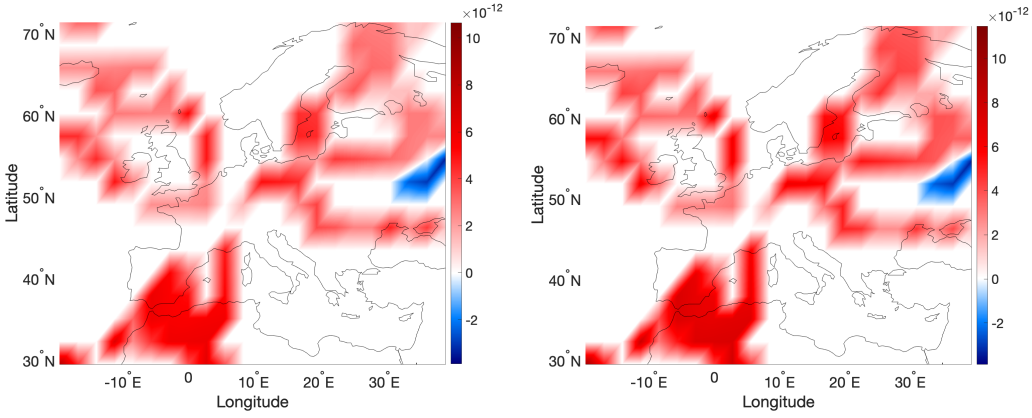

(a) Original temperature

(b) Adjusted temperature

Figure 3.11: ATR20 from contrails at 00:00 UTC.

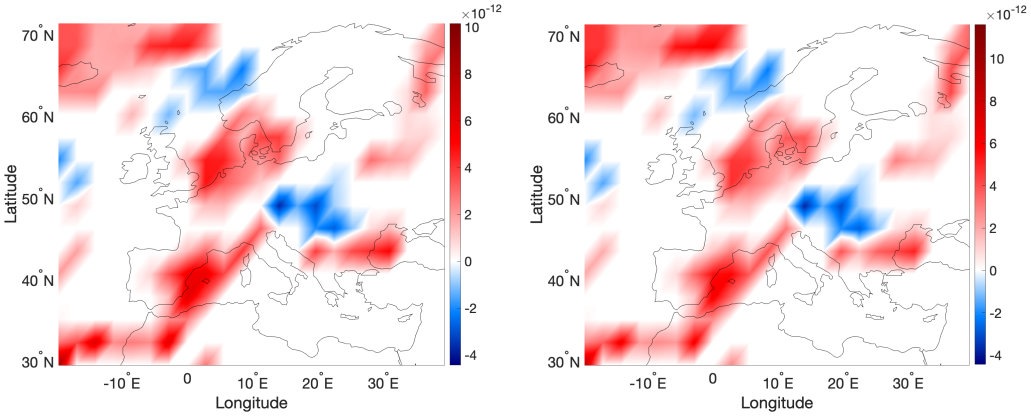

(a) Original temperature

(b) Adjusted temperature

Figure 3.12: ATR20 from contrails at 12:00 UTC.

Outgoing Longwave Radiation (OLR)

Numerical weather prediction models (NWPs) and climate models make use of various cloud schemes and radiation schemes. Often, there is a difference in radiation schemes used between them due to different functionalities of the model. For instance, both require the quantification of coupled atmospheric, land, ocean and radiation processes, but the stark difference in timescales indicate that different physical mechanisms are emphasised [107]. Climate models are more focused on measuring the global energy balance (radiation budget) while weather models are more focused on capturing physics occurring at much smaller timescales. For the sake of comparison, the difference in *OLR* calculation for both models is shown in Fig. 3.13. It is evident that the *OLR* is naturally different for EMAC and ECMWF because the former is a climate model while the latter is a NWP. However, the resulting difference in day-time impact (Eq. (3.5)) is not significant.

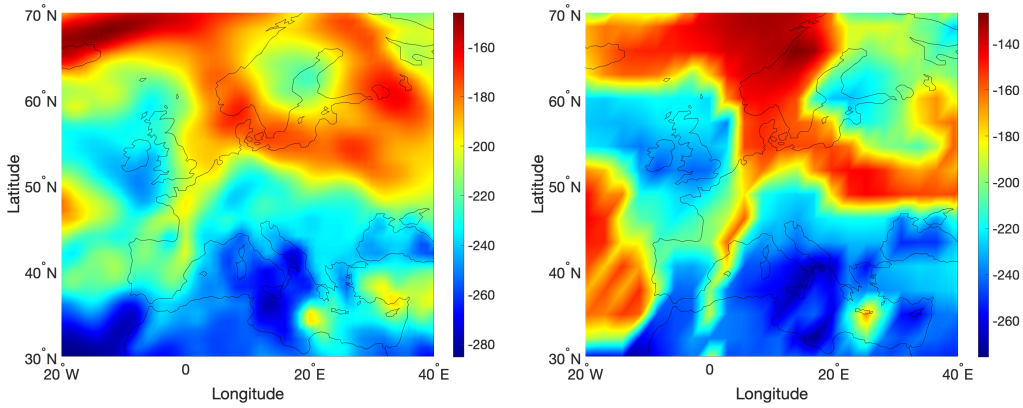

(a) ECMWF dataset

(b) EMAC dataset

Figure 3.13: OLR data corresponding to 00:00 UTC.

3.7.6. Uncertainties for contrail aCCFs

While contrail-cirrus effects contribute to significant net warming, the confidence level of these estimates is considerably low [52]. Estimating the RF of contrails is complex as it is dependent on several parameters such as ice particle composition, shape, distribution, lifetime, etc. The largest uncertainties in assessing contrail RF have been caused by a dearth of knowledge of not only the contrail coverage but also the optical thickness of persistent contrails [108, 109]. Acquiring accurate information about these parameters requires simulations occurring at a very fine resolution which may be possible with large eddy simulations (LES) and/or observational data. The derivation of contrail aCCFs are based on Lagrangian simulations of contrails in the Trans-Atlantic for a range of scenarios to obtain their position, temperature, and average lifetime. This information is used to estimate contrail optical depth and solar zenith angle to enable their use in a parametric equation [106] to estimate the RF based on a specific contrail composition. Additionally, the atmospheric data such as relative humidity and temperature are also characterised by uncertainties due to nudging and natural atmospheric variability. Thus, uncertainties in meteorological conditions, and parameterisations for cloud microphysics propagate to the aCCFs. There is also a latitudinal dependency of contrail aCCFs as the flight traffic varies latitudinally, and is subject to further investigation. Also, two different aircraft, can produce a contrails with different properties for the same atmospheric conditions, due to a difference in overall propulsive efficiency, fuel use and combustion techniques which are not taken into account by the contrail aCCFs. In this section, which serves as a preliminary analysis, we looked a subset of these uncertainties arising from differences between ECMWF reanalysis data and the EMAC model that is nudged towards this dataset at three pressure levels and times. It was shown in Section 3.7.5 that the temperature difference impacts the predicted PCC and the consequent climate impact prediction from contrail aCCFs. The two main effects observed when the corrected temperature were used were as follows: (i) the warmer temperature reduced

PCC, and (ii) the maximum value of climate impact in terms of ATR20 increased when applied to the contrail aCCFs.

3.8. The Air Traffic Simulator Submodel: AirTraf

AirTraf 2.0 [110] is a global 3D air traffic simulation tool which is implemented in EMAC as a submodel. This submodel has various optimisation objectives, as shown in Figure 3.14, and can take into account effects of local weather conditions (e.g., wind) during air traffic optimisation. The air traffic information comprises the Eurocontrol's Base of Aircraft Data (BADA Revision 3.9, [111]) aircraft performance model and the International Civil Aviation Organization (ICAO) [112] emission data bank. Fuel use and NO_x emissions are calculated by the total energy model based on the BADA methodology [113] and the DLR (Deutsches Zentrum für Luft- und Raumfahrt) fuel flow method [114]. The flight trajectory optimisation is performed by the Adaptive Range Multi-Objective Genetic Algorithm (ARMOGA version 1.2.0, [115–117]).

Figure 3.14 shows the AirTraf procedure and the routing options available for optimisation. First, air traffic data are required, which consist of a 1-day flight plan of city pairs and the departure times. Additionally, aircraft and engine performance data are also provided. For all optimisation objectives, the local weather conditions are provided by online calculation of ECHAM5. The last routing option is climate impact, and is optimised with respect to aCCFs. This option is coded by coupling AirTraf and ACCF submodels using the MESSy interface. The optimised trajectory is dependent on setting certain bounds for design variables. There are eleven design variables in total for the geometry definition of a flight trajectory, five of which are altitude-related (vertical cross section) and six are related to the latitude and longitude (horizontal cross section), as shown in Figure 3.15. These variables can be adjusted by the user according to the type of re-routing that is desired. Following the flight trajectory calculation, fuel use and NO_x emissions are calculated. Subsequently, aircraft positions are advanced along the flight trajectory corresponding to the time steps of EMAC. Finally, the individual aircraft's emissions corresponding to the flight path in one time step are gathered into a global field. The flying process ends when the arrival check is passed.

3.9. Radiation Infrastructure Submodel: RAD

Radiative calculations are conducted using the RAD submodel [84]. The longwave terrestrial radiative spectrum is segmented into 16 spectral bands (ranging from 3.33 to 1000 μm) and is determined following the approach outlined by Mlawer *et al.* [119]. Solar radiation, or shortwave radiation, is partitioned into 4 spectral bands (covering ultraviolet, visible, and near-infrared wavelengths from 0.25 to 4.00 μm) and computed according to the methodology of Bonnel [120]. To enhance resolution in the shortwave spectrum, particularly in the stratosphere and mesosphere, the FUBRAD submodel expands the spectral bands to 55, as described by Nissen *et al.* [121].

The RF of O_3 perturbations is defined as the difference in the net radiative fluxes caused by a change (e.g., between two time periods such as pre-industrial and present day; [8]). In this context, the focus lies on examining the impact of AirTraf NO_x emissions (`atf`) on this radiative forcing (RF), which will be discussed in Chapter 4. The strato-

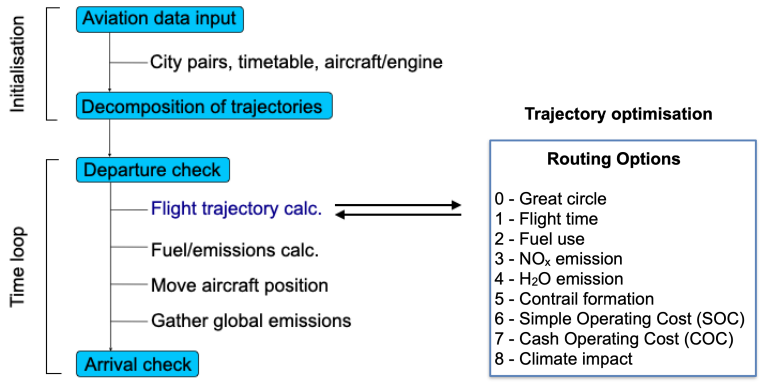

Figure 3.14: An overview of an AirTraf simulation, adapted from Yamashita *et al.* [118] and updated with the new optimisation objectives Yamashita *et al.* [110].

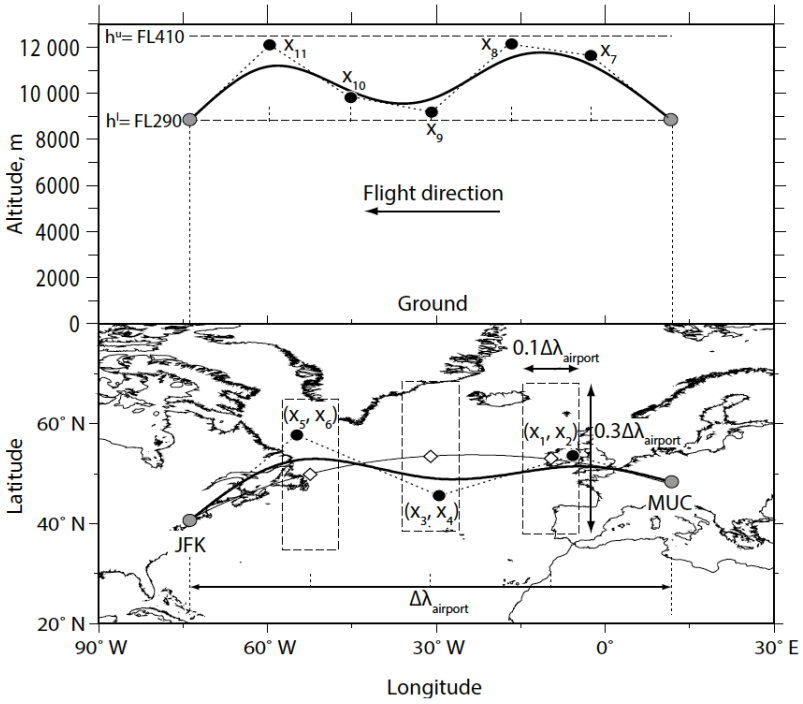

Figure 3.15: The geometry definition of a flight trajectory with the vertical cross section (**top**) and horizontal cross section (**bottom**) reprinted from Yamashita *et al.* [82]. The bold solid line indicates the real trajectory from MUC to JFK. The black dots are control points determined by design variables x_i. The cruise flight altitude is allowed to vary from 29,000 feet (FL290) to 41,000 feet (FL410). Bottom: the dashed boxes show rectangular domains of three control points. The diamonds along the great circle are centre points of the boxes. $\Delta\lambda_{\text{airport}}$ is the longitudinal distance between two cities.

spheric adjusted RF is calculated (see Chapter 2), but this value only covers part of the stratospheric temperature adjustment. The adjustment requires an additional spin-up simulation of three months, but since we are dealing with pulse NO_x emissions, this time frame would cause the pulse to disappear. The full O_3 contribution is calculated from all emission sources, and contributions from all sources except AirTraf (`non-atf`) are then subtracted using the EMAC submodel SCALC [44]. That is,

$$\mathrm{RF}(\mathrm{O_3atf}) = \mathrm{RF}(\mathrm{O_3}) - \mathrm{RF}(\mathrm{O_3non\text{-}atf}) \tag{3.7}$$

This approach is consistent with the IPCC RF definition, since the sum of all individual RF contributions approximately equals the total RF (for a detailed example, see Dahlmann *et al.* [122] and Mertens *et al.* [123]).

4

Verification of NO_x-O_3 aCCFs for air traffic optimisation

All models are wrong, but some are useful.

George Box

Parts of this chapter are from Rao *et al.* [80]. This article corresponds to items 1 in the list of peer-reviewed journal articles.

4.1. Introduction

Reduction of aviation induced climate impact by climate-optimised flight planning requires a quick prediction tool such as aCCFs. In order to analyse and verify the aCCFs, which is in line with the first research sub-question, the relevant climate modelling framework was described in Chapter 3. The quality of the aCCFs are expressed in terms of the adjusted R^2 [43] and while this value is large for H_2O aCCFs, for O_3 aCCFs and CH_4 aCCFs, it is much smaller [42]. Due to the complexity of NO_x-O_3 chemistry (see Chapter 2), and the lack of many studies to mitigate these impacts particularly in the context of aviation, the O_3 aCCFs are verified in this chapter.

Preliminary results [124] showed that climate-optimised flight trajectories considering only O_3 aCCFs, do reduce the NO_x-induced O_3 RF. Here, the aim is to extend the preliminary approach by following a more detailed air traffic optimisation procedure (treating lateral and vertical shifts) involving a large variability of O_3 aCCFs. Hartjes *et al.* [40] determined three-dimensional aircraft trajectories while minimizing contrail formation and found vertical trajectory adjustments to be preferable over horizontal trajectory changes. This is an additional motivation to separately investigate the impact of lateral re-routing and vertical re-routing in relation to NO_x-O_3 effects. While the tools required were described inChapter 3, the approach and the specific modelling setup are described in Section 4.2. After describing the procedure and numerical experiments for verifying the O_3 aCCFs (Section 4.3), the simulation results (Section 4.4) are discussed and concluded (Section 4.5).

4.2. Modelling setup

The procedure of evaluating the effectiveness of using O_3 aCCFs during air traffic optimisation for the actual reduction of climate impact (caused by aviation NO_x on O_3) is discussed here from a modelling perspective. This entails the use of numerical simulations with EMAC and other key submodels. Figure 4.1 shows the key steps and submodels required to do this.

After selecting days characterised by large variability of O_3 aCCFs during an arbitrarily chosen year (Section 4.3.1), the numerical experiments (Sections 4.3.2 and 4.3.3) are performed on two of these chosen days. These two days include a typical summer and winter day in the European subcontinent and are thus characterised by different synoptic situations. In order to generate climate-optimised (with respect to O_3 aCCFs) and cost-optimised trajectories (used as a baseline), the AirTraf submodel (Chapter 3) is required. For these two objective functions in AirTraf, both lateral re-routing for a fixed cruise altitude and vertical re-routing while restraining lateral movements are tested. In each of these cases, the NO_x emissions from AirTraf are tagged as a category using the TAGGING submodel (Chapter 3) and their contribution to changes in O_3 is achieved. Lastly, the radiative forcing of these O_3 changes are computed for each of the scenarios using the RAD submodel (Chapter 3) and used as a proxy to compare their climate impact. This leads to information on the viability of the O_3 aCCFs as a tool for obtaining climate-friendly trajectories as well as the impact of lateral and vertical re-routing. In this simulation setup, EMAC (ECHAM5 version 5.3.02, MESSy version 2.54.0) is applied with the T42L31ECMWF resolution, corresponding to a quadratic Gaussian grid of 2.8

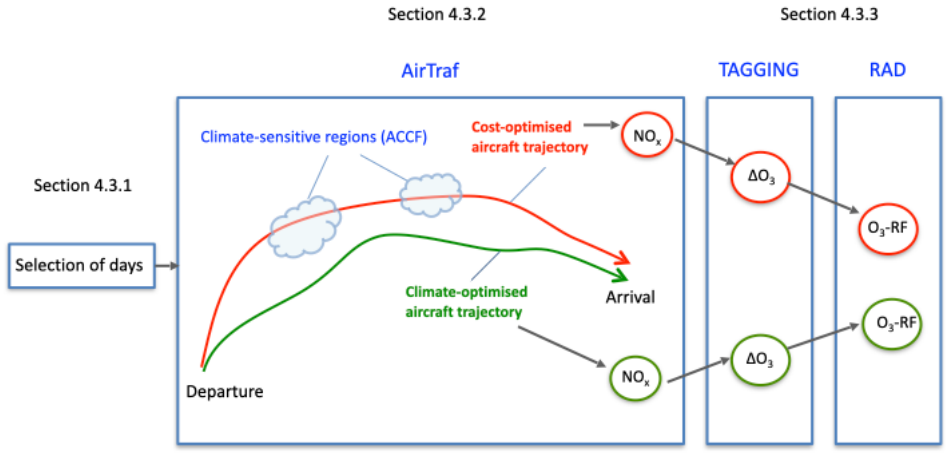

Figure 4.1: Simulation with used submodels, adapted from Yin *et al.* [124]. The blocks are labelled with the corresponding section numbers and it also serves as a roadmap for Section 4.3.

by 2.8° in latitude and longitude and 31 vertical hybrid pressure levels up to 10 hPa (an altitude of roughly 30 km). The vertical resolution at flight levels is roughly 1 km and the simulation time step is 12 minutes. Note that EMAC is run in Quasi-chemical-transport model (QCTM) mode [125] to ensure that the changes from the air traffic emissions do not feed back to the physical and dynamical processes. This is done in order to yield identical synoptic situations for the reference (background) and perturbed (additional NO_x emission) simulations. The complete list of used EMAC submodels in this study can be found in Appendix Appendix B.

4.3. Procedure and numerical experiments

The modelling setup as shown in Figure 4.1 is elaborated in this section. First, there is a one year spin-up simulation in the period from August 2015 until August 2016. This period is more than sufficient to ensure that the model reaches an equilibrium state and minimises the impact of initial conditions on the simulation results. Following this, three steps are performed:

1. Selection of days with a large variability of O_3 aCCFs,

2. Calculation of two aviation emission inventories for each selected day (step 1), i.e., for cost-optimised and O_3 aCCFs optimised aircraft trajectories,

3. Calculation of the contribution of NO_x emissions from step 2 to O_3 mixing ratios and respective RF.

These steps are first discussed in Sections 4.3.1 to 4.3.3 respectively.

4.3.1. Procedure for selection of simulation days

To test the validity of O_3 aCCFs via trajectory optimisation, specific days during which the variation of O_3 aCCFs is large and allows a significant alteration of trajectories when optimising for NO_x-O_3 effects are chosen. In order to determine the variability of O_3 aCCFs, a statistical approach is employed. The variability of O_3 aCCFs for the year 2016 based on ECMWF Re-Analysis Interim data [126] of temperature (T) and geopotential (ϕ) at a typical cruise flight pressure level of 250 hPa is analysed. These forecasts were used because of the finer resolution compared to nudged EMAC data and even smaller differences between these datasets compared to what were highlighted in the previous chapter. For each day, (T, ϕ) are recorded 4 times a day (6 hours between them) and the O_3 aCCFs are calculated offline for the longitude range (20°W to 35°E) and latitude range (25°N to 70°N) corresponding to the European airspace. The unbiased sample variance for each month (Equation (4.1)) is calculated and expressed as a percentage of the monthly mean variance.

$$\sigma^2 = \frac{1}{N-1} \sum_{i=1}^{N} \left(Y_i - \mu\right)^2 , \tag{4.1}$$

where Y_i is the O_3 aCCFs value for each time step with mean μ for $N = 4 \times k$ samples; k refers to the number of days in the specific month. In this context, a day is considered to have significant spatial variability in O_3 aCCFs when the percentage variance exceeds 120%. This threshold is large enough since these days occur only about 6 times a month or 20% of the days in 2016, which can be deduced from Table 4.3 in Section 4.4.1. For example, small variability (Figure 4.2 (a)) and large variability (Figure 4.2 (b)) are compared for two days from March 2016. In Figure 4.2 (a), all the sample values (red) lie below the 120% line (blue), while in Figure 4.2 (b), they lie above the line. Large variability days for 2016 are of particular interest. The O_3 aCCFs corresponding to those days is shown in Figure 4.3. The day characterised by large variability depicts a sharper contrast in the pattern with a distinct boundary separating larger and relatively lower values. The lower and upper peak values have a larger spatial spread for the case with large variability of O_3 aCCFs.

4.3.2. 1-day air traffic simulation

For all synoptic situations, which are selected due to large spatial variability of O_3 aCCFs (see also Section 4.4.1), a cost-optimised and climate-optimised (considering only O_3 aCCFs) simulation is performed. To be specific, the cost-optimised simulation entails Simple Operating Cost (SOC), considering only flight time and fuel consumption [110] and is the baseline scenario. For each optimisation objective, the optimisation has been performed in two ways:

- Lateral re-routing: The flight corridor is fixed at an altitude of FL340 which corresponds to a typical cruise pressure level of 250 hPa by using constant vertical design variables (labelled $x_7, \ldots, x_{11}$ in Figure 5 of Chapter 3). This way, the trajectory is optimised in terms of lateral re-routing called the Horizontal Analysis (HA). It is indeed artificial to fix a cruise flight altitude, but this is done to analyse lateral shifts in trajectories for the two routing objectives.

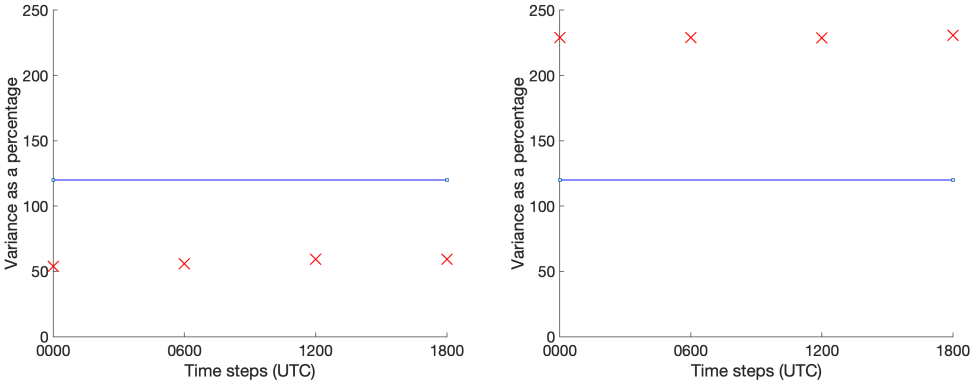

Figure 4.2: Variability of O_3 aCCFs expressed in terms of percentage variance at 250 hPa: **(a)** Small variability (18th March 2016) and **(b)** Large variability (1st March 2016). The blue line indicates the 120% line; and the samples are marked by red 'x' and correspond to 4 times (in UTC) of the day where data are available. Note that these samples represent averaged values over the chosen latitude and longitude range.

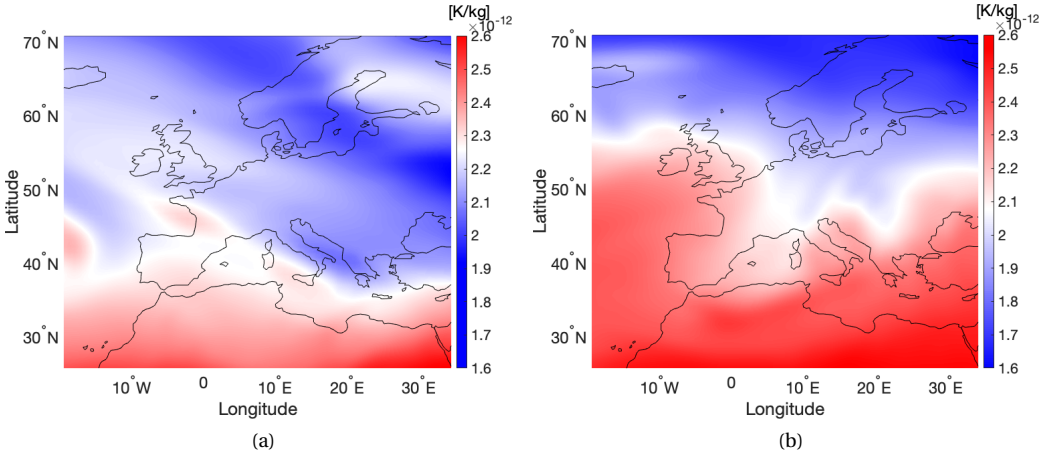

Figure 4.3: O_3 aCCFs [K/kg(NO_2)] at 250 hPa at 0000 UTC for two days of **(a)** small variability (18th March 2016) and **(b)** large variability (1st March 2016)

- Vertical re-routing: The dashed boxes controlled by $x_1, \ldots x_6$ (Figure 5 of Chapter 3) are fixed to the centre points of their respective rectangular domains. This way, the trajectory is laterally constrained and vertically optimised based on the depth of the cruise flight corridor called the Vertical Analysis (VA).

With this approach, it is possible to assess the climate impact mitigation potential in terms of O_3-RF on the basis of different re-routing approaches, after being subjected to the same synoptic situations. The above settings are used as inputs to ARMOGA to optimise trajectories with regard to SOC and climate impact of NO_x-O_3 effect in separate simulations. More details regarding the simulation and the flight plan are listed in Table 4.1.

4.3.3. 4-month chemistry-climate simulation

Following the 1-day air traffic simulation, the NO_x emission data of the corresponding flights are recorded and input into a 4-month chemistry-climate simulation. The contribution of the AirTraf NO_x emissions to the tropospheric mixing ratios of NO_y (all active nitrogen species) and O_3 is tracked over the simulation period using the TAGGING submodel. This duration of four months is sufficient to record the effect of NO_x emissions and has been proposed by other studies (e.g., [33, 39, 75, 83]). The concentration and subsequent impact of emissions from the cost- and climate-optimised flights can be evaluated in detail. Finally, using the submodel RAD, the radiation budget is calculated (see also Figure 4.1). Note that the atmosphere also contains background emissions from other sources such as aircraft, ships, road traffic, biomass and agricultural waste burning and other anthropogenic non-traffic emissions. Lastly, there are lightning NO_x emissions that are calculated online using the parameterisation described by Grewe *et al.* [127].

To summarise the simulation setup based on Sections 4.3.1 to 4.3.3, after selecting two representative winter and summer days characterised by large spatial variability of O_3 aCCFs, there is a 1-day air traffic simulation on each of these days, which is followed by a chemistry-climate simulation that calculates mixing ratios of NO_y and O_3 due to resulting aviation NO_x emissions over a 4-month period (Table 4.2). In the latter, the

Table 4.1: 1-day air traffic simulation setup.

Parameter	**Optimisation objective**	
	Cost optimised and **Climate optimised** (O_3 aCCFs)	
EMAC resolution	T42L31ECMWF (2.8° × 2.8°)	
Time step of EMAC	12 minutes	
Waypoints	101	
Design variables	11 (6 locations and 5 altitudes)	
Flight plan	85 European flights	
Aircraft type	A330-301	
Engine type	CF6-80E1A2, 2GE051 (with 1862M39 combustor)	
Flight Mach number	0.82	
Cruise flight altitude	Lateral re-routing	Vertical re-routing
	FL340 ≈ 10.4 km	[FL290, FL410] ≈ [8.8, 12.5] km

radiation budget is also calculated. The analysis is split into two components namely HA and VA in order to assess the horizontal and vertical pattern of O_3 aCCFs and the climate impact from these different re-routing procedures. In total, 16 simulations were performed.

4.4. Results

First, the simulation days based on the procedure discussed in Section 4.3.1 are described in Section 4.4.1. A winter and summer day are chosen followed by the analysis of air traffic optimisation results for lateral and vertical re-routing in Section 4.4.2. In Section 4.4.3, the results from the chemistry-climate simulation are discussed for the two selected days. The influence of the synoptic situation on the transport of NO_x and the subsequent NO_y and O_3 contributions is shown. Finally, the overall climate impact is derived and compared for all simulations in terms of O_3-RF caused by optimised air traffic in Section 4.4.4.

4.4.1. Selection of simulation days

Following the procedure described in Section 4.3.1, the days with large variability of O_3 aCCFs for the year 2016 are listed in Table 4.3. There is no specific pattern in how they are distributed. Here, a winter day (1st February) and a summer day (1st August) are chosen arbitrarily from the list which have a percentage variance of ≈ 134% and ≈ 144%, respectively. Any day would be an equally good choice, but days that are seasonally opposites are chosen because the synoptic situation on these days may be linked to the summer and winter weather patterns documented by Irvine *et al.* [95].

Synoptic situation

The synoptic situation for the selected winter and summer day are shown in Figure 4.4 (a) and (b), which are comparable to the winter (W3) pattern and summer (S2) pattern of Irvine *et al.* [95], respectively. The selected winter day (Figure 4.4 (a)) is characterised by the presence of high and low geopotential height anomalies [128], which indicate the presence of high pressure (H) and low pressure (L) systems (see H and L in Figure 4.4), respectively. The high pressure system and high wind speeds (up to 60 m/s) that dominate the European airspace, are expected to induce a south and downward transport of the bulk of emitted species. On the other hand, the selected summer day (Figure 4.4 (b)) is characterised by a zonal jet that is relatively slow (≈ 35 m/s) and with a smaller variation in the field. The synoptic situation on this day is expected to transport the bulk of emitted species to higher latitudes (> 50°N).

Table 4.2: Complete simulation setup.

Simulation type	Simulation length	Season		Objective function		Analysis		# runs
Air traffic optimisation	1 day	Winter	Summer	Cost	Climate	HA	VA	8
Atmospheric impacts	4 months	Winter	Summer	Cost	Climate	HA	VA	8

Table 4.3: Days with large variability of O_3 aCCFs in the year 2016.

Month	Day of the month
January	8-15, 30, 31
February	1-3
March	1-6, 22, 24
April	24-26, 28, 29
May	1-3, 12-14, 16, 18, 19
June	12-16
July	12, 13, 30, 31
August	1, 4, 5, 26-29
September	1-3, 5, 23, 27-30
October	1-3, 24
November	5, 6, 9
December	6, 7, 10, 11, 24, 26

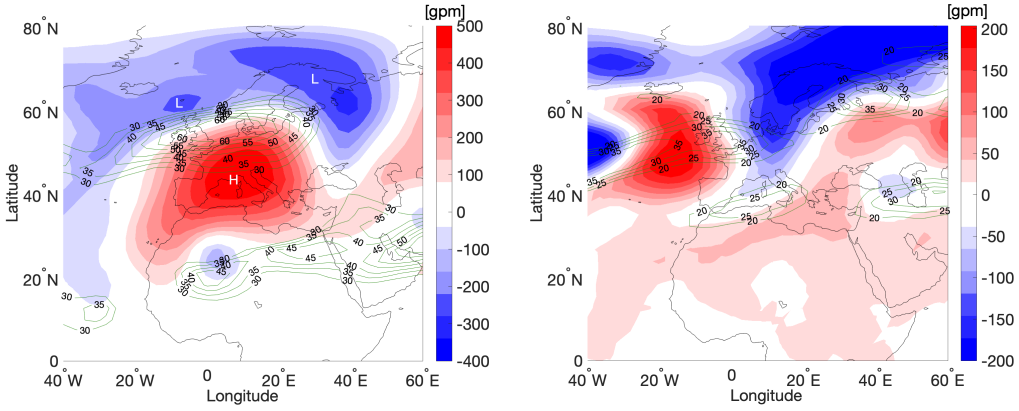

(a) (b)

Figure 4.4: Daily mean geopotential height anomaly (red–blue contours, in geopotential meter (gpm)) and zonal wind speed (green contours with interval 5 m/s) at 250 hPa for **(a)** 1st February 2016, with wind speeds from 30 to 60 m/s, **(b)** 1st August 2016, with wind speeds from 20 to 35 m/s. “H" and “L" represent the high and low geopotential height anomalies.

O_3 aCCFs pattern

The estimated impact of NO_x emissions on O_3 for the selected winter and summer day is shown in Figure 4.5 (b) and Figure 4.6 (b), respectively. Since the O_3 aCCFs are functions of temperature and geopotential (Chapter 3), the corresponding isolines are also depicted in Figures 4.5 and 4.6. For the selected winter day, Figure 4.5 (b) shows that lower (higher) latitudes are characterised by larger (smaller) values of O_3 aCCFs due to larger (smaller) values of temperature and geopotential in these regions [74]. That is, for example, the Mediterranean region is characterised by large values of O_3 aCCFs while regions close to Iceland are characterised by low values of O_3 aCCFs. There are slight similarities between the synoptic situation and the O_3 aCCFs: the geopotential lines (Figure 4.5 (a)) are similar in structure to the colour contours (Figure 4.5 (b)). The O_3 aCCFs shows large values and hence strong warming effects in lower latitudes, where the bulk of emitted species are expected to be transported (Figure 4.4 (a) and their pathway indicated by the geopotential lines in Figure 4.5 (a)).

For the selected summer day, Figure 4.6 (b) similarly shows that lower (higher) latitudes are characterised by larger (smaller) values of O_3 aCCFs due to larger (smaller) values of temperature and geopotential in these regions. There are slight similarities between the synoptic situation and the O_3 aCCFs: the geopotential lines (Figure 4.6 (a)) are similar in structure to the colour contours (Figure 4.6 (b)). The temperature is higher (isolines in Figure 4.6 (b)) compared to 1st February (isolines in Figure 4.5 (b)) with a very different geopotential field. Consequently, the O_3 contribution from NO_x emissions estimated by the O_3 aCCFs is also larger. However, the synoptic situation on the selected summer day (Figure 4.4 (b) and the pathway of the emissions as indicated by geopotential lines in Figure 4.6 (a)) is expected to transport emitted NO_x to higher latitudes (> 40° N). Yet, O_3 effects are predicted to be stronger at the lower latitudes by the O_3 aCCFs, owing to the strong dependence on temperature and geopotential, which is a limitation (Figure 4.6 (b)).

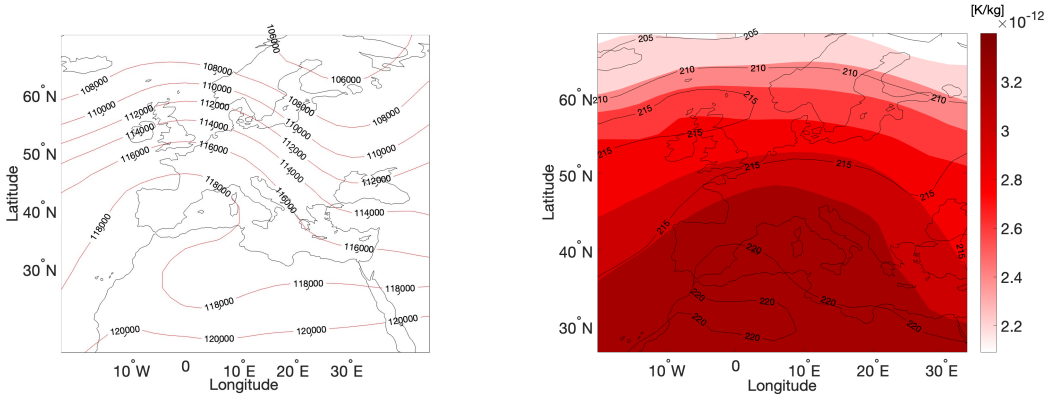

Figure 4.5: Meteorological parameters and O_3 aCCFs at 250 hPa on 1st February 2016: **(a)** Geopotential (isolines, m^2/s^2) **(b)** Temperature (isolines, K) and O_3 aCCFs (colour contours, $K/kg(NO_2)$).

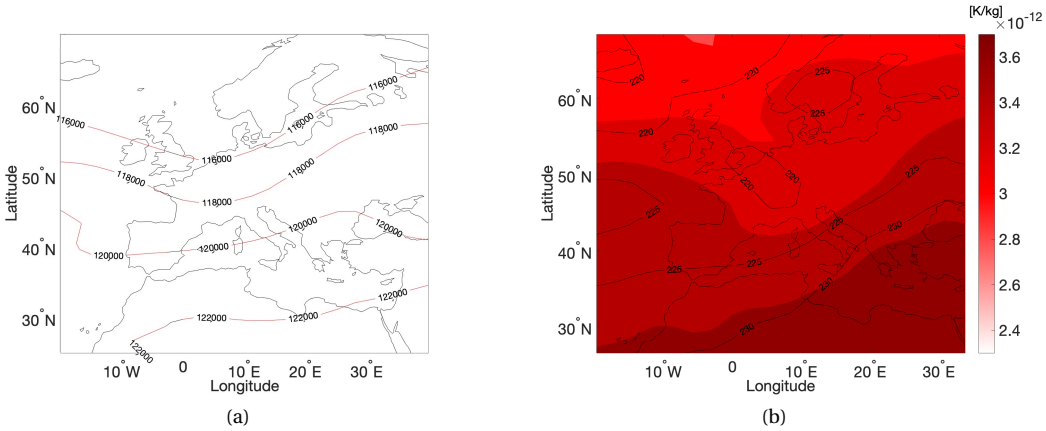

(a) (b)

Figure 4.6: Meteorological parameters and O_3 aCCFs at 250 hPa on 1st August 2016: **(a)** Geopotential (isolines, m^2/s^2) **(b)** Temperature (isolines, K) and O_3 aCCFs (colour contours, K/kg(NO_2).

The vertical distribution of O_3 aCCFs for the selected days can be visualised by plotting its meridonial mean in the European area as shown in Figure 4.7. The pressure levels [315, 180] hPa correspond roughly to the flight corridor within [FL290, FL410]. Most of the climate sensitive regions lie at higher altitudes.

4.4.2. Optimised air traffic

In this section, the results for the 1-day air traffic simulation for lateral re-routing on the selected winter and summer days are analysed. There are 85 flights in the flight plan and the flight altitude is fixed at FL340, corresponding to a typical cruise pressure level of 250 hPa (Table 4.1). Therefore, only lateral changes in the routing for cost-optimised (blue) and climate-optimised (red) flights are seen on the chosen winter day and summer day (Figure 4.8), respectively. Since the flight trajectories are essentially curves and hence functions, the relative change of climate-optimised flights with respect to cost-optimised flights can be computed in $\mathbb{R}^2$ (since cruise altitude is fixed). The $\mathcal{L}^2$ norm [129], given by $|\boldsymbol{d}|_2 = \left[\sum_i |d_i|^2\right]^{1/2}$ is used to compute the deviation $\boldsymbol{d}$ between each climate- and cost-optimised flight considering each trajectory point, i. The maximum deviation, considering all flights, is found to be $\approx$ 11.5 % and $\approx$ 6.5 % on the selected winter and summer day, respectively. The mean lateral deviation for all the flight trajectories was found to be $\approx$ 1% on both the selected days. In most cases, climate-optimised flights are shifted to the North, where the O_3 impact is predicted to be lower (Figure 4.5 (b) and Figure 4.6 (b)).

In the case of vertical re-routing, the lateral changes for cost- and climate-optimised flights are fixed. Figure 4.9 (a) and Figure 4.9 (b) illustrate the vertical changes of climate-optimised (red) and cost-optimised (blue) flights on the selected winter and summer days, respectively. The vertical shift in trajectories is calculated using the same procedure, while laterally, flight trajectories remain unchanged. The maximum deviation between the climate-optimised and cost-optimised flight trajectories is found to be $\approx$ 22

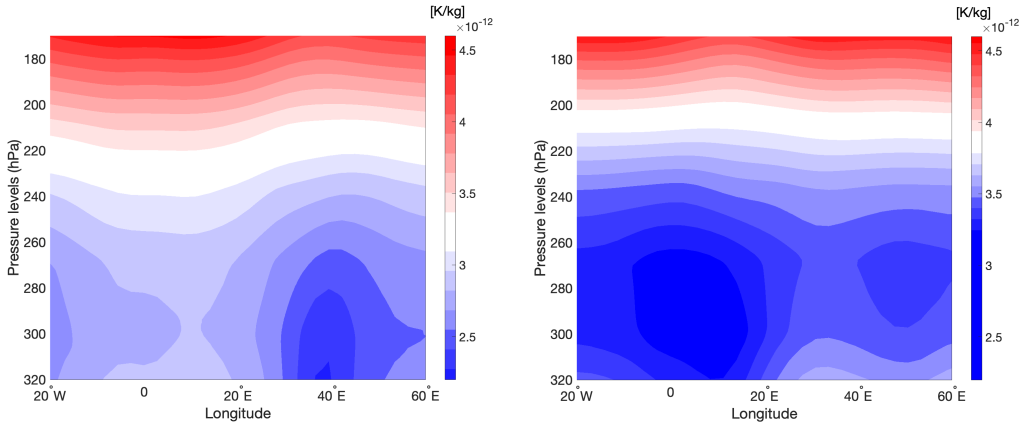

Figure 4.7: Meridonial mean O_3 aCCFs on **(a)** 1st February 2016 and **(b)** 1st August 2016. Pressure levels (hPa) correspond to cruise flight levels used for vertical re-routing.

% and ≈ 26 % on the selected winter and summer day, respectively. The mean vertical deviation for all the flight trajectories is found to be ≈ 7.5% and ≈ 5.5% on the selected winter and summer day, respectively. Therefore, in the case of vertical re-routing, the differences between flight trajectories are considerably larger than in lateral re-routing.

For the vertically re-routed cost-optimised flights, there are no significant quantitative differences in flight altitude for two selected days. This is because the total cost mainly depends on the flight time and fuel consumption. To reduce the flight time, aircraft fly along a jet stream and to reduce the fuel cost, aircraft stay at higher altitudes. As the optimiser considers both effects, it found that there is a bigger advantage to fly higher for the two selected days. This also implies that the synoptic situation that is relevant for the contribution of O_3 from NO_x emissions does not play a major role in the cost optimisation. On the contrary, for O_3 aCCFs optimised flights, large differences are seen in the two days which indicates that the situation is more complex as NO_x-O_3 effects depend on various factors as discussed in Chapter 2. The climate sensitive regions lie more at higher altitudes (Figure 4.7), and O_3 aCCFs optimised flights avoid the most sensitive regions by flying lower. On the selected winter day, there is a tendency for many flights to drift to lower altitudes at eastward longitudes (Figure 4.9 (a)). On the selected summer day, many flights seem to prefer flying even lower than in winter at ≈ 10000 m (Figure 4.9 (b)); however, a few flights also move to slightly higher altitudes (around 12000 m, i.e. corresponding to ≈ 190 hPa). The choice of lower altitudes for mitigating the climate impact of NO_x has also been reported in various studies e.g., [34, 35, 130–133].

Table 4.4 summarises the fuel consumption, the amount of NO_x emitted and the mean emission index of NO_x ($EINO_x$) for each case that is considered. In all cases of lateral re-routing, the amount of fuel consumption and NO_x is almost the same for cost-optimised and climate-optimised flights. For vertical re-routing, in both, winter and summer, climate-optimised flights consume ≈ 4% more fuel. In winter they emit ≈ 8%

more NO_x than cost-optimised flights, and in summer ≈ 3.5% more NO_x than cost-optimised flights. Therefore, for vertical re-routing, higher overall emissions for the climate-optimised case are seen, which is consistent with results from Yin *et al.* [124].

4.4.3. Atmospheric composition changes from re-routing

The TAGGING submodel tracks the contribution of the NO_x emissions from the optimised air traffic to the tropospheric NO_y and O_3 mixing ratio from the time at which the emissions are released until the four-month simulation period is complete. These fields are denoted as NO_y`atf` and O_3`atf`, respectively. Since the synoptic situations on the two selected days are different, the results for the two days are separated.

Case study for selected winter day

Figure 4.10 (a) and Figure 4.10 (b) illustrate the patterns for the zonal mean of NO_y`atf`, taken along the longitudes, one week since the emissions are released from laterally re-routed and vertically re-routed climate-optimised flights, respectively. Since the transport pathways of emissions are essential in the first week(s), the result is shown for 8th February. The patterns look similar in both cases, with peak values located at lower altitudes (≈ 600 to 700 hPa) and lower latitudes (≈ 20° N), approaching towards the equator. However, in the case of vertical re-routing, large values are also spread across the vertical pressure levels (≈ 200 to 400 hPa). Therefore, the location of the bulk of emissions are at lower latitudes and altitudes, which is to be expected from the synoptic situation (Figure 4.4 and Figure 4.5 (a)).

The difference of the zonal mean O_3`atf` mixing ratios between climate- and cost-optimised flights on the selected winter day is depicted in Figure 4.11. In the case of lateral re-routing (Figure 4.11 (a)), the O_3`atf` mixing ratio is larger for cost-optimised flights. In winter, there is less photo-chemical activity in general; the climate optimised flights are using predominantly higher latitudes, whereas the cost optimised flights use predominantly lower latitudes. As the photochemical activity is more prominent at lower latitudes, the O_3`atf` mixing ratio decreases considerably for climate optimised flights. In the case of vertical re-routing (Figure 4.11 (b)), the climate-optimised flights use preferably lower flight altitudes (Figure 4.9 (a)), where higher O_3 change occurs. This matches with the results from the air traffic optimisation (Figure 4.9 (a)), where most climate-optimised flights took place at low altitudes. The region of O_3`atf` change is crucial for the resulting RF, which is shown in Section 4.4.4.

The four green dotted boxes represent the regions between 200 hPa and 400 hPa, 400 and 1000 hPa, for areas above and below 50 °N where changes in NO_y`atf` and O_3`atf` are investigated. These regions correspond to approximate cruise and non-cruise altitudes for lower and higher latitudes. Figure 4.12 shows the time series of the mass of NO_y`atf`

Table 4.4: Fuel consumption, NO_x emissions and mean $EINO_x$ from laterally and vertically re-routed flights.

Optimisation objective	**Selected day**	**Fuel consumption** [$\times 10^3$ kg]		**NO_x emission** [$\times 10^6$ g(NO_2)]		**$EINO_x$** [g(NO_2)/kg(fuel)]	
		Lateral	Vertical	Lateral	Vertical	Lateral	Vertical
Cost-optimised	Summer	815	742	10.3	8.92	12.6	12
	Winter	813	747	9.18	7.52	11.3	10.1
Climate-optimised	Summer	816	771	10.2	9.23	12.5	12
	Winter	815	777	9.15	8.15	11.2	10.5

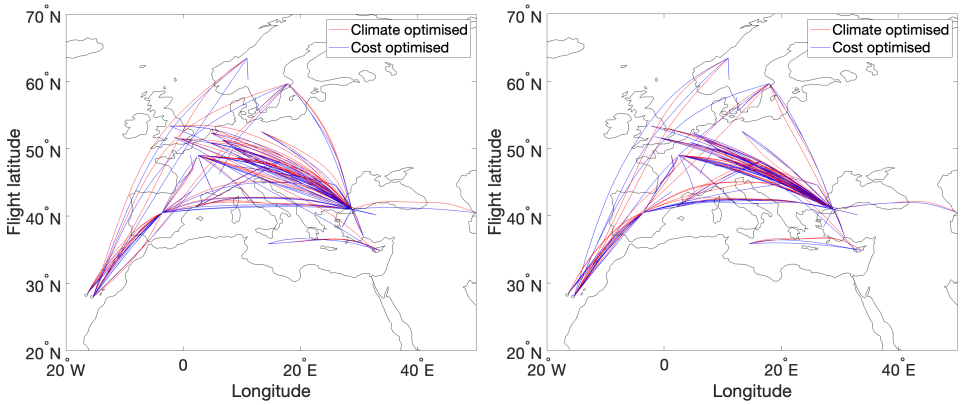

Figure 4.8: Horizontal profile of optimised routes with respect to costs (blue) and climate (red) with a fixed cruise altitude of FL340 (≈ 250 hPa) for **(a)** 1st February 2016 and **(b)** 1st August 2016. The flight altitude is fixed at 250 hPa.

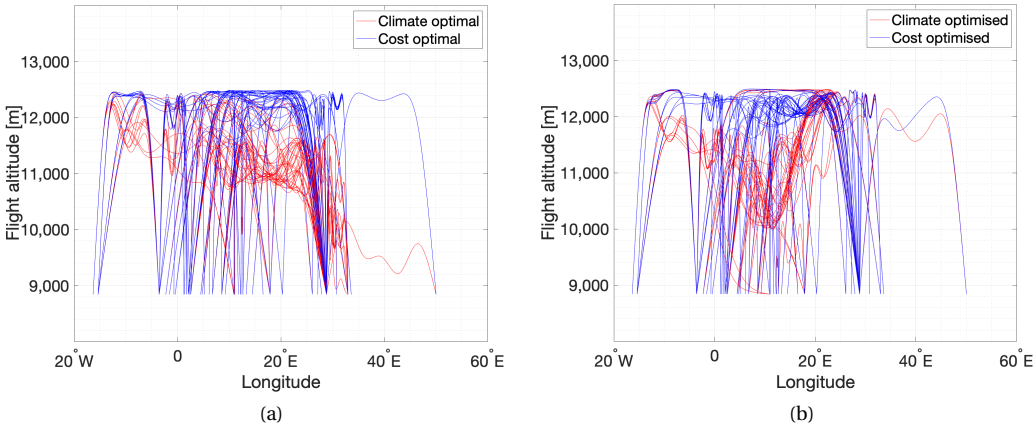

Figure 4.9: Vertical profile of optimised routes with respect to costs (blue) and climate (red) with a variable cruise altitude (within [FL290, FL410]) for **(a)** 1st February 2016 and **(b)** 1st August 2016. Note that lateral movements are restrained.

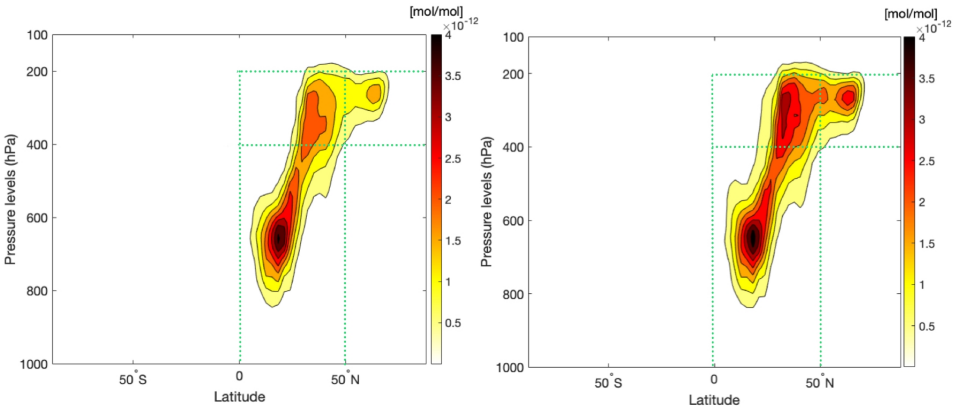

Figure 4.10: Zonal mean mixing ratio of NO_y`atf` [mol/mol] for climate-optimised **(a)** lateral re-routing and **(b)** vertical re-routing, on 8th February 2016, a week after the release of the emissions. The green dotted boxes indicate four regions of interest, where further analysis is carried out. See text for details.

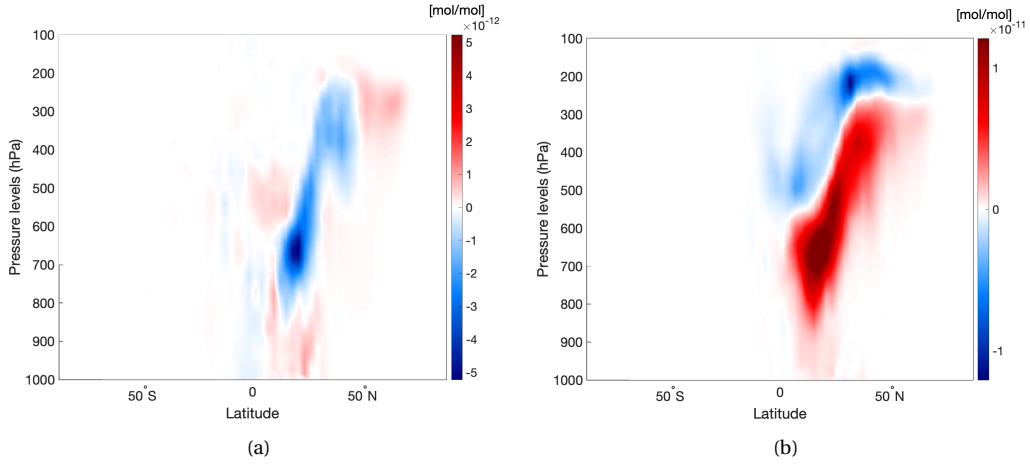

Figure 4.11: Difference of the zonal mean O_3`atf` mixing ratio [mol/mol] between climate-optimised flights and cost-optimised flights on 8th February 2016, a week after the release of the emissions for **(a)** lateral re-routing and **(b)** vertical re-routing.

in these regions for all the climate and cost-optimised simulations on the selected winter day. For the conversion of NO_yatf from volume mixing ratio to mass, the molar mass of nitrogen (N) [14 kg/kmol] is used throughout this study. The regions where most of the NO_yatf is present are (a) and (b) of Figure 4.12. In the first few days of the simulation, most of the NO_yatf is present in the former region (i.e., at cruise level altitudes), thereafter the bulk is transported to the latter region (i.e., lower altitudes). Additionally, the deviation in the time series of NO_yatf between climate-optimised and cost-optimised simulations is larger for vertical re-routing than for lateral re-routing. Finally, regions (c) and (d) don't show significant activity.

Similarly, Figure 4.13 shows the time series of the mass of O_3atf in these regions for the climate- and cost-optimised simulations on the selected winter day. In the first five days of the simulation, the O_3atf mass peaks in region (a), but thereafter, the bulk of O_3atf rises rapidly in region (b), i.e., at lower altitudes corresponding to 400 to 1000 hPa. On the contrary, the other two regions, which correspond to higher latitudes, are characterised by very low amounts of O_3atf. Also, more O_3atf is produced from cost-optimised simulations compared to climate-optimised simulations, which is expected to lead to higher O_3-RF (Section 4.4.4).

Case study for selected summer day

Figure 4.14 (a) and Figure 4.14 (b) illustrate the zonal mean NO_yatf, one week since the emissions are released from laterally re-routed and vertically re-routed climate-optimised flights, respectively. These patterns are distinct from the winter case (Figure 4.10). In the case of lateral re-routing (Figure 4.14 (a)), there is a localised peak at cruise level (≈ 250 hPa) and towards the North pole (≈ 80°N). In the case of vertical re-routing (Figure 4.14 (b)), there are two distinct peaks, also concentrated at cruise altitudes (≈ 200 hPa and 300 hPa) either upper mid-latitudes (≈ 50°N) or close to the North pole (≈ 80°N). In both cases of the selected summer day, the bulk of emissions can be found at high altitudes and towards higher latitudes (> 50° N), which is to be expected from the synoptic situation (Figure 4.4 (b) and Figure 4.6 (a)).

The difference of the zonal mean O_3atf mixing ratios between climate- and cost-optimised flights on the selected summer day is depicted in Figure 4.15. There is a strong contrast to the winter case (Figure 4.11). In summer, there is a lot more photochemical activity than in winter and hence the difference in O_3atf mixing ratio does not have a single localised peak. This is especially clear for lateral re-routing (Figure 4.15 (a)), where the O_3atf mixing ratio is seen to be mainly larger for cost-optimised flights. In the case of vertical re-routing (Figure 4.15 (b)), most climate-optimised flights take place at lower altitudes (Figure 4.9 (b)). This results in higher O_3atf mixing ratios in general, larger for climate-optimised flights. This matches with the results from the air traffic optimisation (Figure 4.9 (b)), where most climate-optimised flights took place at lower altitudes compared to cost-optimised flights. The region of O_3atf change is crucial for the resulting RF, which is shown in Section 4.4.4.

The green dotted boxes in Figure 4.14 indicate four regions of interest, that are further investigated. Figure 4.16 shows the time series of the mass of NO_yatf in these regions for all the climate- and cost-optimised simulations on the selected summer day. The regions where most of the NO_yatf is present are (a), (b) and (c) of Figure 4.16. In the first two

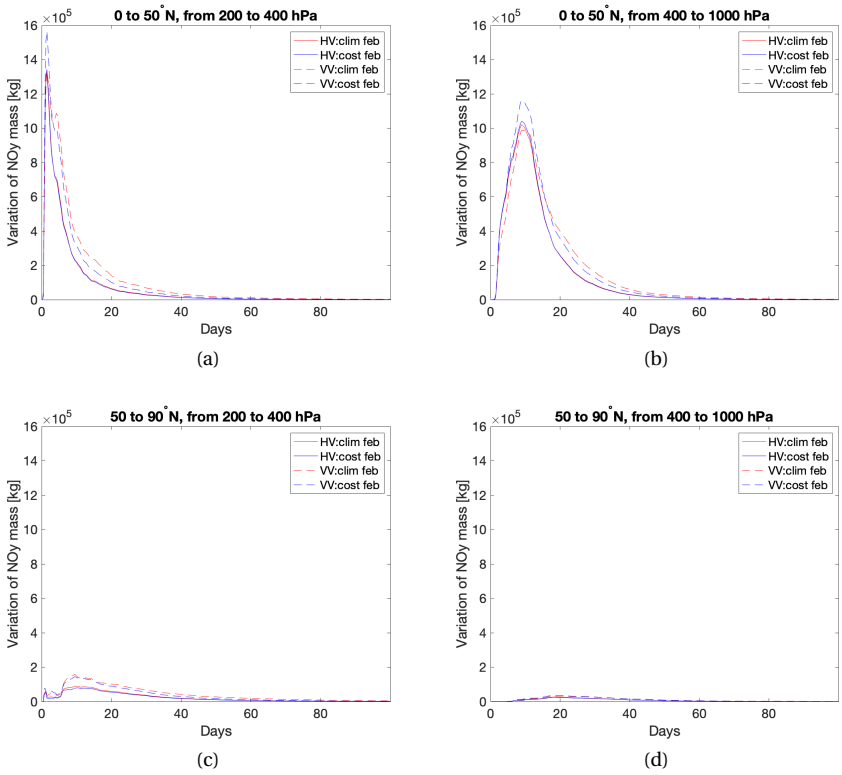

Figure 4.12: Time series of NO_y`atf` mass [kg(N)] in specific regions from chemistry-climate simulations starting on 1st February 2016. The red and blue lines indicate the climate-optimised and cost-optimised cases, respectively, and the panel titles in **(a)**, **(b)**, **(c)** and **(d)** indicate the investigated regions.

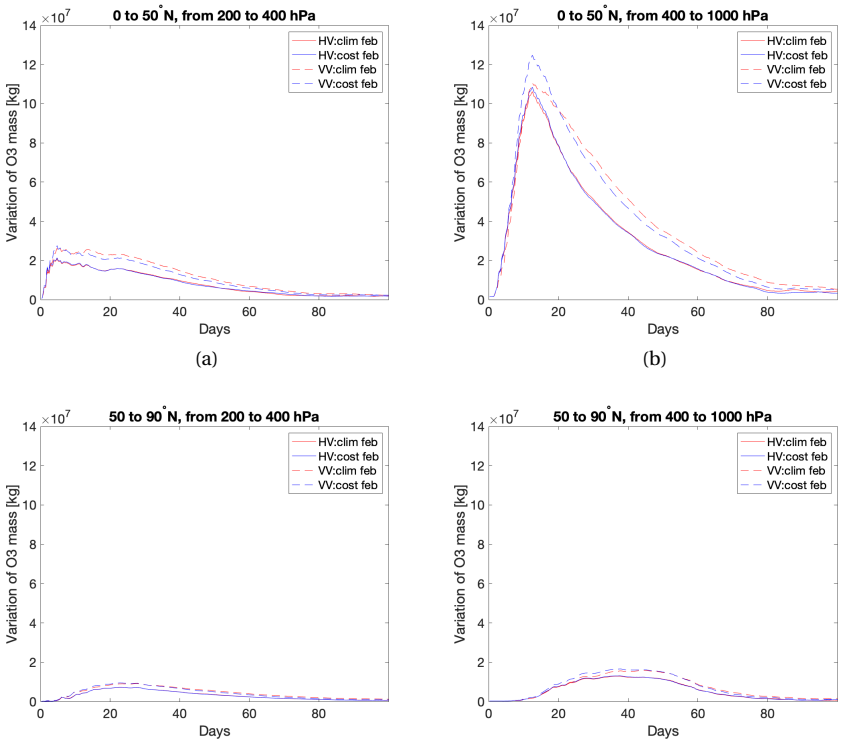

Figure 4.13: Time series of O_3`atf` mass [kg] in specific regions from chemistry-climate simulations starting on 1st February 2016. The red and blue lines indicate the climate-optimised and cost-optimised cases, respectively, and the panel titles in **(a)**, **(b)**, **(c)** and **(d)** indicate the investigated regions.

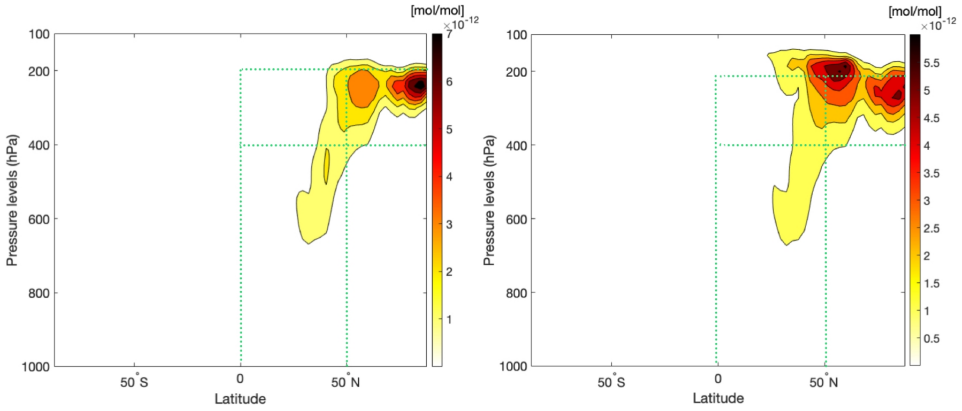

Figure 4.14: Zonal mean mixing ratio of NO_y`atf` [mol/mol] for climate-optimised **(a)** lateral re-routing and **(b)** vertical re-routing on 8th August 2016, a week after the release of the emissions. The green dotted boxes indicate four regions of interest, where further analysis is carried out. See text for details.

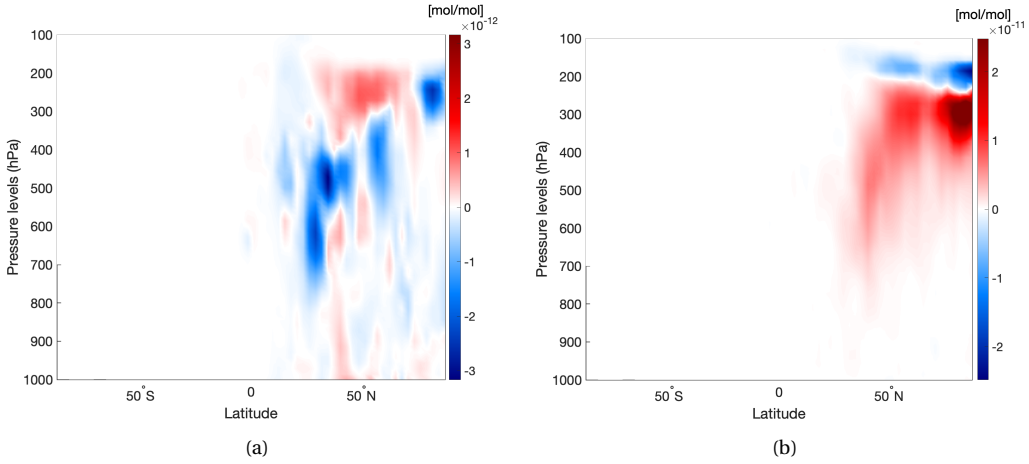

Figure 4.15: Difference of the zonal mean O_3`atf` mixing ratio [mol/mol] between climate-optimised flights and cost-optimised flights on 8th August 2016, a week after the release of the emissions for **(a)** lateral re-routing and **(b)** vertical re-routing.

days of the simulation, most of the NO_yatf is present in region (a) (i.e., at cruise level altitudes). A part of it is transported to region (c) (i.e., higher latitudes but at cruise level) and after a few days, NO_yatf is transported to region (b) (i.e., lower altitudes). After one week, region (b) is seen to have the highest amount of NO_yatf. Finally, the deviation in the time series of NO_yatf between climate-optimised and cost-optimised simulations is larger for vertical re-routing than for lateral re-routing.

Similarly, Figure 4.17 shows the time series of O_3atf mass in these regions for all the climate- and cost-optimised simulations on the selected summer day. In all four regions of Figure 4.17, the O_3atf mass is seen to rise with the bulk of O_3atf rising rapidly in region (b) after one week, i.e., at lower altitudes corresponding to 400 to 1000 hPa but within 0 to 50° N. Also, more O_3atf is produced from cost-optimised simulations compared to climate-optimised simulations, which is expected to lead to higher O_3-RF (Section 4.4.4).

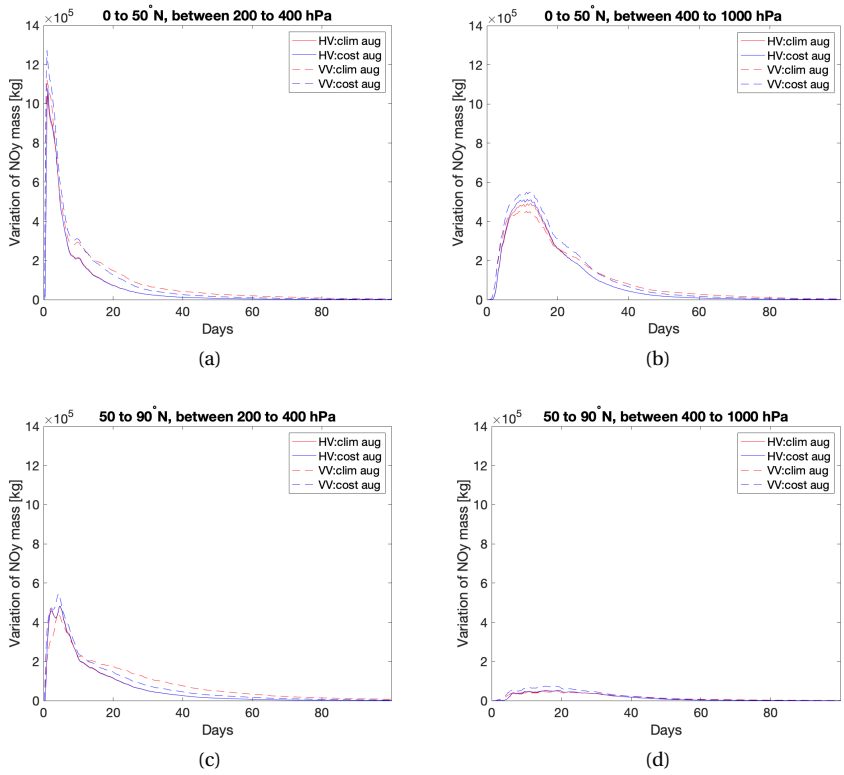

Figure 4.16: NO_yatf mass [kg(N)] time series in specific regions from chemistry-climate simulations starting on 1st August 2016. The red and blue lines indicate the climate-optimised and cost-optimised cases respectively and the panel titles in **(a)**, **(b)**, **(c)** and **(d)** indicate the investigated regions.

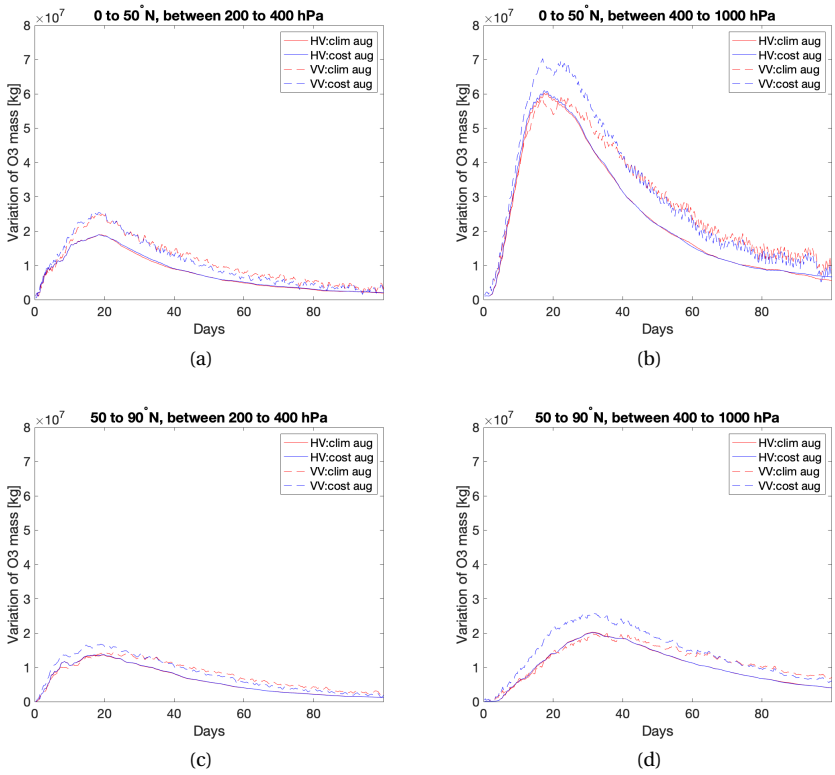

Figure 4.17: O_3`atf` mass [kg] time series in specific regions from chemistry-climate simulations starting on 1st August 2016. The red and blue lines indicate the climate-optimised and cost-optimised cases respectively and the panel titles in **(a)**, **(b)**, **(c)** and **(d)** indicate the investigated regions.

4.4.4. Radiative forcing

The mean O_3-RF from AirTraf NO_x over the 4-month chemistry-climate simulation period for all the simulations are listed in Table 4.5. First and foremost, it can be seen that O_3-RF is larger for cost-optimised simulations compared to climate-optimised simulations. This corroborates the findings of Yin *et al.* [124]. The summer flights lead to larger climate impact than the winter flights in terms of O_3-RF, because of greater photochemical activity in summer, indicating stronger NO_x-O_3 effects in summer, which supports previous studies [19, 33].

For lateral optimisation, i.e., for a fixed cruise level of 250 hPa, the O_3-RF is lower compared to vertical optimisation despite larger fuel consumption and NO_x emitted compared to those for the vertical re-routing (Table 4.4). Looking back at the mixing ratio of NO_y for lateral re-routing, it can be seen in Figure 4.10 (a) and Figure 4.14 (a) that the peak values are less dispersed compared to vertical re-routing. For both of the selected days (Figure 4.10 (b) and Figure 4.14 (b)), the peaks are separated and are at significantly different pressure levels ($\approx$ 650 hPa and $\approx$ 300 hPa) in winter, and at different latitudinal locations ($\approx$ 55°N and $\approx$ 85°N) in summer. Additionally, the NO_y field

is more dispersed in the vertical re-routing case, which means that it is less influenced by atmospheric processes such as wash-out and dry deposition compared to the lateral re-routing case. Lastly, the time series of O_3 mass in Figures 4.13 and 4.17 indicate lower values for lateral re-routing compared to vertical re-routing. As a result, the O_3-RF from vertical re-routing is larger compared to that from lateral re-routing.

So far, no studies are available that have analysed the mean O_3-RF based on aviation NO_x emissions occurring on a single day. Yin et al. [124] reported a mean O_3-RF of ≈ 13 mW/m^2, but this involved an air traffic simulation for the same flight plan as used in this study, repeated every day for a period of 90 days (as opposed to a single day in the present study). Since radiative calculations are non-linear, it is not possible to make a direct and accurate comparison between these two studies. However, taking a rough estimate, the mean RF that can be attributed to a single day is $\frac{13}{90}$ mW/m^2 ≈ 140 μW/m^2, which has the same order of magnitude as the values listed in Table 4.5. Other studies, such as Lee et al. [62] and Lee et al. [52] provide best estimates of global aviation RF of 26.3 mW/m^2 and 36.0 mW/m^2, respectively from short term O_3 change based on several aviation NO_x emission inventories.

Finally, the difference between climate- and cost-optimised flights in mean O_3-RF over the period of four months is larger for vertically re-routed flights, which can be attributed to the larger difference in O_3 mixing ratios compared to that from laterally re-routed flights (Figures 4.13 and 4.17). The largest reduction of 20% occurred for vertically re-routed flights on the selected summer day while the smallest reduction of 0.5% occurred for laterally re-routed flights on the selected winter day (Table 4.5).

Table 4.5: Comparison of mean RF of O_3 from optimised air traffic for emissions as given in Table 4.4.

Air traffic optimised on	**Type of analysis**	**Mean RF of O_3 [μW/m^2]**		**% reduction**
		Cost-optimised	Climate-optimised	
Winter day	Horizontal	84.1	83.7	0.5
	Vertical	96.9	94.6	2.4
Summer day	Horizontal	96.4	95.6	0.8
	Vertical	148	119	20

4.5. Discussions and conclusions

The possibility of reducing aviation's overall climate impact requires us to take into account various non-CO_2 effects such as H_2O, contrails, aerosols and NO_x effects on O_3 and CH_4. This study looked specifically into short term NO_x effects on changes in O_3 mixing ratios, a phenomenon that is governed by several competing factors such as emission location and time, synoptic situation, transport pathways and photochemical activity. The prototype O_3 aCCFs were introduced as a tool to facilitate the prediction of O_3 CCFs by means of instantaneous weather data (temperature and geopotential) without the need of the computationally expensive procedure of recalculating CCFs. However, this comes at a cost of larger uncertainties and lower accuracy, which necessitates a study to test its validity. Hence, the hypothesis was that O_3 aCCFs can mitigate short-term aviation NO_x-O_3 effects compared to cost-optimised flights for days characterised by large spatial variability of O_3 aCCFs. It can be concluded that the O_3 aCCFs do enable a reduction of O_3 RF.

Days selected with large variability of O_3 aCCFs were chosen (Section 4.4.1) to assess if a large reduction in climate impact is possible for contrasting synoptic situations. The findings were positive and comply with the findings conducted by Yin *et al.* [124]. The impact of the weather situation on the selected winter and summer day and subsequent transport pathways proved to be very crucial in the climate impact of flights as was discussed in earlier studies (e.g., [33, 38, 74]). While looking into detailed 1-day air traffic optimisation, it was found that on average, for climate-optimised flights, there was a much larger deviation in vertical re-routing compared to lateral re-routing. Although laterally re-routed flights consumed more fuel and emitted more NO_x than vertically re-routed flights, the climate impact was still lower. This can be attributed to the location and spread of NO_x emissions and possibly the choice of cruise level. It would help extending the analysis to other cruise levels to test the sensitivity of changes in O_3 mixing ratios and the subsequent RF, as the corresponding findings can also be compared with other studies (e.g., [19, 21, 35]). For vertically re-routed flights, the difference in O_3-RF between climate- and cost-optimised flights (and hence climate mitigation potential) was found to be larger than for laterally re-routed flights. Since the flight altitude was variable in this case of vertical re-routing, the NO_x emissions were subjected to different chemical regimes. Additionally, the emissions were also driven by the transport pathway, causing a larger difference in O_3 mixing ratios and hence, RF. The NO_x-O_3 effects were found to be stronger in the summer period than in winter, which also agrees with previous studies (e.g., [20, 74]). Although those findings in general might apply to other seasons, future studies could check if there are any special features due to various photochemical regimes for NO_x-O_3 effects.

For the RF calculation for an O_3 perturbation, a more advanced radiation flux change is required than instantaneous RF at the tropopause, because it is not a reliable predictor for expected resulting temperature change [49]. On the other hand, the simulation set-up employing pulse emissions is not well suited to derive stratospheric-adjusted RFs or effective RFs. To overcome this discrepancy, Grewe et al. [39] and Frömming et al. [33] applied a post-processing to their instantaneous RF values, converting them into stratospheric-adjusted RFs on the basis of a range of pre-calculated scenarios. However, a revision for this procedure might be necessary [42]. Therefore, here, the adjusted RF[1] calculation are consistently applied for the cost- and O_3 aCCFs- optimised air traffic, using the RAD submodel (Section 4.4.4).

In the present study, the flight optimisation in the European airspace was analysed but it might help extending the analysis to the North-Atlantic region where there is more freedom for routing to change: longer distances allowing detours and identifiable weather patterns [95]. Finally, Frömming et al. [33] took into account the influence of the weather on the total NO_x CCFs. This total effect includes not just the short term increase in O_3 but also a long-term decrease of CH_4 and a CH_4 induced decrease of O_3 (PMO and stratospheric water vapour decrease). In order to take this total effect into account for arbitrary situations using aCCFs, the current CH_4 aCCFs needs to be carefully evaluated [42]. Note also that there was a strong connection between the weather situation and O_3 CCFs as shown by Frömming et al. [33] but the O_3 aCCFs do not capture all features equally

[1] This value covers only a part of the stratospheric temperature adjustment, as a full adjustment could not be covered due to a simulation length of just four months.

well (Figures 4.5 and 4.6 (b)). Hence, while aCCFs in general are useful in calculating real-time flight trajectories for the sake of climate impact mitigation, looking at ways of improving them will lead to much needed improved predictions of climate impact from non-CO_2 effects of aviation, which are highly needed. As a result, climate-optimised flight planning could be practically feasible.

5

Estimating aviation's NO_x-O_3 warming effects with a probabilistic approach

Another world is not only possible, she is on her way.
On a quiet day, I can hear her breathing.

Arundhati Roy

Parts of this chapter are from Rao *et al.* [134], which is currently under peer review. Please cite as shown in the list of peer-reviewed journal articles, item 3.

5.1. Introduction

Chapter 4 discusses a detailed verification process which shows the effectiveness of O_3 aCCFs in optimising aircraft trajectories for reducing aviation NO_x induced climate impact resulting from O_3 formation. It was shown that while O_3 aCCFs provide reasonable mean estimates, they are limited to certain geographical areas (parts of the Northern hemisphere), are deterministic, and lack uncertainty estimates in their predictions. Without reliable uncertainty estimates, a surrogate model is ineffective for climate-optimised flight planning.

Here, probabilistic algorithmic climate change functions (paCCFs) are conceptualised as a replacement for aCCFs via a two-step approach: (i) firstly, by using the first comprehensive global dataset based on the CCF approach [33, 38, 135, 136], to recalculate iRF of O_3 induced by NO_x (i.e., O_3 iRF) in more regions (North America (N. America), South America (S. America), Eurasia, Africa and Australasia) and days for a range of cruise level altitudes thereby encouraging the possibility of *global* flight planning, and (ii) secondly, by formulating a corresponding high-accuracy *probabilistic* surrogate model using a chained Gaussian process (GP) regression model that is heteroscedastic to predict O_3 iRF with reliable uncertainty estimates using the most influential spatial and meteorological features locally. GP regression is a Bayesian nonparametric technique that exhibits great flexibility and captures more information about the data by using more parameters as the dataset grows. Moreover, predictions are made with confidence levels, using the most influential features obtained using feature selection techniques, which is especially desirable for non-CO_2 effects of aviation.

Compared to the aCCFs, more data are now available (Section 5.2) and the methodology is used to derive probabilistic algorithmic climate change functions (paCCFs) using standard (homoscedastic) and chained (heteroscedastic) GPs with additional features compared to van Manen & Grewe [42] is described in detail (Section 5.3). After visualising the data (Section 5.4.1), it is prepared (Section 5.4.2) to enable the training of the GP models to estimate climate impact in terms of O_3 iRF (Section 5.4.3). After assessing the performance of these models (Section 5.4.4), the use of this model is then demonstrated by applying the method exemplarily to actual flight routes in the European airspace (Section 5.4.5), enabling climate impact predictions including confidence levels. The manner in which the GP models maybe used for air traffic optimisation is discussed (Section 5.5) following which potential improvements are offered (Section 5.6).

5.2. Data generation

The simulations performed to obtain the complete dataset is described in Maruhashi *et al.* [136] (under review). The approach uses the EMAC model (Chapter 3) and several submodels and is briefly summarised here. Four submodels played a significant role for the investigation of short-term O_3 iRF from global aviation NO_x: TREXP (Tracer Release EXperiments from Point Sources, [44]), ATTILA (Atmospheric Tracer Transport In a LAgrangian model, [96]), AIRTRAC (Supplement of Grewe *et al.* [38]), and RAD [84]. TREXP was employed to define the positions and duration of release of NO_x pulse emissions in terms of latitude, longitude, and pressure altitude. The emission points are representative of aircraft flying at typical subsonic cruise levels (≈ 10 - 12 km) and consist of

28 emission points per region (N. America, S. America, Eurasia, Africa and Australasia), as shown in Figure 5.2a at an atmospheric pressure of 200, 250, and 300 hPa. An emission amount of 5×10^5 kg of nitrogen oxide (NO) was injected into the atmosphere at 06:00 UTC within a 15-minute time step and randomly split into 50 Lagrangian air parcel trajectories within the grid cell of each emission point using ATTILA. The procedure followed is the same as in [38] on the dates 1st January 2014 and 1st July 2014 each with a 3-month simulation period. Newtonian relaxation (i.e., nudging, [137]) was applied to variables such as vorticity, surface pressure field logarithm, wind divergence, and temperature within these simulations, nudging them towards 2014 ERA-Interim reanalysis data. Within each air parcel trajectory, the AIRTRAC submodel calculated the contribution of NO_x emissions to the atmospheric composition of O_3, CH_4, HNO_3, OH, and NO_y (active nitrogen species) and the background concentrations were computed by the MECCA submodel (Module Efficiently Calculating the Chemistry of the Atmosphere, [97]) for the troposphere and stratosphere. The impact of a NO_x perturbation on tropospheric O_3 change is characterised by chemical reactions as discussed in Chapter 2. The photolysis rate coefficients, chemical reactions simulating O_3 change and loss terms, and phenomena such as scavenging and dry deposition are taken into account using a host of submodels resulting in a net O_3 contribution. This is followed by the conversion of this contribution of a local emission to the global O_3 distribution from Lagrangian space to the EMAC grid point space for the calculation of the iRF of O_3 from aviation NO_x using the RAD submodel [84].

The RAD submodel computes the radiative fluxes every 2 hours, as opposed to 15 minutes, due to computational burdens, and the averaged value is extracted with a 6 hour output frequency over the 3-month simulation period. It is important to note that in this study, iRF refers to the mean global radiative impact resulting from a pulse emission, rather than the cumulative RF contributions since pre-industrial times and is measured relative to the climatological tropopause since the stratospheric-adjusted RF and the effective radiative forcing (ERF) are not feasible in this case [49, 80]. For computational efficiency and resolution balance, a T42L41 spectral resolution was selected for the EMAC grid, which includes 41 vertical hybrid pressure levels ranging from the surface up to 5 hPa and a horizontal grid space discretised into 128 longitude and 64 latitude points ($\approx 2.8° \times 2.8°$). A total of 30 simulations were conducted for five regions, two seasons and three pressure levels, totaling approximately 105,000 CPU hours using parallel computing on the Dutch supercomputer Snellius. Thus, CCM data generation is a computationally expensive process, and the goal is to adequately reproduce these predictions using the methodology described in Section 5.3.

5.3. Methodology

Supervised learning aims to find a relation between a target variable, $y \in \mathbb{R}$ (climate impact in terms of iRF from aviation NO_x emissions) and selected input variables that are influential, $\boldsymbol{x} \in \mathbb{R}^m$ (e.g., meteorological and spatial parameters), based on data generated from a high-cost CCM subject to several input climate model parameters. More concretely, there exists a dataset, $\mathcal{D} = \{(\boldsymbol{x}_i, y_i) | i = 1, \ldots, n\} \equiv (X, \boldsymbol{y})$ where $X \in \mathbb{R}^{n \times m}$ is called the design matrix and $\boldsymbol{y} \in \mathbb{R}^n$ is the target vector, created by aggregating the n cases. Given this dataset, it is desired to build a low-cost probabilistic surrogate model

that can make predictions for new, unobserved cases $\boldsymbol{y}_*$ using Gaussian process regression (GPR). This is a Bayesian nonparametric approach that does not yield a single best-fit point estimate, but provides a probability distribution for each estimate; they essentially provide a useful way of quantifying uncertainties in the model estimates for new test inputs. This runs contrary to deterministic surrogates such as the existing aCCFs [42], that provide a point estimate for a given input, that does not capture the uncertainty associated with it. This is discussed in detail in the following subsections.

5.3.1. Towards probabilistic algorithmic climate change functions

The fundamental issue lies in the computational burden borne by chemistry-climate models (CCMs), which can only be executed for a limited set of emission scenarios and cannot be run effectively in real-time. It is assumed that these CCM outputs serve as potentially noisy "ground-truth" data, and consequently, epistemic uncertainties within the CCM are not accounted for. The aim is to reproduce these climate impact forecasts by using information from influential variables at the emission source, i.e., locally. However, the variability in climate impact is not constant; it fluctuates across different geographic areas, over time, and under varying input conditions (Section 5.4.1). In statistical terms, this phenomenon is heteroscedastic. Conventional deterministic and most probabilistic surrogates disregard this phenomenon, providing an incomplete view of the climate response. In this section, a probabilistic framework is introduced which is designed to train homoscedastic and heteroscedastic surrogates using available data and make accurate climate impact predictions along with uncertainty estimates. Furthermore, the potential of employing this model for climate-optimised flight planning on a global scale in the context of climate-conscious decision-making is explored. The framework consists of five main steps as shown in Figure 5.1:

Step 1: Run the CCM to emit NO_x at specific points across the globe and trace the O_3 impact on a supercomputer which outputs a wide range of data including weather-related variables, chemical concentrations, and O_3 iRF. The latter is the quantity of interest or target variable, $y \in \mathbb{R}$, and described in Section 5.2. The process of running the CCM is computationally expensive and requires a wide range of input parameters (such as boundary conditions, emission inventories, weather data, initial conditions, chemical reaction rates of various atmospheric species, etc.) to accurately simulate complex phenomena in the atmosphere.

Step 2: Select weather and spatial parameters at the emission location from the global set. That is, the data is *local*. Next, perform objective feature selection by calculating the mutual information (MI) between the iRF and these local parameters and using Automatic Relevance Determination (ARD, [77]) to pick the m highest scoring features. This is described in Section 5.3.2. This feature set, $\boldsymbol{x} \in \mathbb{R}^m$, is used as a proxy of the most influential local features used as predictors for the Gaussian process models in step 3.

Step 3: Split the iRF data (d), into a training set (80%), y and a test set (20%), y_*. The former dataset is used to train probabilistic surrogate models based on a chained GP model [138] that is heteroscedastic, and a standard GP model [76] that is homoscedastic, using the features selected in step 2. This step is described in detail

in Section 5.3.3. The robustness of the choice of splitting the data is standard practice in statistical learning.

Step 4: Estimate the probability density function (pdf) of the test set from the CCM and the predictions made on it by the chained and standard GP model. Visually, the estimated pdfs of the two GP models, are always Gaussian, and can be compared to the data distribution (panel above "Radiative forcing" in Figure 5.1, discussed in Section 5.4.1. A number of metrics are then used to assess the performance of the prediction.

Step 5: This is a future suggestion, which entails the use of the chained GP model in predicting an improved estimate of iRF on an arbitrary day, where feature information is readily available. Then, the predictions of iRF can be converted to probabilistic algorithmic climate change functions (step 5a) for O_3 ($paCCF_{O_3}$), which represent the Average Temperature Response (ATR) of O_3 over a selected time horizon (e.g. 20 years) caused by a local aviation NO_x emission. This can then be used as an objective function in an air traffic optimisation tool (e.g., AirTraf [110]) to generate climate-optimised trajectories, that avoid the most climate-sensitive regions (step 5b), or converted into an equivalent CO_2 effect [139] to enable its use in the forthcoming EU-wide Monitoring, Reporting, and Verifying (MRV) scheme (step 5c).

5.3.2. Feature selection

After having generated the data (Step 1, Figure 5.1), feature selection serves as the second step. There are several potentially important features $\mathcal{V} \in \mathbb{R}^p$ that inform the climate impact of aviation NO_x on O_3, but statistical models are constrained by the curse of dimensionality for large p. However, a subset of important features $\mathcal{S} \subseteq \mathcal{V}$ can still be picked by: (i) calculating the mutual information (MI) between the target and each feature $\mathcal{I}(y; v_i)$ with $v_i \in \mathcal{V}$, $\forall i = 1, \ldots, p$ and selecting variables which are characterised by relatively large scores, and, (ii) using Automatic Relevance Determination (ARD, [77]), which automatically determines the relevance of different features for Gaussian process regression (GPR). Thus, $\mathcal{S} \in \mathbb{R}^m$ is obtained with $m < p$. Additionally it is informative to look at $\mathcal{I}(v_i; v_j)$ $\forall i \neq j$ to detect multicollinearity, which negatively impacts regression models. MI measures relationships between any two random variables, for which a moderate number of samples are available. Intuitively, it tells us how much can be learnt about one random variable by knowing the value of the other random variable. The MI between two univariate random variables X and Y is given by,

$$\mathcal{I}(X;Y) = \mathrm{KL}(\rho(x,y)||\rho(x)\rho(y)) = \int_{\mathcal{X}}\int_{\mathcal{Y}} \rho(x,y) \log \frac{\rho(x,y)}{\rho(x)\rho(y)} \mathrm{d}x\, \mathrm{d}y,$$

where $\mathrm{KL}(\rho(a)||\rho(b))$ represents the KL divergence between two probability density functions (pdfs), is ≥ 0 and it is a unit of statistical distance; $\rho(x,y)$ represents the joint pdf of X and Y over the space $\mathcal{X}, \mathcal{Y}$; and $\rho(x)$, $\rho(y)$ represent the marginal pdf of X and Y respectively.

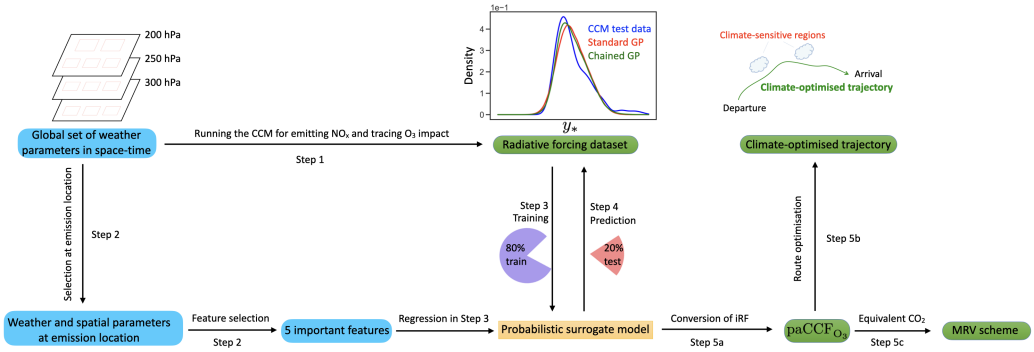

Figure 5.1: A schematic representation of the method to predict climate impact and its potential application in climate-optimised flight planning and use in a MRV scheme.

5

5.3.3. Standard and Chained GPR

In Section 2.2.1.3, the standard GPR was discussed, where the data is assumed to be *homoscedastic*, that is, the noise variance σ_n^2 is constant. This is a common assumption used in regression modelling for computational and technical convenience. This method is first applied for the current dataset to link local NO_x emissions to the RF from O_3 in Section 5.4. However, many real-world phenomena are characterised by heteroscedasticity; that is, the variance of the data is some (simple or complex) function of certain variables. Here, $\varepsilon \sim \mathcal{N}(0, \sigma_n^2(\boldsymbol{x}))$ is applied and the statistical model becomes,

$$y = f(\boldsymbol{x}) + \varepsilon(\boldsymbol{x}), \tag{5.1}$$

where y and $\boldsymbol{x}$ represent the iRF and the selected meteorological features, respectively. To solve this, the noise variance is modelled using a log-GP prior, to ensure that only positive values are possible. That is,

$$\rho(y|f(\boldsymbol{x}), g(\boldsymbol{x})) = \mathcal{N}\left(f(\boldsymbol{x}), e^{g(\boldsymbol{x})}\right), \quad \text{where,}$$
$$\rho(\boldsymbol{f}) = \mathcal{N}(\mu_f, k_f(\boldsymbol{x}, \boldsymbol{x'}))$$
$$\rho(\boldsymbol{g}) = \mathcal{N}(\mu_g, k_g(\boldsymbol{x}, \boldsymbol{x'}))$$

Thus, two GPs are used to learn both the mean and the variance of the Gaussian likelihood, and they are independent. However, note that in this case, the posterior distribution is not analytically tractable. There are several approximations used to address this issue such as Markov Chain Monte Carlo (MCMC, [140]), Laplace approximation [141], variational inference [142], and expectation propagation [143]. Here, the chained GPs by Saul *et al.* [138] is employed, which uses sparse variational inference to approximate GPs with the aid of so-called inducing point methods. These methods introduce $q < n$ pseudo points at locations $Z = \{\boldsymbol{z}_i\}_{i=1}^{q}$ to approximate the full covariance matrix. The locations are inferred by applying K-means clustering [144] to input data, $\boldsymbol{x}$ and using the cluster centres. The corresponding function values are $\boldsymbol{u}_f = f(Z)$ and $\boldsymbol{u}_g = g(Z)$. The posterior distribution to be determined is expressed using Bayes' theorem,

$$\rho(\boldsymbol{f},\boldsymbol{g},\boldsymbol{u}_f,\boldsymbol{u}_g|\boldsymbol{y}) = \frac{\rho(\boldsymbol{y}|\boldsymbol{f},\boldsymbol{g},\boldsymbol{u}_f,\boldsymbol{u}_g)\,\rho(\boldsymbol{f},\boldsymbol{g},\boldsymbol{u}_f,\boldsymbol{u}_g)}{\rho(\boldsymbol{y})},$$

where it is assumed that,

$$\rho(\boldsymbol{f},\boldsymbol{g},\boldsymbol{u}_f,\boldsymbol{u}_g|\boldsymbol{y}) \approx \rho(\boldsymbol{f}|\boldsymbol{u}_f)\rho(\boldsymbol{g}|\boldsymbol{u}_g)\rho(\boldsymbol{u}_f|\boldsymbol{y})\rho(\boldsymbol{u}_g|\boldsymbol{y}) \approx \rho(\boldsymbol{f}|\boldsymbol{u}_f)\rho(\boldsymbol{g}|\boldsymbol{u}_g)\pi(\boldsymbol{u}_f)\pi(\boldsymbol{u}_g), \quad (5.2)$$

where it has been assumed that the latent functions factorise for the tractability of the problem. In variational inference, proxies for $\rho(\boldsymbol{u}_f|\boldsymbol{y})$ and $\rho(\boldsymbol{u}_g|\boldsymbol{y})$ are obtained by seeking an appropriate distribution $\pi(\boldsymbol{u}_f)$ and $\pi(\boldsymbol{u}_g)$ respectively from a family of distributions $\mathcal{V}$, such that $\mathrm{KL}\big(\pi(\boldsymbol{f},\boldsymbol{g},\boldsymbol{u}_f,\boldsymbol{u}_g)||\rho(\boldsymbol{f},\boldsymbol{g},\boldsymbol{u}_f,\boldsymbol{u}_g|\boldsymbol{y})\big)$ is minimised. While the likelihood $\rho(\boldsymbol{y})$ is generally not tractable, a lower bound for $\log\rho(\boldsymbol{y})$ is found,

$$\begin{aligned}\log\rho(\boldsymbol{y}) &= \log\int \rho(\boldsymbol{y}|\boldsymbol{f},\boldsymbol{g})\rho(\boldsymbol{f}|\boldsymbol{u}_f)\rho(\boldsymbol{g}|\boldsymbol{u}_g)\rho(\boldsymbol{u}_f)\rho(\boldsymbol{u}_g)\mathrm{d}\boldsymbol{f}\,\mathrm{d}\boldsymbol{g}\,\mathrm{d}\boldsymbol{u}_f\,\mathrm{d}\boldsymbol{u}_g \\ &\geq \int \pi(\boldsymbol{f})\pi(\boldsymbol{g})\log\rho(\boldsymbol{y}|\boldsymbol{f},\boldsymbol{g})\,\mathrm{d}\boldsymbol{f}\,\mathrm{d}\boldsymbol{g} - \mathrm{KL}(\pi(\boldsymbol{u}_f)||\rho(\boldsymbol{u}_f)) - \mathrm{KL}(\pi(\boldsymbol{u}_g)||\rho(\boldsymbol{u}_g)). \quad (5.3)\end{aligned}$$

Following Saul *et al.* [138] and modelling $\pi(\boldsymbol{u}_f) = \mathcal{N}(\boldsymbol{u}_f|\boldsymbol{m}_f,\Sigma_f)$ and $\pi(\boldsymbol{u}_g) = \mathcal{N}(\boldsymbol{u}_g|\boldsymbol{m}_g,\Sigma_g)$ allows us to compute $\pi(\boldsymbol{f}) = \int\rho(\boldsymbol{f}|\boldsymbol{u}_f)\pi(\boldsymbol{u}_f)\mathrm{d}\boldsymbol{u}_f$ and $\pi(\boldsymbol{g}) = \int\rho(\boldsymbol{g}|\boldsymbol{u}_g)\pi(\boldsymbol{u}_g)\mathrm{d}\boldsymbol{u}_g$. The likelihood also factorises, i.e., $\rho(\boldsymbol{y}|\boldsymbol{f},\boldsymbol{g}) = \prod_{i=1}^{n}\rho(y_i|f_i,g_i)$, allowing us to apply stochastic variational inference to the integral in Eq. (5.3),

$$\log\rho(\boldsymbol{y}) \geq \sum_{i=1}^{n}\int \pi(f_i)\pi(g_i)\log\rho(y_i|f_i,g_i)\,\mathrm{d}f_i\,\mathrm{d}g_i - \mathrm{KL}(\pi(\boldsymbol{u}_f)||\rho(\boldsymbol{u}_f)) - \mathrm{KL}(\pi(\boldsymbol{u}_g)||\rho(\boldsymbol{u}_g)).$$

The above integral can be solved analytically since the likelihood is Gaussian. Note that the variational parameters $\boldsymbol{m}_f,\Sigma_f,\boldsymbol{m}_g,\Sigma_g$ are learnt through maximising the bound. After optimisation, the posterior predictive distribution is calculated as,

$$\rho(y_{i*}|y_i,\boldsymbol{x}_i,\boldsymbol{x}_{i*}) = \int \rho(y_{i*}|f_{i*},g_{i*})\pi(f_{i*})\pi(g_{i*})\,\mathrm{d}f_{i*}\mathrm{d}g_{i*}, \quad (5.4)$$

where each prediction point is treated independently for the data pair $\{(\boldsymbol{x}_{i*},y_{i*})\}_{i=1}^{n_*}$. While inferring GPs (without a sparse approximation) have a computational cost of $\mathcal{O}\left(n^3\right)$, chained GPs with a sparse approximation have a computational cost of $\mathcal{O}\left(nq^2\right)$ for q inducing points that are used to parameterise the covariance matrix. The inducing points are picked as a subset of the training data X, thus $q < n$, which makes it more computationally efficient than standard GPs, especially while dealing with large datasets. Additionally, chained GPs permit a nonlinear combination of any number of GPs even with models with a non-Gaussian likelihood. The chained GP methodology is implemented using a machine learning library called GPFlow (version 2.6.3, [145]).

5.4. Results

5.4.1. Data on the relation of local NO_x emissions to O_3 iRF

The CCM data (Section 5.2) corresponding to the short-term O_3 iRF from local aviation NO_x emissions is visualised for each pressure level and all emission scenarios in Figure 5.2b. Since there is no clear pattern and there is significant variation in the data, it is informative to detect statistical outliers. The outliers are those data points that are larger than the Interquartile Range (IQR) ($> Q_3 + 1.5 \times \text{IQR}$) or smaller than the IQR ($< Q_1 - 1.5 \times \text{IQR}$), where Q_1 and Q_3 represent the first and third quartiles, respectively. Figure 5.2b also depicts a boxplot with the fifteen outliers, all of which deviate from the first and third quartile by more than 1.5 times the IQR. These outliers are associated with the pressure levels of 200 and 300 hPa, and are mostly associated with Australasia. These elevated iRF values, especially in Australasia, are explained by the increased efficiency of O_3 production for a given quantity of NO_x. This is due to the heightened sensitivity of a NO_x-deficient atmosphere [20, 21, 31, 135]. On the other hand, the lowest mean climate impact from NO_x corresponds to 250 hPa, and is consistent with Frömming *et al.* [33]. Figure 5.2c depicts the evolution of NO_x and O_3 over the simulation period starting from 1st January 2014, for two release locations. The solid line represents the outlier associated with grid index '2' of Australasia at 200 hPa and the dashed line represents grid index '4' of N.America at 250 hPa. Although the NO_x is consumed faster for the point associated with the outlier, the peak O_3 mass and the area under the curve are significantly larger, indicating a greater O_3 production, and a larger iRF as a result. Apart from the magnitude of the peak O_3 mass, its position shows that it also occurs much sooner. Thus, it can be seen from the data that the relation between NO_x emissions and O_3 forcings is not straightforward, making a reliable surrogate model for predicting NO_x-O_3 impact even more essential.

5.4.2. Data preparation and feature selection for GPR

The CCM data for iRF is represented on the time region grid (trg), whereas the features are represented on the EMAC grid. Owing to the different grid resolutions, the features from the finer EMAC grid are bilinearly interpolated to the coarser time region grid [42]. That is, $x_i : \text{EMAC} \rightarrow \text{trg}, i = 1, \ldots, p$. Subsequently, following Section 5.3.2, the MI between iRF and interpolated features is calculated by first estimating their true pdf using Kernel Density Estimates (KDEs) with the help of Scott's rule for bandwidth selection [146]. From the list of features considered (Appendix C), ten highest scoring features that can be used to predict the target variable. These include temperature, geopotential, zonal wind velocity, meridional wind velocity, vertical wind velocity, specific humidity, relative humidity, potential vorticity, solar irradiance, and release location of the emissions in terms of latitude. However, the choice is restricted to five features, due to the curse of dimensionality. High dimensional feature spaces are sparsely populated with data, making it harder to predict patterns. For instance, an m-dimensional feature space contains 2^m corners, thus using five features requires much lesser data than (say) ten features. To narrow down feature selection with the help of ARD, the target and features are first transformed to a common scale using Z-score normalisation,

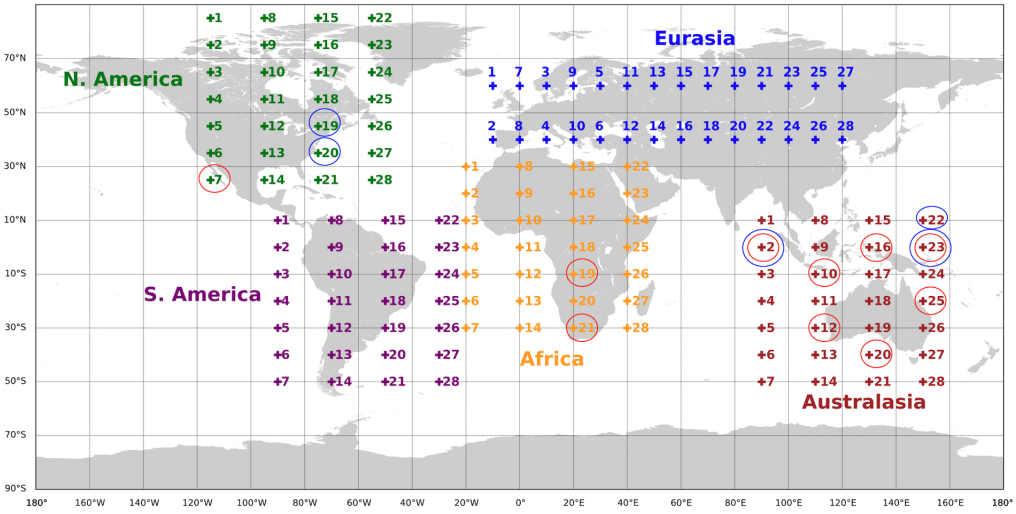

(a)

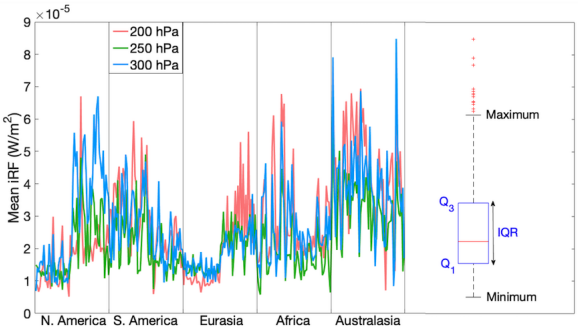

(b)

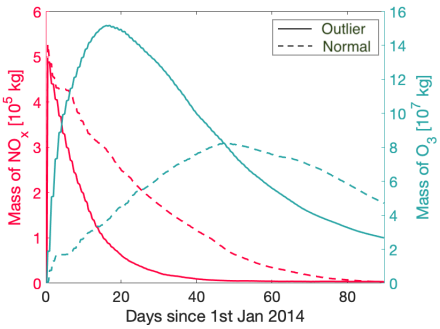

(c)

Figure 5.2: The emission locations and corresponding iRF [W/m^2] dataset from the CCM simulations for the three cruise pressure levels. **(a)** The time region grid comprising 28 emission locations for each of N. America, S. America, Eurasia, Africa and Australasia, for which the iRF is calculated (used from [135]). The red and blue circles represent regions associated with statistical outliers in the iRF dataset corresponding to 200 and 300 hPa, respectively. No outliers are present for 250 hPa. **(b)** The iRF values, where the horizontal axis represents the corresponding geographical regions per pressure level where emissions were released. The boxplot of the same data is shown, where the red horizontal line represents the median and the fifteen outliers are marked with red crosses. The minimum, maximum, first and third quantiles (Q_1, Q_3), and Inter Quantile Range (IQR) are labelled in the plot. **(c)** The evolution of NO_x-O_3 mass for two time region grids over the 3-month simulation period since 1st January 2014. The solid line represents the outlier associated with time region grid index '2' of Australasia at 200 hPa and the dashed line represents time region grid index '4' of N.America at 250 hPa. The peak O_3 mass and the area under the curve is significantly larger for the outlier, ultimately resulting in a larger iRF.

$$\frac{A-\mu_A}{\sigma_A}$$

where A, μ_A, and σ_A represent any variable to be normalised, their sample mean, and sample standard deviation, respectively. Applying the normalisation causes the associated feature or target to have zero-mean and unit-variance. After initially using all ten normalised features in the GP models, ARD suggested the following five features as the most influential: Temperature (T), geopotential (ϕ), solar irradiance (S_r), zonal wind velocity (u_w), and, release location of the emissions in terms of latitude (R_lat). It is known that solar irradiance provides the energy needed for photochemical reactions for NO_x in the atmosphere, leading to the formation of O_3. The corresponding increase in T due to increase in solar irradiance also influences these reactions [147], while R_lat, ϕ, and u_w, govern the location and subsequent pathways for NO_x emissions. However, it is well known the largest O_3 change occurs after about ten days since the release of emissions [74]. Now, the normalised dataset is randomly shuffled and split into 80% training data $\mathcal{D}$ which will be used to train the GP models and 20% test data $\mathcal{D}_* = (X_*, \boldsymbol{y}_*)$ upon which the trained models will make predictions (Section 5.4.3). This is done so that overfitting can be avoided, and is standard machine learning practice.

5

5.4.3. Estimating climate impact

After randomly selecting 80% of the dataset in training (y) the GP models, their climate impact estimates on the remaining 20% test data (y_*) are visualised in the form of pdfs (panel above 'radiative forcing dataset' in Figure 5.1). They bear a close resemblance and exhibit a considerable overlap with the data distribution. However, the position and magnitude of the peak of the chained GP pdf aligns more closely with that of the CCM pdf compared to the standard GP model. The splitting of the data is done to prevent overfitting, and thus provide models that can be generalised. The two characteristic aspects of GP models are the mean and variance estimates. Figure 5.3a shows the mean predictions from the chained GP model against the test data. It can be seen that the six largest values of iRF test data are underestimated (enclosed by the magenta box) by the mean of the GP model, and are part of the set of outliers shown in Figure 5.2b. Since the feature space is high-dimensional ($\mathbb{R}^5$) and thus difficult to visualise, we plot test data and predictions against one of the features (i.e., temperature) in Figure 5.3b. Here, predictions are shown for 20 chosen test indices so as to avoid clutter. The left and right panel of Figure 5.3b represents the mean and variance predictions from the standard GP and chained GP models, respectively. The mean predictions of the standard and chained GP models are depicted as blue and black points, respectively and the test data points are shown in orange. The variance predicted for each test index by the standard GP model and chained GP model is colour-coded with respect to its magnitude shown in the colour bars. For the standard GP, the variances (uncertainty estimate) are almost the same for changes in temperature and while most data are captured, many outliers are not. On the other hand, for the chained GP, the variance changes, as it is a function of the feature space and captures most almost every single data point. A smaller (larger) variance corresponds to a higher (lower) confidence in predicting the target. It is seen though, that while the mean prediction is similar to the standard GP model, the

variance in some cases is smaller (larger) and it captures these test data points with relatively higher (lower) probability. For example, the prediction at 210 K is associated with low uncertainty, while 220 K is associated with a relatively large uncertainty. Similarly, violin plots for predictions against the other features are available in **??**. The predictions corresponding to outliers are characterised by large variances. Thus, the climate impact is estimated with varying confidence levels, making the chained GP model more realistic. Going further, we score each of the five features based on the test dataset, by computing their corresponding MI with iRF. We then normalise these scores by dividing them by the highest score and deduce that solar irradiance (S_r) and zonal wind velocity (u_w) are the most and least important predictors of aviation NOx-O3 effects, respectively (Figure 5.3c).

5.4.4. Performance of the model and comparisons

Here, the performance of the GP models is evaluated and compared to an existing linear regression model by following the R^2 test for the mean predictions on the test data. Additionally, the statistical distance between the predictive distribution of the GP models and the test data distribution is measured using the Kullbak-Leibler (KL) divergence [148].

Keeping the test data fixed, the amount of data used for training the models are varied: 100%, 80%, 60%, and 40% of y, which serves as a simple convergence study (Figure 5.4). The R^2 increases as the amount of training data is increased, as shown in Figure 5.4a. The R^2 is only marginally higher for the standard GP model (= 0.53) than the chained GP model (= 0.51) when all the training data is used (scenario in Figure 5.3) and this can be attributed to the latter requiring more data to learn both, the mean and variance functions (Section 5.3.3). Hence, both models show basically the same quality in this respect. Since KL divergence measures statistical distance between the distributions, the value should fall as more training data is used by the GP models. All fifteen statistical outliers were removed from the full dataset (Figure 5.2b), since this measure is sensitive to them. For both GP models, there is a reduction in KL divergence as the amount of training data increases (Figure 5.4b). The sharper changes for the chained model (especially moving from 40% to 60% y), can be attributed to the requirement of learning two latent functions (and hence more hyperparameters) at the same time, which requires more data. The global minimum in KL-divergence is lower for the chained GP model, which indicates a higher accuracy compared to the standard GP model.

So how do these surrogate models perform compared to a linear regression model? The best available model derived by van Manen & Grewe [42], which involves using T, ϕ, and $T \cdot \phi$ as features is used. The third feature, which is the product of T and ϕ was used to model the non-linearity of NO_x-O_3 effects. After training a linear regression model with these features for the data, the mean predictions are visualised and the predictions from the standard GP model are also overlaid as a reference in Figure 5.4c. Visually, it is clear that the linear model cannot reproduce the data and quantitatively, the R^2 value of 0.05 is too low, thus confirming that the linear regression model does not fit the data well. The higher R^2 that was obtained by van Manen & Grewe [42] for O_3 aCCFs can be attributed to two reasons. Firstly, the data was only based on the North Atlantic region,

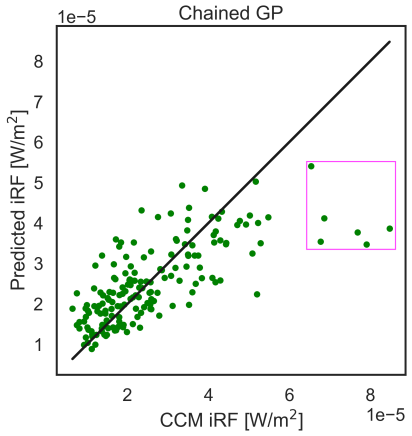

(a)

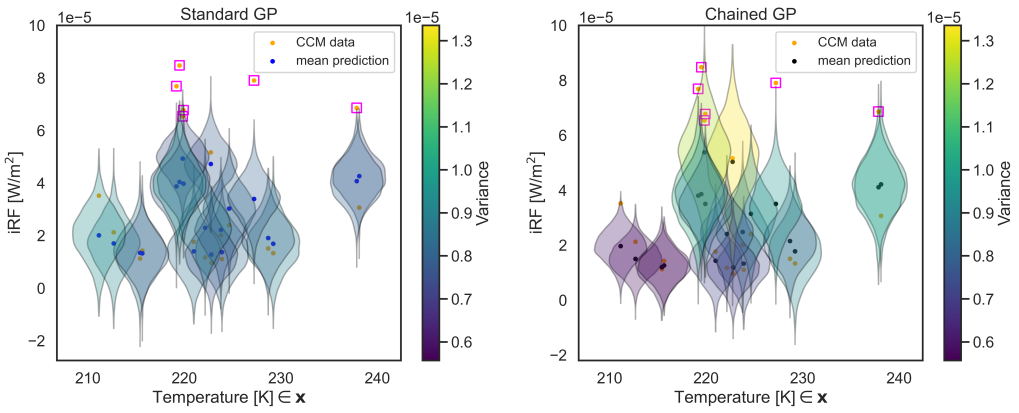

(b)

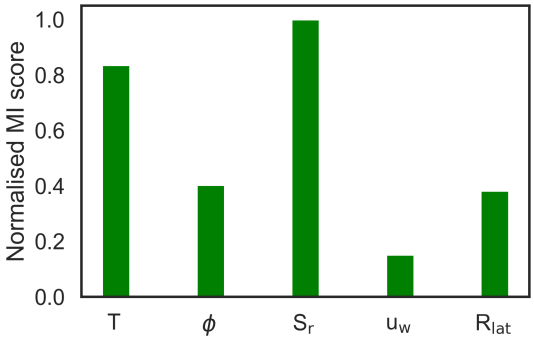

(c)

Figure 5.3: Comparing predictions from the GP models and the test data. **(a)** Mean predictions from the chained GP model in green plotted against the CCM test data on the horizontal axis. **(b)** Violin plot of the predictions from the two GP models, plotted against one of the features (temperature), for 20 chosen test indices. **(c)** Bar chart containing normalised MI scores between each feature and iRF of the test dataset.

and secondly, all the data were used for training the model unlike this case.

5.4.5. Climate impact estimation for a frequently flown flight

The chained GP model is applied to forecast the NO_x-O_3 climate effects of a commonly operated flight within the European Union, considering various departure times on a selected day. This analysis is based on actual flight path data retrieved from the Eurocontrol database [111], and the details of these flights are provided in Table 5.1. In addition to this, the great circle flight path which represents the shortest path is included for the same origin-destination pair at a typical cruise altitude of 10.7 km to highlight differences in predictions. The weather-related feature data (T, ϕ, S_r, u_w) are obtained from the CCM corresponding to the departure time of the flights to enable the evaluation of the chained GP model.

Figure 5.5b shows the three actual flight paths and the great circle path from take-off from the departure airport in the Netherlands (Amsterdam Schiphol (EHAM)) to the landing in the arrival airport in Spain (Madrid-Barajas airport (LEMD)), while Figure 5.5a shows the climate impact prediction from the chained GP model during the cruise phase of the flights. In the latter, it can be seen that among the three actual flight paths, the largest and smallest peak mean impacts occur for the flight departing at 18:49 UTC and 09:25 UTC, respectively, at 45°N (Figure 5.5a). Conversely, the largest and smallest uncertainty estimates occur for the flights departing at 09:25 UTC and 18:49 UTC, respectively. Figure 5.5b also shows a colour map of the wind velocity field embedded with geopotential height contour lines at a cruise level of 216 hPa at an arbitrary time of the day on which the flights take place. The orange diamond in the figure represents the region where maximum mean climate impact was predicted for the three flights. Emissions here are expected to be transported to lower latitudes by the jet stream and this region has been identified earlier with a large and early O_3 maximum compared to higher latitudes characterised by a small and late O_3 maximum [74]. Looking at the variation of uncertainty estimates throughout cruise flight, it is found to be lowest for the flight at 09:25 UTC, and highest for the flight at 18:49 UTC. The total climate impact for the cruise level, however, is largest for the flight at 09:25 UTC and smallest for the flight at 10:20 UTC. The difference in prediction between the great circle path and the three actual flight paths is significant, indicating that the GP model is indeed influenced by the chosen features, and not dominated by noise. The varying confidence intervals, subject to varying input conditions, shows that if one were to optimise flights based on climate impact using a heteroscedastic model (Figure 5.1), the expected reduction in climate impact can be associated with a level of probability.

Table 5.1: Characteristics of three flights from EHAM to LEMD on 1st June 2016 at different departure times.

Flight	Departure time (UTC)	Arrival time (UTC)	Flight duration [hours]
1	09:25	11:49	2.4
2	10:20	12:49	2.5
3	18:49	20:56	2.1

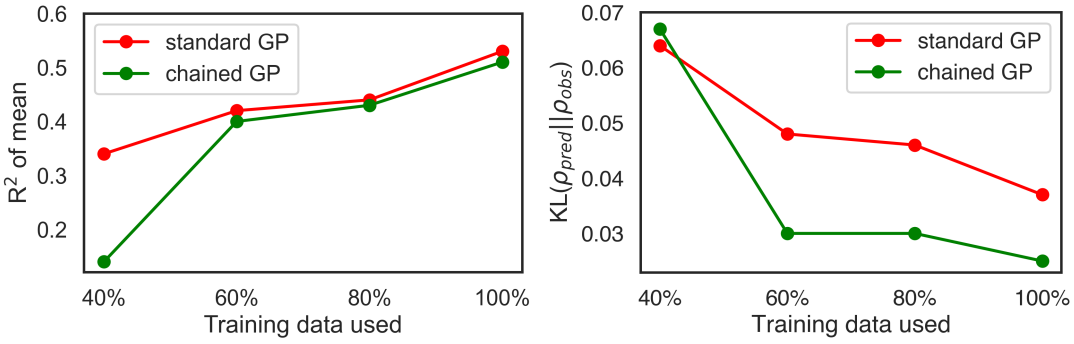

(a) (b)

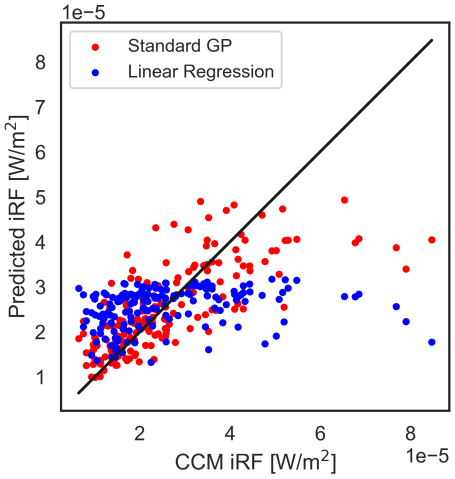

(c)

Figure 5.4: Convergence study of GP models and comparison with linear regression models. The complete dataset (d) is split into training data (y), which never exceeds 80% d, and test data (y_*) is fixed at 20% d. It is analysed if the GP models perform better by gradually increasing the amount of training data for four scenarios: 40%, 60%, 80%, and 100% of y and testing them on y_*. **(a)** Convergence of R^2 of the mean predictions on the test data increases as more training data is used. **(b)** The statistical distance between the predictive distribution and the test data distribution shrinks in terms of KL divergence as more training data is used. **(c)** The mean predictions of the linear regression model (in blue) are compared against test data with $(T, \phi, T \cdot \phi)$ as the feature basis. The mean predictions from the standard GP model (in red) are overlaid as a reference.

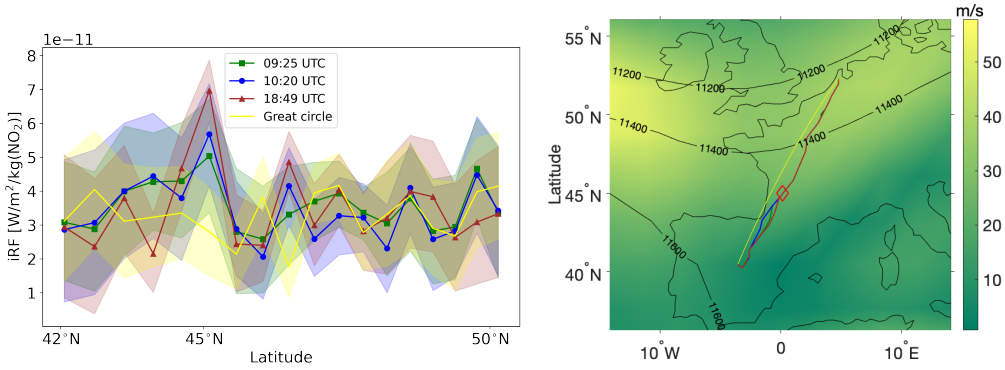

(a) (b)

Figure 5.5: Characteristics of the three flights described in Table 5.1 and the great circle path. **(a)** The climate impact prediction from the chained GP model for the three actual flights and the great circle path at cruise level in terms of scaled O_3 iRF [W/m^2/kg(NO_2)]. The horizontal axis represents the latitude. The solid lines and the shaded areas represent the mean prediction and 95% confidence interval, respectively, for all four paths. The markers for the three actual flights denote specific points along the trajectory at cruise level, at which the model is evaluated. At 45° N, these three flights show a peak mean climate impact. **(b)** The actual reported flight paths shown in 2D for the three flights, including take-off and landing retrieved from the EUROCONTROL database [111] and the 2D great circle path. The colour map and contour lines represent the wind velocity [m/s] and geopotential height [m], respectively, at a cruise atmospheric pressure of 216 hPa while the orange diamond represents the region where maximum mean climate impact is predicted for the three flights.

5.5. Towards climate-optimised flight planning

Now that it has been shown that the probabilistic surrogate models perform reasonably well in reproducing results (Sections 5.4.3 and 5.4.4) from the verified EMAC model (see Section 3.2), and can be used to estimate the climate impact of existing flights (Section 5.4.5), it can also be used in generating climate-optimised flight trajectories with respect to NO_x-O_3 effects, which requires weather and spatial data, that are readily available and avoids high-cost CCM simulations. Earlier studies for climate-optimised flight planning used either CCFs [39] or the deterministic aCCFs [80, 132, 149, 150] as the objective function to generate climate-optimised flights with a significant mitigation potential. In order to use the new probabilistic surrogate model, the mean function of the posterior predictive distribution (Eq. (2.17)) of either the standard or chained GP model can be used. It is re-written here as,

$$\tilde{\mu}(\boldsymbol{x}_*) = \mu(\boldsymbol{x}_*) + \sum_{i=1}^{n} \alpha_i k(\boldsymbol{x}_i, \boldsymbol{x}_*), \tag{5.5}$$

where $\boldsymbol{\alpha} = K_y^{-1}\big(\boldsymbol{y} - \mu(X)\big)$ and the other terms can be referred to in Section 2.2.1.3. Thus, it involves the linear combination of n kernel functions, each of which is centred on a training point and represents the mean predicted iRF as a function of the selected features: T, ϕ, S_r, u_w, and R_{lat}. Since it is of interest to assess short-term climate impact of this re-routing strategy and policy decisions, it is beneficial to convert the predicted iRF for pulse emissions to average temperature response over a time horizon of 20 years for

non-pulse emissions [14]. An example of non-pulse emissions is an increased emission scenario representing the growth of air traffic, where such a conversion is desirable [12]. The suitable climate metric is called F-ATR20 (Future emission-scenario based Average Temperature Response over a 20-year horizon),

$$\text{F-ATR}H = \frac{1}{H}\int_{t_0}^{t_0+H} \Delta T(t)\mathrm{d}t,$$

where H = 20 years, t_0 represents the initial time period, and, $\Delta T = \lambda \times \text{aRF}$, represents the time-varying global-mean temperature change for climate sensitivity parameter (λ). However, calculating F-ATR20, requires a preliminary conversion of iRF to stratospheric-adjusted RF (aRF), which cannot be calculated directly, and requires a parameterisation. The parameterisation followed by Grewe *et al.* [38] requires additional simulations for various times of the year and perturbation altitudes for the new regions considered here (Figure 5.2a) and is beyond the scope of this study. Subsequently, the efficacy of individual forcing agents (in this case, O_3) in producing global temperature change can be calculated [52, 151]. The final conversion to F-ATR20 (per kilogram of emitted NO) of O_3 from the mean predicted iRF will be called ozone probabilistic algorithmic climate change function (paCCF_{O_3}). The paCCF_{O_3} can then be be used as the objective function in AirTraf (see Chapter 3), to generate climate-optimised flight trajectories. This is illustrated in Figure 5.1.

If the methodology based on Section 5.3 is extended to other climate forcing agents, the complete paCCF can be written as the piece-wise sum of individual contributions from each agent c,

$$\text{paCCF} = \sum_c \text{paCCF}_c\,,$$

where $c \in \{O_3, CH_4, H_2O, \text{contrails}, \text{aerosols}\}$, and paCCF can be used as an objective function in AirTraf.

5.6. Discussion

The application of climate-optimised routing requires us to be able to predict the climate impact of various forcing agents (here, NO_x emissions) as a function of readily available forecasts of relevant features. It is shown that probabilistic surrogate modelling is useful in providing uncertainty estimates to climate impact from aviation NO_x in terms of iRF. Both, the chained (heteroscedastic) and the standard GP model (homoscedastic) perform well and significantly better than the deterministic aCCFs [42]. The chained GP model reproduces the data distribution more accurately than the standard GP model, and has the added advantage of providing varying confidence levels for their predictions on test data. Additionally, the model is global and it was found that, apart from temperature and geopotential at the point of release, the solar irradiance, zonal wind velocity and release location are significant predictors of warming produced from O_3 as a result of aviation NO_x. Furthermore, it was observed that the uncertainty estimates due to varying input conditions is significant (Figure 5.3b and Appendix D). The improvements are demonstrated by applying the method exemplarily to actual flight routes in the European airspace, enabling climate impact predictions including confidence levels. Thanks

to this nonparametric approach, incorporating more iRF data into the model's training process could potentially reveal a reduction in uncertainty estimates, ultimately leading to a decreased risk in climate-optimised flight planning.

However, a model can be only as good as the quantity and quality of the data used to train it. Firstly, data are available for aviation NO_x emissions released on 2 days (and for three pressure levels), which constitutes $n = 840$ data points. Standard GP models, without a sparse approximation of the covariance matrix, has $\mathcal{O}(n^3)$ complexity is limited by $n < 10000$, or ≈ 24 days. Thus, while there are computational limitations to calculate the data, running the full order model with the simulation setup of Maruhashi *et al.* [135] for a few more days and regions (e.g., remaining parts of Asia), characterised by other seasons and cyclical events such as El Niño and La Niña could help further advance the understanding of local aviation NO_x emissions on global warming. Secondly, there are certain physical limitations in the NO_x-O_3 chemistry calculated by the EMAC submodel AIRTRAC [38], which is part of the CCM data generation process (Section 5.2). While these limitations include the use of linearised reaction rates and fewer tagged processes, simple and accurate correction factors were derived by Maruhashi *et al.* [136] considering various emission scenarios. These values can be used appropriately to scale the iRF data used by the GP models. Thirdly, in order to convert iRF to CCFs, for the regions considered in this paper, the parameterisation must be revised with the aid of additional simulations, which will further improve this work. Lastly, this is both, an atmospheric transport and chemistry problem [33, 74] that requires to addressed while relying on a limited amount of CCM data. Since atmospheric transport is dominated by advection and convection (rather than diffusion) due to the dynamic movement of air masses driven by various factors such as temperature gradients, pressure differences, and wind patterns, using *local* weather data as features may not capture all the relevant physics of the problem. This is the largest source of uncertainty in the aCCFs and GP models as the iRF is predicted solely based on weather data at the release site, overlooking the broader weather pattern's influence. This could partly explain why some statistical outliers are underestimated with respect to the *mean* of the surrogate models. The use of nonlocal data, in terms of trajectory forecasts, for a better understanding of NO_x-O_3 chemistry has also been suggested [74], which can be leveraged in the future.

While nonlocal data is readily available from the underlying chemistry-climate model, there are two challenges: choosing how to define a nonlocal region in space, and the computational issue of dealing with its high-dimensional nature. To make this tractable it is required to represent the nonlocal data in a lower-dimensional space. A linear dimensional reduction method such as Principal Component Analysis (PCA) or multidimensional scaling (MDS) could be attempted, or nonlinear reduction if it proves necessary, e.g. kernel-PCA, Isomap [152], or auto-encoder approaches [153]. Assuming the model can be successfully calibrated, it will provide specific information about the importance of local versus nonlocal effects, as well as the underlying noise level. It *may* be able to incorporate nonlocal effects to improve prediction, but given the convective nature of the underlying process this is perhaps unlikely. If these dimension-reduction methods do not show a low-*effective* dimension, then a method capable of native high-dimensions such as neural networks (NN) would be required. They can be used in regression as replacements for any other surrogate. In the context of physical predic-

tions however, experience shows it is necessary to incorporate physical constraints [154]. The use of nonlocal data as features can also help reducing the variance of the predictions (Figure 5.3b and Appendix D), which could be beneficial in increasing the climate-impact mitigation potential for flight planning. Nevertheless, uncertainties will remain. While this new model is a big step forward in advancing the predictive ability of NO_x-O_3 effects and climate-optimised flight planning, further strides can be made by implementing the methods mentioned in this section to other effects of aviation NO_x and climate forcing agents such as H_2O, contrails, and aerosols.

In order to apply the paCCFs in a non-CO_2 MRV scheme, one would require real-time trajectory data and local atmospheric conditions, which are both available to aircraft operators. Using this information, the chained GP model can provide climate impact estimates of the released NO_x, along with the associated likelihood. The total climate impact from NO_x for each flight, associated with a level of probability, can then be converted to metric tonnes of equivalent CO_2 (t CO_2 eq). The recorded t CO_2 eq, accompanied typically with a 95% confidence interval, aligns with the methodologies and metrics evaluated by the Intergovernmental Panel on Climate Change (IPCC) and endorsed by the Conference of the Parties, acting as the meeting of the Parties to the Paris Agreement. This way, the probabilistic approach used in this work ensures accurate monitoring of climate impact of aviation NO_x and will be beneficial for inclusion in the forthcoming EU-wide MRV initiative, targeting non-CO_2 aviation impacts.

6

Conclusions and outlook

The basic contradiction of the capitalist system of control is that it cannot separate 'advance' from destruction, nor 'progress' from waste – however catastrophic the results. The more it unlocks the powers of productivity, the more it must unleash the powers of destruction; and the more it extends the volume of production, the more it must bury everything under mountains of suffocating waste.

István Mészáros

6.1. Conclusions

The goal of this dissertation, as defined in Chapter 1 is to verify and improve the estimation of localised aviation NO_x emissions on RF via changes in the greenhouse gas O_3 by using uncertainty quantification techniques. The main research question and its sub-questions are revisited here to assess the extent to which they have been answered:

How effective is the prediction of aviation's climate impact in real-time to enable climate-optimised flight planning?

The prediction of aviation's climate impact, particularly the non-CO_2 effects, are strongly dependent on the spatio-temporal location, and thus the prevailing weather situation. Good estimates are desirable, given that non-CO_2 effects contribute to probably two-thirds of the total impact from aviation, and are simultaneously characterised by a low level of scientific understanding. The aCCFs serve as a deterministic surrogate model that estimate the climate impact of a local aviation emission using data from weather forecasts. Thus, real-time prediction of aviation's climate impact is possible. To test the aCCFs in a climate modelling framework, they were programmed as the ACCF submodel in the MESSy framework, with EMAC as the base model. In order to generate climate-optimised trajectories, the aCCFs are used as an objective function by coupling the ACCF submodel with the air traffic simulator submodel AirTraf. The effectiveness of the aCCFs and the optimisation approach are addressed in the first sub-question.

Are algorithmic climate change functions (aCCFs) a reliable tool for predicting and abating aviation's climate impact?

It should be noted that the quality of aCCFs, as expressed in terms of adjusted R^2, is not that high for NO_x-O_3 and NO_x-CH_4 effects, and unreported for contrail effects. In Chapter 3, the ACCF submodel, which embodies the aCCFs in accordance to MESSY coding standards, along with the required adaptation within EMAC were discussed. Here, the impact of using different sources of meteorological data were analysed with respect to predictions made by contrail aCCFs. It was shown that the modelled non-linear dependence between the contrail impact prediction and temperature, makes these aCCFs very sensitive to changes in temperature. To alleviate this, a simple correction term for temperature was determined and applied within the EMAC model which indicated a decrease in potential contrail coverage (PCC) and a lower climate impact prediction. However, there are major sources of uncertainties pertaining to meteorological inputs and contrail physics that are abstracted from the problem and these were discussed. It was concluded that while the aCCFs are a novel conceptualisation for predicting the climate impact of local cruise aviation emissions, a strict verification process is desirable. Thus, in Chapter 4, a novel approach was applied to assesses the effectiveness of reducing the aviation-induced impact via ozone (O_3) formation from NO_x emissions by using O_3 aCCFs for aircraft trajectory optimisation. For the first time, the effectiveness of a climate-optimised strategy with the EMAC model and several other submodels was explored in two distinct ways: allowing lateral movements for a fixed cruise altitude, and, allowing vertical movements but restricting lateral changes. Summer and winter days with significant O_3 aCCF spatial variability were chosen for a one-day air traffic simulation in European airspace. This was done to test the O_3 aCCFs under extreme situations characterised by contrasting seasons and synoptic situations. The different predictions by O_3 aCCFs for these days created differences in re-routing results, especially in the

vertical direction. In both cases, climate-optimised flights yielded lower O_3 radiative forcing (RF) than cost-optimised flights. Lateral re-routing for the fixed cruise altitude corresponding to 250 hPa resulted in a lower climate impact than vertical re-routing. However, the mitigation potential was found to be greater for vertically re-routed flights. Three findings were found to be in agreement with several other studies. Firstly, the impact of the weather situation on the selected winter and summer day and subsequent transport pathways proved to be very crucial in the climate impact of flights. Secondly, NO_x-O_3 effects were found to be stronger in the summer and thirdly, vertically re-routed flights were at lower flight altitudes compared to cost-optimised flights. However, while the use of O_3 aCCFs in flight planning allows the climate impact mitigation in terms of RF, discrepancies in predicting O_3 impact from aviation NO_x emissions, especially on the chosen summer day, motivated the need for further research to refine the O_3 aCCFs concept. It was discussed in Chapter 4 that a step in this direction could improve predictions of non-CO_2 aviation effects which in turn facilitate global climate-optimised flight planning. This leads to the second sub-question which is addressed below.

What kind of uncertainty quantification (UQ) techniques are conducive to improving this predictive power?

In Chapter 2, UQ was introduced for its relevance in improving climate model projections. Here, probabilistic surrogate modelling was discussed as a means of accurately estimating climate impact in a computationally feasible manner. As stated above, the rationale behind replacing them with a more accurate global surrogate model that also yields confidence intervals was discussed in Chapter 5. This was achieved by: (i) using a global comprehensive dataset on aviation NO_x-O_3 effects in five geographical regions and multiple pressure levels generated from EMAC model simulations, (ii) following an objective approach to selecting atmospheric variables (feature selection) that influence NO_x-O_3 impact, and, (iii) regressing the data against selected atmospheric variables using a stochastic surrogate model based on homoscedastic (standard) and heteroscedastic (chained) Gaussian process regression. It was deduced that temperature, geopotential, solar irradiance, wind velocity and the release location are all important predictors of NO_x-O_3 effects. Thus, with this independent approach applied to a global dataset, features in addition to van Manen & Grewe [42] were found to be influential. Confirming the fact that the meteorology at the time of emissions is so important is still astonishing, since the NO_x-O_3 effects evolve over several months. These results also confirm the findings of Frömming *et al.* [33] and Rosanka *et al.* [74] which indicate that the transport pathway at the time of the NO_x emission for the first few days strongly determine the fate of O_3 change. It was also shown that the chained model performs better than the standard model in significant ways. This new surrogate model was shown to converge as more data is used and was found to perform significantly better than linear regression models. The use of the model is demonstrated by predicting and discussing the climate impact of a frequently flown flight in the European Union at different flight times. The improved ability to predict instantaneous RF of O_3 from NO_x on a regular basis with varying confidence levels increases the potential of global climate-optimised flight planning. The latter can be achieved first by converting the predicted RF to probabilistic algorithmic climate change functions for O_3 ($paCCF_{O_3}$), which represent ATR of O_3 over a selected time horizon due to local aviation NO_x emissions. Secondly, by

applying the probabilistic framework to other climate forcing agents such as NO_x-CH_4, H_2O, contrails, and aerosols and converting them to paCCFs. Thus, for the first time, a probabilistic surrogate model based on Gaussian processes was identified successfully as a UQ technique to predict the O_3 RF for local NO_x emissions, with a higher accuracy than past known surrogate models in literature.

6.2. Outlook

After reviewing the results and addressing to what extent the research questions have been answered, some specific limitations and future recommendations are addressed here:

- In Chapter 3, the sensitivity of PCC and the subsequent contrail impact to input temperature was analysed. A temperature correction term of 3K was determined, but this was based on data available for a single winter day (18th December 2015). Secondly, no statistically significant correlation was found between the temperature bias and the nudged EMAC data, and restricting the analysis to a small dataset is possibly an important factor that contributed to this. In terms of sensitivity, it was found that both the PCC and the contrail aCCFs are extremely sensitive to small changes in temperature. Thus, using the temperature bias is recommended only as a short-term fix to be used in the CONTRAIL and ACCF submodel during winter simulations and in the Northern hemisphere. The derivation of contrail aCCFs itself is based on a RF dataset in the North-Atlantic region during specific winter periods. Contrails, however, are produced in several other regions and seasons, that are not taken into account. A large number of sources of uncertainties were also identified for the impact of contrails. One important component comprises the uncertainties regarding the atmospheric conditions under which contrails form (Schmidt Appleman Criterion (SAC)) and persist (ice-supersaturation). To address this source of uncertainty, as a first step, the relevant meteorological variables (e.g., temperature) associated with contrail formation and persistence may be modelled as random variables and propagated through the CONTRAIL submodel. As a second step, remote sensing data may be examined to detect the formation of contrails across the globe. Then, the pdfs on the input variables that are consistent with the observed outputs can be obtained uniquely using Bayesian inversion.

- In Chapter 4, air traffic was optimised laterally (fixing a cruise altitude) and vertically (restricting lateral movements) with respect to two objectives: minimising O_3 aCCFs, and minimising cost. These objectives were used to assess the horizontal and vertical structure of the O_3 aCCFs in a case study chosen to be appropriate and were shown to be positive, but to different degrees. There is an indication that despite consuming more fuel and emitting more NO_x, the climate impact from laterally optimised flights were lower on average, which can be attributed to the location and dispersion of NO_x emissions at the chosen cruise altitude. It would certainly help extending this analysis to lower and higher cruise levels so that it is easier to compare these findings with other existing studies. Another way of enhancing this study is considering not just days characterised by summer and

winter, but also other seasons, and possibly other weather patterns, which would indicate any special features surrounding atmospheric transport of emissions and photochemical rates influencing NO_x-O_3 chemistry.

- In Chapter 5, the heteroscedastic Gaussian process model was shown to be superior in various ways to linear regression surrogates, in particular, the O_3 aCCFs. While the most comprehensive global dataset is used for training the models, it is limited to two specific days, only. Although there are computational limitations to calculate these datasets, running the EMAC model for a few more days and regions, characterised by other seasons and cyclical events such as El Niño and La Niña can also be used additionally to train the surrogate model. Further improvements could also be made in the data generation process itself, involving the submodel AIRTRAC, by taking into account more tagged processes and using fewer modelling assumptions. If this is not computationally convenient, in the short-term, specific correction factors derived by Maruhashi *et al.* [136] may be used. Converting the instantaneous RF to paCCFs requires a parameterisation that can be obtained by running additional global simulations, that are not carried out in this work. Another key point is that both the aCCFs and paCCFs rely on using weather data at the point of release of the emission, i.e., only local data is considered. While this is useful, it may not capture all the relevant physics governing atmospheric transport and chemistry, and could be the primary reason for large uncertainties in climate impact predictions. The use of non-local features is advised, by incorporating more contextual information surrounding the emission location. This entails using feature information over a pre-defined region around the emission location. However, there are several challenges that have to be addressed, details of which are available in Section 5.6 of Chapter 5. While the paCCFs do not take uncertainties in standard weather forecasts into account, it can be used along with the work of Simorgh *et al.* [155] for robust climate-optimised flight planning to overcome this limitation. While this dissertation tackles the short term NO_x-O_3 effect, which is the most significant, the long-term decrease of CH_4 and a CH_4 induced decrease of O_3 (PMO) and stratospheric water vapour can also be estimated to get the total effect of aviation NO_x. The prediction of the total NO_x effect can then be compared to with other studies that used high-fidelity simulations.

In general, the results presented in the dissertation are an important step towards climate-optimisation of individual flights by verifying for the first time the applicability of the NO_x-O_3 aCCFs including their horizontal and vertical pattern. While other studies have focused on annual or seasonal mean impacts of aviation, the concept of aCCFs is unique in relating a localised pulse emission on an arbitrary day to its potential climate impact. Going further, improvements have been achieved by using the paCCFs concept via enhanced climate impact predictions relating to O_3 change as a result of local NO_x emissions, along with heteroscedastic uncertainty estimates. This serves not only as a recipe for other climate forcing agents of aviation but also a big step towards its use in the forthcoming EU-wide Monitoring, Reporting, and Verifying (MRV) initiative, targeting non-CO_2 aviation impacts. While the main ingredients are now present for global climate-optimised flight planning, further attention can be devoted to considering ad-

ditional constraints such as air-traffic management, regulatory compliance, passenger comfort, air quality and aircraft noise.

A

Fundamentals of probability theory

This appendix contains some details from probability theory that are relevant for Chapters 2, 4 and 5.

A

A.1. Probability theory

Probability is a branch of mathematics with two commonly used interpretations- the frequentist approach and the Bayesian approach. In the former approach, probabilities are defined as the frequency with which an event occurs, when an experiment is repeated a large number of times. The latter approach is used in this work, where probabilities are interpreted as a distribution of subjective knowledge, that are updated as data are observed. Regardless of the interpretation used, mathematical concepts such as random variables, samples, probability density functions, etc. have a common logical framework.

Definition A.1.1 (Probability space)**.** A probability space $(\Omega, \mathcal{F}, P)$ consists of three components: the sample space Ω containing all possible outcomes E of an experiment, a σ-algebra of subsets of Ω, and lastly, a probability $P : \mathcal{F} \to [0,1]$.

The probability is a measure that is characterised by three Kolmogorov axioms:

1. $P(\emptyset) = 0$,
2. $P(\Omega) = 1$, and,
3. $P\left(\bigcup_{i=1}^{\infty} E_i\right) = \sum_{i=1}^{\infty} P(E_i) \;\; \forall E_i \in \mathcal{F}$ and disjoint sets, i.e., $E_i \cap E_j = \emptyset$.

Definitions for conditional probabilities include:

1. If A, B denote two events, the joint probability of these events is defined as,

$$P(A,B) := P(A \cap B) = P(A|B)P(B)\,,$$

   where $P(A|B)$ is the conditional probability of A occurring, given that B has already occurred.

2. If A, B are independent events, i.e., they have no influence over each other, $P(A|B) = P(A)$. Then their joint probability is given by,

$$P(A,B) := P(A \cap B) = P(A)P(B)\,.$$

Definition A.1.2 (Random variable)**.** A random variable defined on a probability space $(\Omega, \mathcal{F}, P)$ is a function $X : \Omega \to \mathcal{X}$ such that $\{\omega \in \Omega | X(\omega) \leq x\} \in \mathcal{F}$.

If $\mathcal{X}$ is a countable set $\{x_1, x_2, \ldots, x_n\} \in \mathbb{R}$ then X is a discrete random variable. On the other hand, X is a continuous random variable. The particular values in $\mathcal{X}$ taken by the random variable are termed realisations or samples. For every such random variable, we have a Cumulative Distribution Function (cdf).

Definition A.1.3 (Cumulative Distribution Function)**.** A cdf is a function $F_X : \mathbb{R} \to [0,1]$ such that $F_X(x) = P\{\omega \in \Omega | X(\omega) \leq x\}$.

The cdf ascribes a probability that a random variable $X \leq x$. The cdf is always right continuous due to the following properties:

1. $\lim_{x\to\infty^-} F_X(x) = 0$,
2. If $x_1 \le x_2$, $F_X(x_1) \le F_X(x_2)$, and,
3. $\lim_{x\to\infty^+} F_X(x) = 1$.

Definition A.1.4 (Probability Density Function)**.** A random variable is continuous if the cdf is absolutely continuous, i.e., $\exists \rho_X$ such that,

$$F_X(x) = \int_{-\infty}^{x} \rho_X(s)\mathrm{d}s,\ x \in \mathbb{R}.$$

Then, the probability density function (pdf) is the derivative of the cdf, $\rho_X = \frac{\mathrm{d}F_X}{\mathrm{d}x}$, which is a mapping $\mathbb{R} \to [0,\infty)$ with the following properties:

1. $\rho_X(x) \ge 0$,
2. $\int_{\mathbb{R}} \rho_X(x)\mathrm{d}x = 1$, and,
3. $P(x_1 \le X \le x_2) = F_X(x_2) - F_X(x_1) = \int_{x_1}^{x_2} \rho_X(x)\mathrm{d}x$.

Some key attributes by which these densities are often characterised include their location or centrality, variability or spread, symmetry, and tail behaviour. This information is provided by the mean, variance, skewness, and kurtosis, respectively and are collectively called statistical moments. The mean or expectation is the first moment of a random variable X, and is a measure of the central location of the pdf. It is defined as,

$$\mathbb{E}[X] = \mu := \int_{\mathbb{R}} x\rho_X(x)\mathrm{d}x.$$

The variance of X is the second moment and is a measure of the squared deviation from the mean. It is defined as,

$$\mathbb{V}[X] = \sigma^2 := \mathbb{E}[(X-\mu)^2] = \int_{\mathbb{R}} (x-\mu)^2\rho_X(x)\mathrm{d}x.$$

The standard deviation $\sigma = \sqrt{\mathbb{V}[X]} > 0$ and has the same units as μ.

Since we characterise uncertain parameters using random variables, the relationship between random variables and their samples, cdf, and pdf are essential.

A.1.1. Common densities

A normal or Gaussian distribution is one of the most commonly used densities in uncertainty quantification, and has a well-defined mean and variance. For $x \in \mathbb{R}$, it is given by,

$$\rho_X(x) = \frac{1}{\sigma\sqrt{2\pi}} \exp\left(-\frac{(x-\mu)^2}{2\sigma^2}\right).$$

A

A random variable X that is normally distributed is centred with mean μ, has a variance σ^2, and is often denoted as $X \sim \mathcal{N}(\mu, \sigma^2)$. Close to 70% and 95% of the samples of X lie within 1σ and 2σ, respectively. Gaussian distributions are commonly seen in biology, finance, measurement errors, and standardised testing.

Another common density is the uniform distribution where every outcome of an experiment has equal probability over an interval $[a, b]$. A random variable X that is uniformly distributed is denoted as $X \sim \mathcal{U}(a, b)$ and defined as,

$$\rho_X(x) = \begin{cases} \frac{1}{b-a}, & \text{if } a \leq x \leq b \\ 0, & \text{otherwise.} \end{cases}$$

A simple example is an idealised random number generator, where each outcome has equal probability.

Figure A.1 shows the pdf and cdf of these densities.

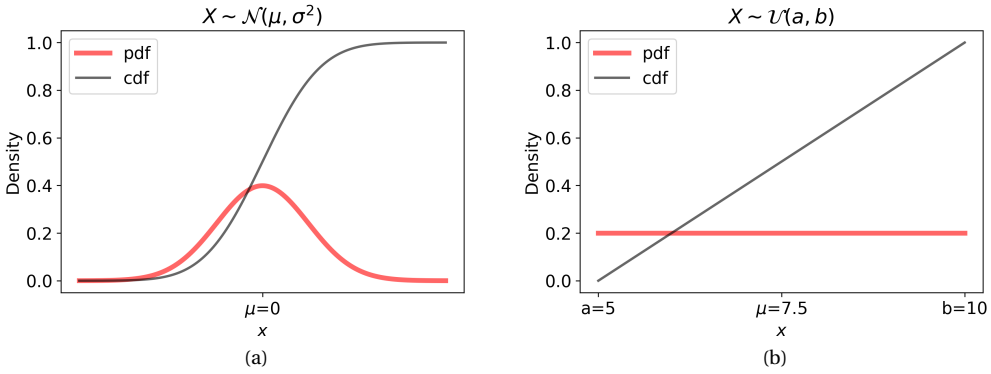

Figure A.1: The pdf and cdf of a **(a)** Gaussian distribution, $\mathcal{N}(0, 1)$ and **(b)** Uniform distribution, $\mathcal{U}(5, 10)$.

A.1.2. Estimating densities

Histograms and kernel density estimators (KDEs) are two commonly used methods to estimate the probability density function of a random variable when a moderate number of samples are available.

1. Histograms

   Constructing a histogram involves dividing the available range of samples, $\{x_1, \ldots, x_n\}$ of X into bins, $\{B_k\}$ with intervals $[t_k, t_{k+1})$ for $k = -\infty, \ldots, -1, 0, 1, \ldots \infty$ and checking the frequency of values, v_k for each interval. The bins are adjacent to each other, do not overlap, and usually are of the same size. The height of each bin is proportional to the frequency of samples in it and are often normalised such that the total bin area = 1. The choice of bin-width and end points highly impacts the estimate $\hat{\rho}_X(x)$ of the true density. For continually measured data, Scott's rule [156] is a rule-of-thumb formula that yields an optimal bin-width choice given by,

$$\hat{h} = \frac{3.5\,\hat{\sigma}_x}{n^{1/3}}\,, \quad \hat{\sigma}_x = \sqrt{\frac{1}{n-1}\sum_{i=1}^{n}(x_i - \bar{x})^2},$$

where $\hat{\sigma}_x$ and $\bar{x}$ is the standard deviation and mean, respectively, for n samples. The histogram is then given by,

$$\hat{\rho}_X(x) = \frac{v_k}{n\hat{h}}, \quad x \in B_k\,.$$

While constructing histograms is straightforward in one dimension, it is difficult to implement in multiple dimensions [157].

2. KDEs

Unlike a histogram, a KDE offers a smooth estimate $\hat{\rho}_X(x)$ of the true pdf with the help of a kernel function $K(x) \geq 0$ which is associated with smoothing parameter, $h > 0$ called bandwidth. Several kernel functions are available, but the standard normal kernel is most commonly used due to mathematical convenience. Similar to histograms, the resulting estimate $\hat{\rho}_X(x)$ is sensitive to the chosen bandwidth and an optimal choice [146] can be used,

$$\hat{h} = \frac{1.06\,\hat{\sigma}_x}{n^{1/5}}\,.$$

The KDE with unit area is then given by,

$$\hat{\rho}_X(x) = \frac{1}{n\hat{h}}\sum_{i=1}^{n} K\left(\frac{x - x_i}{\hat{h}}\right),$$

where $K(x) = \frac{1}{\sqrt{2\pi}}\exp(\frac{-x^2}{2})$. Thus, each kernel function is centred on a sample and the KDE is given by the sum of all kernel functions divided by $n\hat{h}$ so that $\int_{\mathbb{R}} \hat{\rho}_X(x)\mathrm{d}x = 1$. KDEs can be viewed as a generalisation of the histogram and can be used for higher dimensions.

To illustrate the difference between histograms and KDEs, we generate 1000 samples from a non-standard pdf and construct estimates with and without the optimal bin-width and bandwidth (Fig. A.2). The sensitivity of the pdf estimates to the selected parameters is evident and must be chosen carefully.

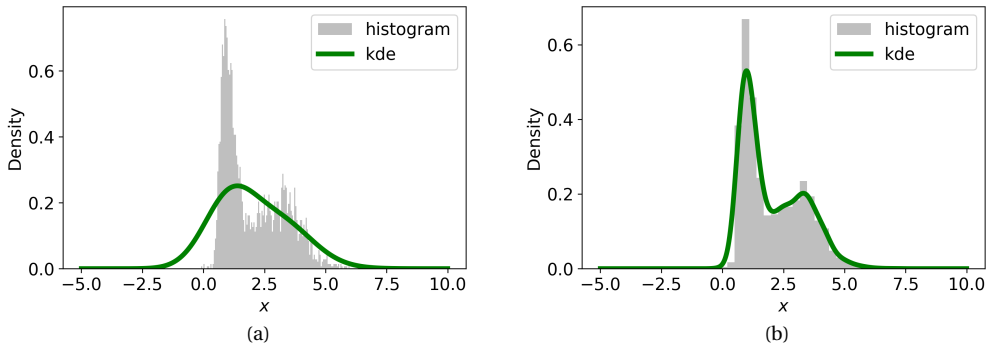

Figure A.2: Constructing pdf estimates in terms of histograms and kdes by **(a)** manually selecting parameters **(b)** using Scott's rule.

A.1.3. Limit theorems

Two important theorems with respect to random variables are the law of large numbers (LLN) and the central limit theorem (CLT). Suppose we want to estimate μ and σ^2 of a population, for which we have some samples $x_1, \ldots, x_n$ associated with random variables $X_1, \ldots, X_n$. An estimator for mean, also called sample mean, is given by,

$$\bar{X}_n = \frac{1}{n} \sum_{i=1}^{n} X_i \, .$$

The strong form of the LLN states that if the random variables are independently and identically distributed (iid) with $\mathbb{E}[X_i] = \mu$, $\mathbb{V}[X_i] = \sigma^2 < \infty$, then, for small $\epsilon > 0$,

$$P\left(\lim_{n \to \infty} |\bar{X}_n - \mu| < \epsilon \right) = 1 \implies \bar{X}_n \xrightarrow{a.s} \mu,$$

implying that the sample mean almost surely $(a.s)$ converges to the population mean. The classical CLT states that the distribution of $Z_n = \dfrac{\bar{X}_n - \mu}{\sigma / \sqrt{n}}$ approaches a standard normal one $\mathcal{N}(0,1)$ as $n \to \infty$, regardless of the original distribution of X. This is equivalent to stating $\bar{X}_n \sim \mathcal{N}\left(\mu, \dfrac{\sigma^2}{n}\right)$ as $n \to \infty$.

The LLN and CLT are illustrated in Fig. A.3 where the true pdf and the estimates in terms of the histogram and kde are included in Fig. A.3b for illustrative purposes. Despite sampling from a uniform distribution (Fig. A.3a), the sampling distribution of the mean approaches a Gaussian (Fig. A.3b).

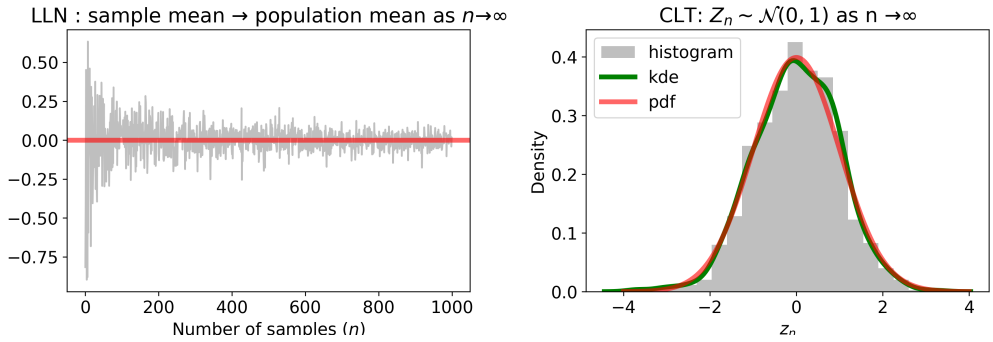

Figure A.3: Taking samples from $X \sim \mathcal{U}(10,100)$, we see in practice the two limit theorems: **(a)** LLN, and **(b)** CLT.

A.1.4. Multivariate random variables

In uncertainty quantification, there are often multiple parameters, each represented by a random variable. Extending the univariate case discussed so far, helps in analysing various useful properties. Placing the random variables in a vector, $X = [X_1, \dots, X_n]^\top$ is a mapping $X : \Omega \to \mathbb{R}^n$ with a joint cdf $F_X : \mathbb{R}^n \to [0,1]$ given by,

$$F_X(x) := F_{X_1,\dots,X_n}(x_1,\dots,x_n) = P(X_1 \le x_1,\dots,X_n \le x_n)\,.$$

The joint pdf of the random variables in the vector is given by the derivative of the joint cdf,

$$\rho_X(x) := \rho_{X_1,\dots,X_n}(x_1,\dots,x_n) = \frac{\partial^n F_{X_1,\dots,X_n}(x_1,\dots,x_n)}{\partial x_1,\dots,x_n}\,,$$

where $\int_{x_1} \cdots \int_{x_n} \rho_X(x_1,\dots,x_n)\,\mathrm{d}x_n \dots \mathrm{d}x_1 = 1$, as usual. The marginal pdf of any member of vector X involves integrating the joint pdf with respect to all other members. For example, the marginal pdf of X_1 is,

$$\rho_{X_1}(x_1) = \int_{x_2} \cdots \int_{x_n} \rho_X(x_1,\dots,x_n)\,\mathrm{d}x_n \dots \mathrm{d}x_2\,.$$

Another important density is the conditional pdf. The conditional pdf of $X_2 \dots X_n$ when X_1 is fixed at a specific value, is given by,

$$\rho_{X_2,\dots,X_n|X_1}(x_2,\dots,x_n|x_1) = \frac{\rho_X(x_1,\dots,x_n)}{\rho_{X_1}(x_1)} \quad , \rho_{X_1}(x_1) > 0\,.$$

A.1.5. Bayes' theorem

If we consider a random vector with two random variables X_1, X_2, we can express their conditional pdfs,

A

$$\rho_{X_1|X_2}(x_1|x_2) = \frac{\rho_X(x_1,x_2)}{\rho_{X_2}(x_2)}$$
$$\rho_{X_2|X_1}(x_2|x_1) = \frac{\rho_X(x_1,x_2)}{\rho_{X_1}(x_1)}\,.$$

Combining these together, Bayes theorem relates expresses one conditional pdf with respect to the other,

$$\rho_{X_1|X_2}(x_1|x_2) = \frac{\rho_{X_2|X_1}(x_2|x_1)\,\rho_{X_1}(x_1)}{\rho_{X_2}(x_2)}$$

Bayes' theorem is used for statistical inference whereby we update the probability of an existing hypothesis H after gathering evidence E. Thus, $P(H|E) \propto P(E|H)\,P(H)$. Here, $P(H)$ is commonly called prior, $P(E|H)$ is the probability of seeing the evidence, given that the hypothesis holds. This is called likelihood, and $P(H|E)$ is the updated belief and called posterior.

A.1.6. Correlation of random variables

The covariance of any two random variables X_1 and X_2 is defined as,

$$\mathrm{Cov}[X_1,X_2] := \mathbb{E}[(X_1 - \mathbb{E}[X_1])(X_2 - \mathbb{E}[X_2])]$$

and yields a single number. The covariance of a variable with itself is the variance, $\mathrm{Cov}[X_1,X_1] = \mathbb{V}[X_1]$, as defined earlier. The covariance is symmetric; that is, $\mathrm{Cov}[X_1,X_2] = \mathrm{Cov}[X_2,X_1]$. The measure of correlation between X_1 and X_2 can be measured by the Pearson correlation coefficient,

$$\mathcal{C}_{X_1X_2} = \frac{\mathrm{Cov}[X_1,X_2]}{\sigma_{X_1}\sigma_{X_2}} \in [-1,1].$$

If $|\mathcal{C}_{X_1X_2}| = 1$, X_1 and X_2 have a perfect linear correlation. A positive value indicates that X_1 increases as X_2 increases, and vice versa, for negative values. If X_1 and X_2 are independent, then $\mathrm{Cov}[X_1,X_2] = 0 \implies \mathcal{C}_{XY} = 0$; the variables are uncorrelated. The converse however, is not generally true. For instance, if X_1 is symmetric about a zero origin and $X_2 = X_1^2$, then it can be shown that $\mathrm{Cov}[X_1,X_2] = 0$ although the two variables are clearly dependent. Thus, the Pearson correlation coefficient should only be used to measure the linear relationship between two variables.

An alternative measure is the mutual information (MI) which measures relationships between any two random variables, for which a moderate number of samples are available. Intuitively, it tells us how much we learn about one random variable by knowing the value of the other random variable. The MI between two univariate random variables X and Y is given by,

$$\mathcal{I}(X_1;X_2) = \mathrm{KL}(\rho_{X_1,X_2}(x_1,x_2)||\rho_{X_1}(x_1)\rho_{X_2}(x_2)) = \int_{x_1}\int_{x_2}\rho_{X_1,X_2}(x_1,x_2)\log\frac{\rho_{X_1,X_2}(x_1,x_2)}{\rho_{X_1}(x_1)\rho_{X_2}(x_2)}\mathrm{d}x_2\,\mathrm{d}x_1,$$

where KL($\rho(a)||\rho(b)$) represents the KL divergence between two probability density functions (pdfs), is ≥ 0 and it is a unit of statistical distance. A value of 0 indicates no correlation. For the example above, consider $X_1 \sim \mathcal{N}(3,1)$ and $X_2 = X_1^2$. The MI score, $\mathcal{I}(X_1; X_2) \approx 5$ based on 1000 samples, indicates a strong correlation, which is not detected by the Pearson correlation coefficient.

A.1.7. Multivariate Gaussians

A multivariate Gaussian distribution for a random vector is denoted as $X \sim \mathcal{N}(\boldsymbol{\mu}, \Sigma)$, where $\boldsymbol{\mu}$ represents the expectation of each random variable in the vector X and Σ is the covariance matrix,

$$\boldsymbol{\mu} = [\mu_1, \ldots, \mu_n]^\top, \; \Sigma = \begin{bmatrix} \mathbb{V}[X_1] & \mathrm{Cov}[X_1, X_2] & \cdots & \mathrm{Cov}[X_1, X_n] \\ \mathrm{Cov}[X_2, X_1] & \mathbb{V}[X_2] & \cdots & \mathrm{Cov}[X_2, X_n] \\ \vdots & \vdots & & \vdots \\ \mathrm{Cov}[X_n, X_1] & \mathrm{Cov}[X_n, X_2] & \cdots & \mathbb{V}[X_n] \end{bmatrix}.$$

The joint pdf is given by,

$$\rho_X(\boldsymbol{x}) = \frac{1}{\sqrt{(2\pi)^n |\Sigma|}} \exp\left[-\frac{1}{2} (\boldsymbol{x} - \boldsymbol{\mu})^\top \Sigma^{-1} (\boldsymbol{x} - \boldsymbol{\mu}) \right].$$

where $|\Sigma|$ is the determinant of the covariance matrix. The marginal densities $\rho(X_i)$ and conditional densities of all combinations $\rho(X_i | X_j = a)$ for $i \neq j$ are also Gaussian. They are of the form $\rho(X_i) = \mathcal{N}(\mu_i, \Sigma_{ii})$ and $\rho(X_i | X_j = a) = \mathcal{N}(\bar{\mu}, \bar{\Sigma})$ where, $\bar{\mu} = \mu_i + \Sigma_{ij}\Sigma_{jj}^{-1}(a - \mu_j)$ and $\bar{\Sigma} = \Sigma_{ii} - \Sigma_{ij}\Sigma_{jj}^{-1}\Sigma_{ji}$.

B

List of EMAC submodels used

This appendix contains a table indicating the list of submodels used in the EMAC simulation setup for Chapter 4.

B

Table B1: List of EMAC submodels used in the simulations.

Submodel	Purpose	Reference
AEROPT	Aerosol optical properties for the radiation scheme	[84]
ACCF 1.0	Climate impact of aviation emissions and contrails calculation	[14]
AIRTRAF 2.0	Air traffic simulation	[110]
CH4 1.0	Simple methane chemistry	[158]
CLOUD	Standard ECHAM5 cloud microphysics calculation	[81]
CLOUDOPT	Cloud optical properties calculation for the radiation scheme	[84]
CVTRANS	Calculates the transport of tracers due to convection	[159]
CONVECT	Convection process calculation	[160]
CONTRAIL	Contrail potential coverage calculation	Supplement of [38]; [41]
DDEP	Dry deposition of gas phase and aerosol tracers	[161]
E5VDIFF	ECHAM5 vertical diffusion and land-atmosphere exchange	[44]
GWAVE	Gravity waves calculation	[44]
JVAL	Photolysis rates	[162]
LNOX	Lighting NO_x production	[163]
MSBM	Multi-phase stratospheric box model calculates the heterogeneous reaction rates on polar stratospheric cloud particles and stratospheric background aerosols	[44]
MECCA	Calculates tropospheric and stratospheric chemistry	[97]
O3ORIG	To trace the origin of ozone	[164]
OFFEMIS	Prescribed emissions of trace gases and aerosols	[165]
ONEMIS	Online calculated emissions of trace gases and aerosols	[165]
ORBIT	Earth orbit calculation for solar zenith angle, etc.	[84]
RAD	Simulates the radiative flux	[84]
SCAV	Simulates the process of wet deposition and liquid phase chemistry	[166]
SCALC	Simple calculations with channel objects to separate the AirTraf ozone from other ozone sources	[44]
SEDI	Sedimentation of aerosol particles	[161]
SURFACE	Calculates the surface temperature	[44]
TAGGING 1.1	Tag the emissions contributions to concentrations	[91]
TNUDGE	Tracer nudging	[165]
TROPOP	Tropopause and other diagnosis	[86]

C

Variables considered for feature selection

This appendix contains the list of variables considered for feature selection (Section 5.4.2) in Chapter 5.

Table C1: List of variables considered for feature selection. The first column indicates variable names based on how they appear in CCM output files. The variables shown in bold text are the ten features that were highest scoring based on mutual information (MI) scores. These were narrowed down to five features: Temperature, geopotential, solar irradiance, zonal wind velocity, and release location of emissions.

Name	Description	Units	Dimensions
ahfice	Conductive heat flux	W m^{-2}	3D
aprc	Convective precipitation	kg m^{-2} s^{-1}	3D
aprl	Large scale precipitation	kg m^{-2} s^{-1}	3D
aprs	Snowfall	kg m^{-2} s^{-1}	3D
aps	Surface pressure	Pa	3D
cossza	Cosine of solar zenith angle	-	3D
geopot	**Geopotential**	m^2 s^{-2}	4D
geosp	Surface geopotential	m^2 s^{-2}	3D
NOX	Mixing ratios of background NO_x	mol mol^{-1}	4D
PV	**Potential vorticity**	PVU	4D
qm1	**Specific humidity**	kg kg^{-1}	4D
qsl	Humidity saturated over land	-	3D
qsw	Humidity saturated over water	-	3D
qsi	Humidity saturated over ice	-	3D
qte	Specific humidity tendency	kg kg^{-1} s^{-1}	4D
qte	Vertically integrated water vapour	kg m^{-2}	3D
qvi	Specific humidity tendency	kg kg^{-1} s^{-1}	4D
rhum	**Relative humidity**	%	4D
routes_out	Flight route data including **release location**	(multiple)	4D
srfl_physc	Solar surface flux	W m^{-2}	3D
tm1	**Dry air temperature**	K	4D
tpot	Potential temperature	K	4D
ts1m1	Surface temperature of land	K	3D
tsw	Surface temperature of water	K	3D
tte	Dry air temperature tendency	K	4D
tvirt	Virtual temperature	K	4D
um1	**Zonal wind velocity**	m s^{-1}	4D
vm1	**Meridional wind velocity**	m s^{-1}	4D
vom1	Vorticity	s^{-1}	4D
vervel	**Vertical wind velocity**	m s^{-1}	4D
xi	Cloud ice	kg kg^{-1}	4D
xl	Cloud water	kg kg^{-1}	4D
xlvi	Vertically integrated cloud ice	kg m^{-2}	3D
xlvl	Vertically integrated cloud water	kg m^{-2}	3D
zi0	**Solar irradiance**	W m^{-2}	3D
zust	Surface friction velocity	m s^{-1}	3D

D

Estimation of climate impact by Gaussian process models

This appendix contains few figures that are relevant for Section 5.4.3 of Chapter 5.

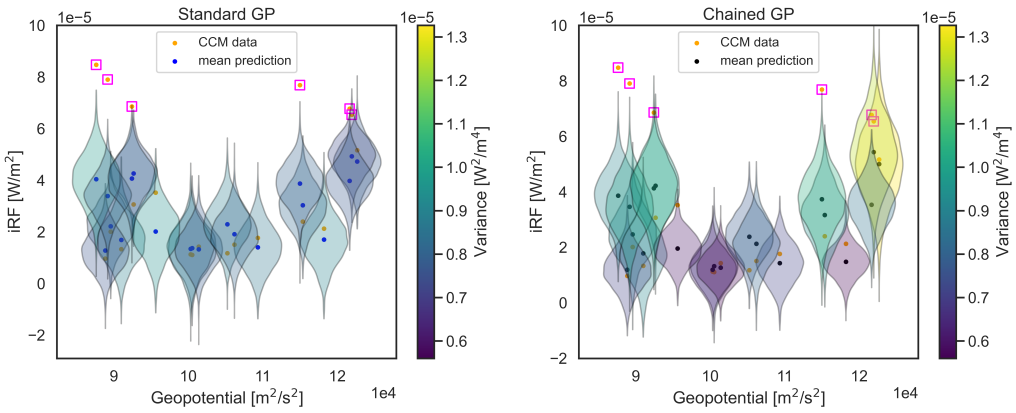

Figure D1: Violin plot of iRF test data and predictions against Geopotential from (left) the standard model and, (right) the chained GP model.

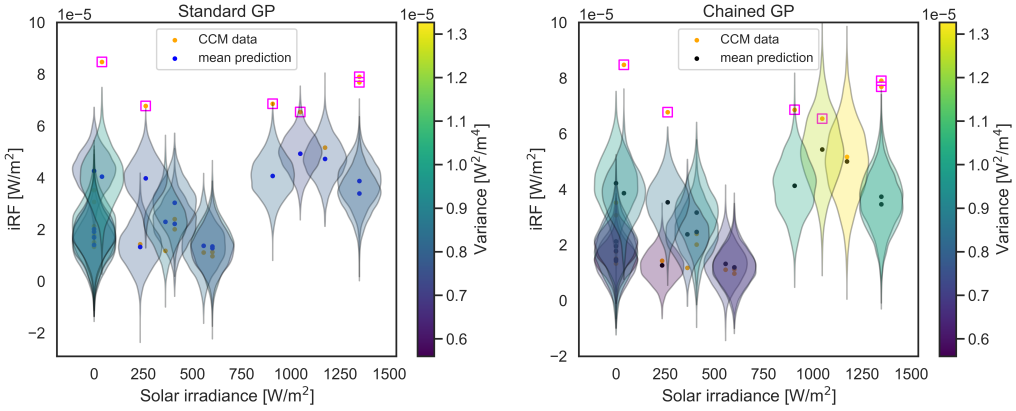

Figure D2: Violin plot of iRF test data and predictions against Solar irradiance from (left) the standard model and, (right) the chained GP model.

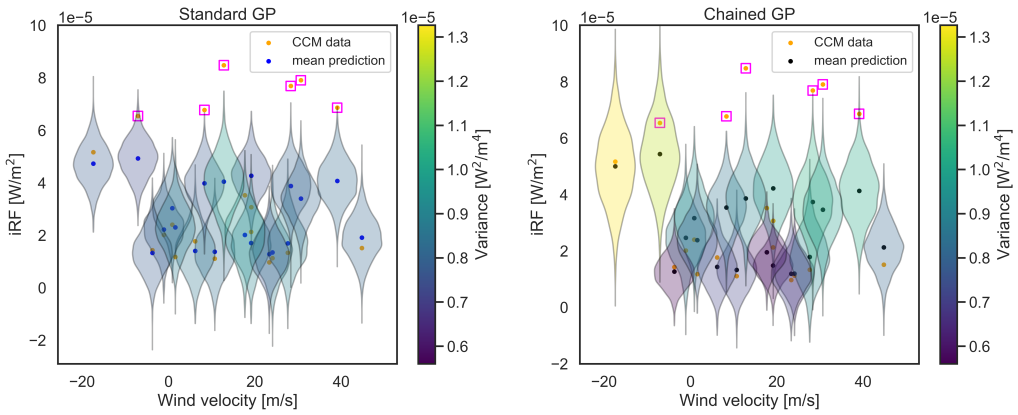

Figure D3: Violin plot of iRF test data and predictions against zonal wind velocity from (left) the standard model and, (right) the chained GP model.

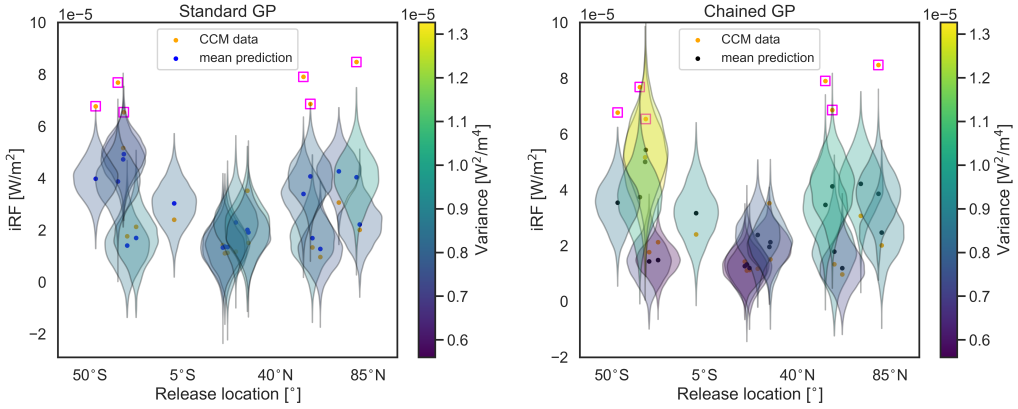

Figure D4: Violin plot of iRF test data and predictions against Release location from (left) the standard model and, (right) the chained GP model.

Bibliography

1. Hopkin, M. Greenhouse-gas levels highest for 650,000 years. *Nature* (2005).
2. IPCC. *Climate Change 2023: Synthesis Report, Summary for Policymakers. Contribution of Working Groups I, II and III to the Sixth Assessment Report of the Intergovernmental Panel on Climate Change [Core Writing Team, H. Lee and J. Romero (eds.)]. IPCC, Geneva, Switzerland.* 1–34 (2023).
3. Khalfan, A. *et al. Climate Equality: A planet for the 99 %* (Oxfam International, 2023).
4. IPCC. in *Climate Change 2021 – The Physical Science Basis* 1513–1766 (Cambridge University Press, 2021). ISBN: 9781009157896.
5. Hickel, J. *Less is more: How degrowth will save the world* ISBN: 978-1786091215 (Windmill Books, 2021).
6. Cockshott, W. P., Dapprich, J. P. & Cottrell, A. *Economic planning in an age of climate crisis* ISBN: 979-8360125563 (2022).
7. Saito, K. *Marx in the Anthropocene* (Cambridge University Press, 2023).
8. IPCC. Climate change 2013: the physical science basis. *Contribution of working group I to the fifth assessment report of the intergovernmental panel on climate change* **1535** (2013).
9. United Nations Framework Convention on Climate Change. *Paris Agreement* Accessed: 14th December 2023. https://unfccc.int/process-and-meetings/the-paris-agreement/the-paris-agreement.
10. Fuglestvedt, J. S. *Climatic Change* **58,** 267–331 (2003).
11. Grewe, V. & Dahlmann, K. How ambiguous are climate metrics? And are we prepared to assess and compare the climate impact of new air traffic technologies? *Atmospheric Environment* **106,** 373–374 (2015).
12. Fuglestvedt, J. S. *et al.* Transport impacts on atmosphere and climate: Metrics. *Atmospheric Environment* **44,** 4648–4677 (2010).
13. De F. Forster, P. M., Shine, K. P. & Stuber, N. It is premature to include non-CO2 effects of aviation in emission trading schemes. *Atmospheric Environment* **40,** 1117–1121 (2006).
14. Yin, F. *et al.* Predicting the climate impact of aviation for en-route emissions: the algorithmic climate change function submodel ACCF 1.0 of EMAC 2.53. *Geoscientific Model Development* **16,** 3313–3334 (2023).
15. Lee, D. S. *et al.* Transport impacts on atmosphere and climate: Aviation. *Atmospheric Environment* **44,** 4678–4734 (2010).

16. Dube, K. Emerging from the COVID-19 Pandemic: Aviation Recovery, Challenges and Opportunities. *Aerospace* **10,** 19 (2022).

17. Morris, G. A., Rosenfield, J. E., Schoeberl, M. R. & Jackman, C. H. Potential impact of subsonic and supersonic aircraft exhaust on water vapor in the lower stratosphere assessed via a trajectory model. *Journal of Geophysical Research: Atmospheres* **108.** ISSN: 0148-0227 (2003).

18. Wilcox, L. J., Shine, K. & Hoskins, B. Radiative forcing due to aviation water vapour emissions. *Atmospheric Environment* **63,** 1–13. ISSN: 1352-2310 (2012).

19. Gauss, M., Isaksen, I. S. A., Lee, D. S. & Søvde, O. A. Impact of aircraft NO_x emissions on the atmosphere – tradeoffs to reduce the impact. *Atmospheric Chemistry and Physics* **6,** 1529–1548. ISSN: 1680-7324 (2006).

20. Gilmore, C. K., Barrett, S. R. H., Koo, J. & Wang, Q. Temporal and spatial variability in the aviation NO x -related O 3 impact. *Environmental Research Letters* **8,** 034027 (2013).

21. Köhler, M., Rädel, G., Shine, K., Rogers, H. & Pyle, J. Latitudinal variation of the effect of aviation NOx emissions on atmospheric ozone and methane and related climate metrics. **64,** 1–9 (2013).

22. Freeman, S., Lee, D. S., Lim, L. L., Skowron, A. & De León, R. R. Trading off Aircraft Fuel Burn and NOx Emissions for Optimal Climate Policy. *Environmental Science & Technology* **52,** 2498–2505. ISSN: 1520-5851 (2018).

23. Kapadia, Z. Z. *et al.* Impacts of aviation fuel sulfur content on climate and human health. *Atmospheric Chemistry and Physics* **16,** 10521–10541. ISSN: 1680-7324 (2016).

24. Righi, M., Hendricks, J. & Sausen, R. The global impact of the transport sectors on atmospheric aerosol: simulations for year 2000 emissions. *Atmospheric Chemistry and Physics* **13,** 9939–9970. ISSN: 1680-7324 (2013).

25. Righi, M., Hendricks, J. & Sausen, R. The global impact of the transport sectors on atmospheric aerosol in 2030 – Part 2: Aviation. *Atmospheric Chemistry and Physics* **16,** 4481–4495. ISSN: 1680-7324 (2016).

26. Kärcher, B. *et al.* A unified model for ultrafine aircraft particle emissions. *Journal of Geophysical Research: Atmospheres* **105,** 29379–29386. ISSN: 0148-0227 (2000).

27. Schumann, U. Formation, properties and climatic effects of contrails. *Comptes Rendus Physique* **6,** 549–565 (2005).

28. Avila, D., Sherry, L. & Thompson, T. Reducing global warming by airline contrail avoidance: A case study of annual benefits for the contiguous United States. *Transportation Research Interdisciplinary Perspectives* **2,** 100033. ISSN: 2590-1982 (2019).

29. Grewe, V. *et al.* Evaluating the climate impact of aviation emission scenarios towards the Paris agreement including COVID-19 effects. *Nature Communications* **12** (2021).

30. Brazzola, N., Patt, A. & Wohland, J. Definitions and implications of climate-neutral aviation. *Nature Climate Change* **12,** 761–767 (2022).

31. Grewe, V. & Stenke, A. AirClim: an efficient tool for climate evaluation of aircraft technology. *Atmospheric Chemistry and Physics* **8,** 4621–4639 (2008).
32. Köhler, M. O. *et al.* Impact of perturbations to nitrogen oxide emissions from global aviation. *Journal of Geophysical Research* **113** (2008).
33. Frömming, C. *et al.* Influence of weather situation on non-CO_2 aviation climate effects: the REACT4C climate change functions. *Atmospheric Chemistry and Physics* **21,** 9151–9172. https://acp.copernicus.org/articles/21/9151/2021/ (2021).
34. Frömming, C. *et al.* Aviation-induced radiative forcing and surface temperature change in dependency of the emission altitude. **117** (2012).
35. Søvde, O. A. *et al.* Aircraft emission mitigation by changing route altitude: A multi-model estimate of aircraft NO_x emission impact on O3 photochemistry. **95,** 468–479 (2014).
36. Matthes, S. REACT4C - Climate Optimised Flight Planning. *Innovation for Sustainable Aviation in a Global Environment. Proceedings of the Sixth European Aeronautics Days 2011* 122–128 (2012).
37. Sridhar, B., Chen, N. Y. & Ng, H. K. *Energy Efficient Contrail Mitigation Strategies for Reducing the Environmental Impact of Aviation* in (2013). https://api.semanticscholar.org/CorpusID:51915670.
38. Grewe, V. *et al.* Reduction of the air traffic's contribution to climate change: A REACT4C case study. *Atmospheric Environment* **94,** 616–625 (2014).
39. Grewe, V. *et al.* Aircraft routing with minimal climate impact: the REACT4C climate cost function modelling approach (V1.0). *Geoscientific Model Development* **7,** 175–201 (2014).
40. Hartjes, S., Hendriks, T. & Visser, D. *Contrail Mitigation Through 3D Aircraft Trajectory Optimization* in (American Institute of Aeronautics and Astronautics, 2016).
41. Yin, F., Grewe, V., Frömming, C. & Yamashita, H. Impact on flight trajectory characteristics when avoiding the formation of persistent contrails for transatlantic flights. *Transportation Research Part D: Transport and Environment* **65,** 466–484 (2018).
42. Van Manen, J. & Grewe, V. Algorithmic climate change functions for the use in eco-efficient flight planning. *Transportation Research Part D: Transport and Environment* **67,** 388–405 (2019).
43. in. *The Concise Encyclopedia of Statistics* 88–91 (Springer New York, 2008).
44. Jöckel, P. *et al.* Development cycle 2 of the Modular Earth Submodel System (MESSy2). *Geoscientific Model Development* **3,** 717–752 (2010).
45. On Climate Change (IPCC), I. P. *Climate Change 2001: The Scientific Basis* tech. rep. (Intergovernmental Panel on Climate Change, 2001).
46. Dörnbrack, A. in *Research Topics in Aerospace* 3–16 (Springer Berlin Heidelberg, 2012). ISBN: 9783642301834.

47. Trenberth, K. E. & Cheng, L. A perspective on climate change from Earth's energy imbalance. *Environmental Research: Climate* **1,** 013001. ISSN: 2752-5295 (2022).

48. Trenberth, K. E., Fasullo, J. T. & Kiehl, J. Earth's Global Energy Budget. *Bulletin of the American Meteorological Society* **90,** 311–324. ISSN: 1520-0477 (2009).

49. Stuber, N., Sausen, R. & Ponater, M. Stratosphere adjusted radiative forcing calculationsin a comprehensive climate model. *Theoretical and Applied Climatology* **68,** 125–135 (2001).

50. Hansen, J. Efficacy of climate forcings. *Journal of Geophysical Research* **110** (2005).

51. Stuber, N., Ponater, M. & Sausen, R. Why radiative forcing might fail as a predictor of climate change. *Climate Dynamics* **24,** 497–510 (2005).

52. Lee, D. S. *et al.* The contribution of global aviation to anthropogenic climate forcing for 2000 to 2018. *Atmospheric Environment* **244,** 117834 (2021).

53. Ponater, M., Marquart, S., Sausen, R. & Schumann, U. On contrail climate sensitivity. *Geophysical Research Letters* **32.** ISSN: 1944-8007 (2005).

54. Ponater, M., Pechtl, S., Sausen, R., Schumann, U. & Hüttig, G. Potential of the cryoplane technology to reduce aircraft climate impact: A state-of-the-art assessment. *Atmospheric Environment* **40,** 6928–6944. ISSN: 1352-2310 (2006).

55. On Climate Change (IPCC), I. P. Aviation and the Global Atmosphere (1999).

56. Shine, K. P., Fuglestvedt, J. S., Hailemariam, K. & Stuber, N. Alternatives to the Global Warming Potential for Comparing Climate Impacts of Emissions of Greenhouse Gases. *Climatic Change* **68,** 281–302. ISSN: 1573-1480 (2005).

57. Koch, A. *Climate Impact Mitigation Potential given by Flight Profile and Aircraft Optimization* 2013.

58. On Climate Change (IPCC), I. P. *Climate Change 2007: The Scientific Basis* tech. rep. (Intergovernmental Panel on Climate Change, 2007).

59. Boden, T., Marland, G. & Andres, R. *Global, Regional, and National Fossil-Fuel CO2 Emissions, 1751 - 2006 (published 2009)* en. 2009.

60. Wild, O., Prather, M. J. & Akimoto, H. Indirect long-term global radiative cooling from NOxEmissions. **28,** 1719–1722 (2001).

61. Myhre, G. *et al.* Radiative forcing due to stratospheric water vapour from CH_4 oxidation. *Geophysical Research Letters* **34** (2007).

62. Lee, D. S. *et al.* Aviation and global climate change in the 21st century. *Atmospheric Environment* **43,** 3520–3537 (2009).

63. Holmes, C. D., Tang, Q. & Prather, M. J. Uncertainties in climate assessment for the case of aviation NO. *Proceedings of the National Academy of Sciences* **108,** 10997–11002 (2011).

64. Grewe, V., Matthes, S. & Dahlmann, K. The contribution of aviation NO_x emissions to climate change: are we ignoring methodological flaws? *Environmental Research Letters* **14,** 121003 (2019).

65. Gimeno, L. *et al.* The residence time of water vapour in the atmosphere. *Nature Reviews Earth &amp Environment* **2,** 558–569 (2021).

66. Schmidt, E. Die Entstehung von Eisnebel aus den Auspuffgasen von Flugmotoren. *Schriften Der Dtsch. Akad. Der Luftfahrtforsch.* **44,** 1–15 (1941).

67. Appleman, H. The Formation of Exhaust Condensation Trails by Jet Aircraft. *Bulletin of the American Meteorological Society* **34,** 14–20 (1953).

68. Schumann, U. On Conditions for Contrail Formation from Aircraft Exhausts. *Meteorologische Zeitschrift* **5,** 4–23. https://elib.dlr.de/32128/ (1996).

69. Gierens, K., Lim, L. & Eleftheratos, K. A Review of Various Strategies for Contrail Avoidance. *The Open Atmospheric Science Journal* **2,** 1–7. ISSN: 1874-2823 (2008).

70. Schumann, U. Influence of propulsion efficiency on contrail formation. *Aerospace Science and Technology* **4,** 391–401. ISSN: 1270-9638 (2000).

71. Haywood, J. M. *et al.* A case study of the radiative forcing of persistent contrails evolving into contrail-induced cirrus. *Journal of Geophysical Research: Atmospheres* **114** (2009).

72. Grooß, J., Brühl, C. & Peter, T. Impact of aircraft emissions on tropospheric and stratospheric ozone. Part I. *Atmospheric Environment* **32,** 3173–3184. ISSN: 1352-2310 (Sept. 1998).

73. Grewe, V. in *Lightning: Principles, Instruments and Applications* 537–549 (Springer Netherlands). ISBN: 9781402090790.

74. Rosanka, S., Frömming, C. & Grewe, V. The impact of weather patterns and related transport processes on aviation's contribution to ozone and methane concentrations from NO_x emissions. *Atmos. Chem. Phys.* **20,** 12347–12361 (2020).

75. Stevenson, D. S. Radiative forcing from aircraft NO_x emissions : Mechanisms and seasonal dependence. **109** (2004).

76. Rasmussen, C. E. & Williams, C. K. I. *Gaussian Processes for Machine Learning* (The MIT Press, 2006).

77. Neal, R. M. *Bayesian Learning for Neural Networks* (Springer New York, 1996).

78. Zhu, C., Byrd, R. H., Lu, P. & Nocedal, J. Algorithm 778: L-BFGS-B. *ACM Transactions on Mathematical Software* **23,** 550–560 (1997).

79. Pedregosa, F. *et al.* Scikit-learn: Machine Learning in Python. *Journal of Machine Learning Research* **12,** 2825–2830 (2011).

80. Rao, P. *et al.* Case Study for Testing the Validity of NO_x-Ozone Algorithmic Climate Change Functions for Optimising Flight Trajectories. *Aerospace* **9,** 231 (2022).

81. Roeckner, E. *et al.* Sensitivity of Simulated Climate to Horizontal and Vertical Resolution in the ECHAM5 Atmosphere Model. *Journal of Climate* **19,** 3771–3791 (2006).

82. Yamashita, H. *et al.* Air traffic simulation in chemistry-climate model EMAC 2.41: AirTraf 1.0. *Geoscientific Model Development* **9,** 3363–3392 (2016).

83. Grewe, V., Tsati, E., Mertens, M., Frömming, C. & Jöckel, P. Contribution of emissions to concentrations: the TAGGING 1.0 submodel based on the Modular Earth Submodel System (MESSy 2.52). *Geoscientific Model Development* **10,** 2615–2633 (2017).

84. Dietmüller, S. *et al.* A new radiation infrastructure for the Modular Earth Submodel System (MESSy, based on version 2.51). *Geoscientific Model Development* **9,** 2209–2222 (2016).

85. Jöckel, P. *et al.* Earth System Chemistry integrated Modelling (ESCiMo) with the Modular Earth Submodel System (MESSy) version 2.51. *Geoscientific Model Development* **9,** 1153–1200 (2016).

86. Jöckel, P. *et al.* The atmospheric chemistry general circulation model ECHAM5/MESSy1: consistent simulation of ozone from the surface to the mesosphere. *Atmospheric Chemistry and Physics* **6,** 5067–5104 (2006).

87. Emmons, L. K. *et al.* Data composites of airborne observations of tropospheric ozone and its precursors. *Journal of Geophysical Research: Atmospheres* **105,** 20497–20538. ISSN: 0148-0227 (2000).

88. Simmons, A. J., Burridge, D. M., Jarraud, M., Girard, C. & Wergen, W. The ECMWF medium-range prediction models development of the numerical formulations and the impact of increased resolution. *Meteorology and Atmospheric Physics* **40,** 28–60 (1989).

89. Kerkweg, A. & Jöckel, P. The 1-way on-line coupled atmospheric chemistry model system MECO(n) – Part 1: Description of the limited-area atmospheric chemistry model COSMO/MESSy. *Geoscientific Model Development* **5,** 87–110. ISSN: 1991-9603 (2012).

90. Grewe, V. A generalized tagging method. *Geoscientific Model Development* **6,** 247–253. https://gmd.copernicus.org/articles/6/247/2013/ (2013).

91. Rieger, V. S., Mertens, M. & Grewe, V. An advanced method of contributing emissions to short-lived chemical species (OH and HO_2): the TAGGING 1.1 submodel based on the Modular Earth Submodel System (MESSy 2.53). *Geoscientific Model Development* **11,** 2049–2066. https://gmd.copernicus.org/articles/11/2049/2018/ (2018).

92. Rieger, V. *A new method to assess the climate effect of mitigation strategies for road traffic* PhD thesis (2018).

93. Roosenbrand, E., Sun, J. & Hoekstra, J. *Examining Contrail Formation Models with Open Flight and Remote Sensing Data* in (Paper presented at 12th SESAR Innovation Days, Budapest, Hungary., Nov. 2022).

94. Burkhardt, U., Kärcher, B., Ponater, M., Gierens, K. & Gettelman, A. Contrail cirrus supporting areas in model and observations. *Geophysical Research Letters* **35.** ISSN: 1944-8007 (2008).

95. Irvine, E. A., Hoskins, B. J., Shine, K. P., Lunnon, R. W. & Frömming, C. Characterizing North Atlantic weather patterns for climate-optimal aircraft routing. *Meteorological Applications* **20,** 80–93 (2012).

96. Brinkop, S. & Jöckel, P. ATTILA 4.0: Lagrangian advective and convective transport of passive tracers within the ECHAM5/MESSy (2.53.0) chemistry–climate model. *Geoscientific Model Development* **12,** 1991–2008. ISSN: 1991-9603 (May 2019).

97. Sander, R. *et al.* The atmospheric chemistry box model CAABA/MECCA-3.0. *Geoscientific Model Development* **4,** 373–380 (2011).

98. Grewe, V., Tsati, E. & Hoor, P. On the attribution of contributions of atmospheric trace gases to emissions in atmospheric model applications. *Geoscientific Model Development* **3,** 487–499. ISSN: 1991-9603 (2010).

99. Burkhardt, U. & Kärcher, B. Process-based simulation of contrail cirrus in a global climate model. *Journal of Geophysical Research: Atmospheres* **114.** ISSN: 0148-0227 (Aug. 2009).

100. Myhre, G. *et al.* Intercomparison of radiative forcing calculations of stratospheric water vapour and contrails. *Meteorologische Zeitschrift* **18,** 585–596. ISSN: 0941-2948 (2009).

101. Matthes, S. *et al.* ATM4E - A concept for environmentally-optimized aircraft trajectories. *2nd Greener Aviation 2016 Conference* (2016).

102. Penner, J. E., Lister, D. H., Griggs, D. J. & D. J. Dokken, M. M. *Aviation and the Global Atmosphere: A special report of IPCC working groups I and III on Collaboration with the Scientific Assessment Panel to the Montreal Protocol on Substances that Deplete the Ozone Layer.* 1999.

103. Holton, J. R. *et al.* Stratosphere-troposphere exchange. *Reviews of Geophysics* **33,** 403 (1995).

104. Grewe, V. & Dameris, M. Calculating the global mass exchange between stratosphere and troposphere. *Annales Geophysicae* **14,** 431–442. ISSN: 1432-0576 (1996).

105. Skowron, A., Lee, D. & León, R. D. The assessment of the impact of aviation NOx on ozone and other radiative forcing responses – The importance of representing cruise altitudes accurately. *Atmospheric Environment* **74,** 159–168 (2013).

106. Schumann, U. A contrail cirrus prediction model. *Geoscientific Model Development* **5,** 543–580. ISSN: 1991-9603 (2012).

107. Smith, R. C. *Uncertainty Quantification: Theory, Implementation, and Applications* (ed Estep, D.) (SIAM - Computational Science & Engineering, 2013).

108. Kärcher, B., Burkhardt, U., Ponater, M. & Frömming, C. Importance of representing optical depth variability for estimates of global line-shaped contrail radiative forcing. *Proceedings of the National Academy of Sciences* **107,** 19181–19184. ISSN: 1091-6490 (2010).

109. Rap, A., Forster, P. M., Haywood, J. M., Jones, A. & Boucher, O. Estimating the climate impact of linear contrails using the UK Met Office climate model. *Geophysical Research Letters* **37.** ISSN: 1944-8007 (2010).

110. Yamashita, H. *et al.* Newly developed aircraft routing options for air traffic simulation in the chemistry–climate model EMAC 2.53: AirTraf 2.0. *Geoscientific Model Development* **13,** 4869–4890 (2020).

111. Eurocontrol. in *EEC Technical/Scientific Report* (2011).

112. ICAO. in *Technical report, Doc 9646-AN/943* (2005).

113. Schaefer, M. Development of forecast model for global air traffic emissions (2012).

114. Deidewig, S., Döpelheuer, A. & Lecht, M. Methods to assess aircraft engine emissions in flight. *ICAS PROCEEDINGS,* 131–141 (1996).

115. Sasaki, D., Obayashi, S. & Nakahashi, K. Navier-Stokes Optimization of Supersonic Wings with Four Objectives Using Evolutionary Algorithm. *Journal of Aircraft* **39,** 621–629 (2002).

116. Sasaki, D. & Obayashi, S. Development of efficient multiobjective evolutionary algorithms: ARMOGAs (adaptive range multi-objective genetic algorithms). **16,** 11–18 (2004).

117. Sasaki, D. & Obayashi, S. Efficient Search for Trade-Offs by Adaptive Range Multi-Objective Genetic Algorithms. *Journal of Aerospace Computing, Information, and Communication* **2,** 44–64 (2005).

118. Yamashita, H. *et al.* Towards Climate Optimized Flight Trajectories in a Climate Model: AirTraf. *USA/Europe Air Traffic Management Research and Development Seminar* (2015).

119. Mlawer, E. J., Taubman, S. J., Brown, P. D., Iacono, M. J. & Clough, S. A. Radiative transfer for inhomogeneous atmospheres: RRTM, a validated correlated-k model for the longwave. *Journal of Geophysical Research: Atmospheres* **102,** 16663–16682. ISSN: 0148-0227 (1997).

120. Bonnel, Y. F. B. Computations of solar heating of the Earth's atmosphere: A new parameterization. *Beitr. Phys. Atmos.* **53,** 35–62 (1980).

121. Nissen, K. M., Matthes, K., Langematz, U. & Mayer, B. Towards a better representation of the solar cycle in general circulation models. *Atmospheric Chemistry and Physics* **7,** 5391–5400. ISSN: 1680-7324 (2007).

122. Dahlmann, K., Grewe, V., Ponater, M. & Matthes, S. Quantifying the contributions of individual NOx sources to the trend in ozone radiative forcing. *Atmospheric Environment* **45,** 2860–2868 (2011).

123. Mertens, M., Grewe, V., Rieger, V. S. & Jöckel, P. Revisiting the contribution of land transport and shipping emissions to tropospheric ozone. *Atmospheric Chemistry and Physics* **18,** 5567–5588 (2018).

124. Yin, F. *et al.* Verification of the ozone algorithmic climate change functions for predicting the short-termNOx effects from aviation en-route. *ICRAT 2018* (2018).

125. Deckert, R., Jöckel, P., Grewe, V., Gottschaldt, K.-D. & Hoor, P. A quasi chemistry-transport model mode for EMAC. **4,** 195–206 (2011).

126. Dee, D. P. *et al.* The ERA-Interim reanalysis: configuration and performance of the data assimilation system. *Quarterly Journal of the Royal Meteorological Society* **137,** 553–597 (2011).

127. Grewe, V. *et al.* Origin and variability of upper tropospheric nitrogen oxides and ozone at northern mid-latitudes. *Atmospheric Environment* **35,** 3421–3433 (2001).

128. ECMWF. *ECMWF | Parameter details* https://apps.ecmwf.int/codes/grib/param-db/?id=171156.

129. Weisstein, E. *Vector norm* https://mathworld.wolfram.com/VectorNorm.html.

130. Grewe, V., Dameris, M., Fichter, C. & Lee, D. S. Impact of aircraft NOx emissions. Part 2: Effects of lowering the flight altitude. *Meteorologische Zeitschrift* **11,** 197–205 (2002).

131. Castino, F. *et al. Seasonal Variability of Aircraft Trajectories reducing NO_x-climate Impacts under a Multitude of Weather Patterns* in (Paper presented at 11th SESAR Innovation Days., 2021).

132. Lührs, B., Linke, F., Matthes, S., Grewe, V. & Yin, F. Climate Impact Mitigation Potential of European Air Traffic in a Weather Situation with Strong Contrail Formation. *Aerospace* **8,** 50. ISSN: 2226-4310 (2021).

133. Matthes, S. *et al.* Mitigation of Non-CO2 Aviation's Climate Impact by Changing Cruise Altitudes. *Aerospace* **8,** 36. ISSN: 2226-4310 (2021).

134. Rao, P. *et al.* The ozone radiative forcing of nitrogen oxide emissions from aviation can be estimated using a probabilistic approach. *Communications Earth & Environment*. Under review (2023).

135. Maruhashi, J., Grewe, V., Frömming, C., Jöckel, P. & Dedoussi, I. C. Transport patterns of global aviation NO_x and their short-term O_3 radiative forcing –a machine learning approach. *Atmospheric Chemistry and Physics* **22,** 14253–14282 (2022).

136. Maruhashi, J., Mertens, M., Grewe, V. & Dedoussi, I. C. A multi-method assessment of the global influence of flight altitude on the short-term climate warming from aircraft NO_x emissions. Under review (2023).

137. Telford, P. J., Braesicke, P., Morgenstern, O. & Pyle, J. A. Technical Note: Description and assessment of a nudged version of the new dynamics Unified Model. *Atmospheric Chemistry and Physics* **8,** 1701–1712. https://acp.copernicus.org/articles/8/1701/2008/ (2008).

138. Saul, A. D., Hensman, J., Vehtari, A. & Lawrence, N. D. *Chained Gaussian Processes* in *Proceedings of the 19th International Conference on Artificial Intelligence and Statistics* **51** (PMLR, Cadiz, Spain, 2016), 1431–1440. https://proceedings.mlr.press/v51/saul16.html.

139. Dahlmann, K., Grewe, V., Matthes, S. & Yamashita, H. Climate assessment of single flights: Deduction of route specific equivalent COsub2/sub emissions. *International Journal of Sustainable Transportation* **17,** 29–40 (2023).

140. Neal, R. M. *Monte Carlo Implementation of Gaussian Process Models for Bayesian Regression and Classification* 1997.

141. Rue, H., Martino, S. & Chopin, N. Approximate Bayesian Inference for Latent Gaussian models by using Integrated Nested Laplace Approximations. *Journal of the Royal Statistical Society Series B: Statistical Methodology* **71,** 319–392 (2009).

142. Opper, M. & Archambeau, C. The Variational Gaussian Approximation Revisited. *Neural Computation* **21,** 786–792 (2009).

143. Hernández-Lobato, D. & Hernández-Lobato, J. M. *Scalable Gaussian Process Classification via Expectation Propagation* 2015.

144. Lloyd, S. Least squares quantization in PCM. *IEEE Transactions on Information Theory* **28,** 129–137 (1982).

145. Matthews, A. G. d. G. *et al.* GPflow: A Gaussian process library using TensorFlow. *Journal of Machine Learning Research* **18,** 1–6. http://jmlr.org/papers/v18/16-537.html (2017).

146. Scott, D. W. *Multivariate Density Estimation* (Wiley, 1992).

147. Gray, L. J. *et al.* Solar influences on climate. *Reviews of Geophysics* **48** (2010).

148. Kullback, S. & Leibler, R. A. On Information and Sufficiency. *The Annals of Mathematical Statistics* **22,** 79–86 (1951).

149. Matthes, S. *et al.* Climate-Optimized Trajectories and Robust Mitigation Potential: Flying ATM4E. *Aerospace* **7,** 156 (2020).

150. Yamashita, H. *et al.* Analysis of Aircraft Routing Strategies for North Atlantic Flights by Using AirTraf 2.0. *Aerospace* **8,** 33 (2021).

151. Bickel, M., Ponater, M., Bock, L., Burkhardt, U. & Reineke, S. Estimating the Effective Radiative Forcing of Contrail Cirrus. *Journal of Climate* **33,** 1991–2005 (2020).

152. Tenenbaum, J. B. A Global Geometric Framework for Nonlinear Dimensionality Reduction. *Science* **290,** 2319–2323 (2000).

153. Wang, Y., Yao, H. & Zhao, S. Auto-encoder based dimensionality reduction. *Neurocomputing* **184,** 232–242 (2016).

154. Zhou, X.-H., Han, J. & Xiao, H. Learning nonlocal constitutive models with neural networks. *Computer Methods in Applied Mechanics and Engineering* **384,** 113927 (2021).

155. Simorgh, A. *et al.* Robust 4D climate-optimal flight planning in structured airspace using parallelized simulation on GPUs: ROOST V1.0. *Geoscientific Model Development* **16,** 3723–3748. ISSN: 1991-9603 (2023).

156. Scott, D. W. Scott's' rule. *Wiley Interdisciplinary Reviews: Computational Statistics* **2,** 497–502 (2010).

157. Smith, R. C. *Uncertainty Quantification: Theory, Implementation, and Applications* (ed Estep, D.) (SIAM - Computational Science & Engineering, 2013).

158. Winterstein, F. & Jöckel, P. Methane chemistry in a nutshell – the new submodels CH4 (v1.0) and TRSYNC (v1.0) in MESSy (v2.54.0). *Geoscientific Model Development* **14,** 661–674. https://gmd.copernicus.org/articles/14/661/2021/ (2021).

159. Tost, H. *Global Modelling of Cloud, Convection and Precipitation Influences on Trace Gases and Aerosols* PhD thesis (University of Bonn, 2006).

160. Tost, H., Jöckel, P. & Lelieveld, J. Influence of different convection parameterisations in a GCM. *Atmospheric Chemistry and Physics* **6,** 5475–5493 (2006).

161. Kerkweg, A. *et al.* Technical Note: An implementation of the dry removal processes DRY DEPosition and SEDImentation in the Modular Earth Submodel System (MESSy). *Atmospheric Chemistry and Physics* **6,** 4617–4632 (2006).

162. Sander, R. *et al.* The photolysis module JVAL-14, compatible with the MESSy standard, and the JVal PreProcessor (JVPP). *Geoscientific Model Development* **7,** 2653–2662 (2014).

163. Tost, H., Jöckel, P. & Lelieveld, J. Lightning and convection parameterisations – uncertainties in global modelling. *Atmospheric Chemistry and Physics* **7,** 4553–4568 (2007).

164. Grewe, V. The origin of ozone. *Atmospheric Chemistry and Physics* **6,** 1495–1511 (2006).

165. Kerkweg, A., Sander, R., Tost, H. & Jöckel, P. Technical note: Implementation of prescribed (OFFLEM), calculated (ONLEM), and pseudo-emissions (TNUDGE) of chemical species in the Modular Earth Submodel System (MESSy). *Atmospheric Chemistry and Physics* **6,** 3603–3609 (2006).

166. Tost, H., Jöckel, P., Kerkweg, A., Sander, R. & Lelieveld, J. Technical note: A new comprehensive SCAVenging submodel for global atmospheric chemistry modelling. *Atmospheric Chemistry and Physics* **6,** 565–574 (2006).

Acknowledgements

While I am quite happy about this relatively short dissertation, it would have not been possible without the invaluable help of numerous people. Thus, I would like to extend my gratitude to all those who have supported me and I apologise in advance if I inadvertently overlook anyone.

First and foremost, I would like to thank my promotor, Volker, who selected me for this position and trusted me despite not having experience in climate science. Your positive and proactive approach, encouragement to pursue ambitious goals, and meticulous nature have not only shaped me into a better researcher and communicator but has also inspired me to continue contributing to the field of climate science. I am extremely grateful to my second promoter, Richard, for stepping in at a crucial moment and enriching my research. Your creativity and competence are second to none. Your informal demeanor, open-mindedness, and great sense of humour made the research atmosphere both productive and enjoyable— a dynamic I will sincerely miss. Special thanks are also due to all the partners of the EU horizon 2020 project, ClimOP, without whom this research would not have been possible. I would also like to thank Deepali for helping me with Gaussian processes (among many other things) and Patrick Jöckel, Hiroshi and Christine for their expertise in EMAC-related queries.

I am highly indebted to Dick for his exceptional role as the head of section during a pivotal phase of my PhD journey. Your decision-making and belief in my abilities were instrumental in helping me overcome the biggest challenges and staying focused on my research goals. In line with this, I would like to thank Laurike for being so kind, understanding, empathetic, and resourceful. We are all so lucky to have you in the Graduate school! I would also like to thank my mentor Bas, everyone at the service desk (Michiel, Eric, Paul, Franciscus, Aytac) for my annoying requests, and of course, my BSc students (Alessandro, Carmelo, Filip, Jeroen, Kristian, Lucille, Lynn, Mathijs, Simen, and Yoari), all of whom I have learnt from.

I would like to thank my wonderful peers at ANCE. More specifically, thank you Irene for the great advice and pleasant conversations, work-related or otherwise. I would also like to thank: Irina for being the best office mate ever; Bieke for always being so helpful and kind to me; Jin for patiently giving me so much data, and for those fun lunches; Kathrin for the Linux help and simplicity; Anique for the engaging Dutch conversations and summary translation; Federica for being a patient listener and saying the funniest Italian things; Flávio for all the help with this LaTeXtemplate; Camilo for the nerdy and light conversations; Anandini for the laughter; Andrei for being the second-best Romanian, Jurriaan for being so cool; Salil for the positive vibes and helping me pick the right gym; Luca for the nice coffee and car rides to work; Rebekka for the nice beer recommendations; Harjot for the great lemon rice; Furkat for the academic advice; and Lisette for sharing cute stories, your lunch, and of course, a nice book.

Finally, I would like to thank my family and friends, all over the world, for their unconditional love and support, while keeping me grounded. Thank you for sharing this journey with me and making it as beautiful as possible.

Pratik Vijay Rao
Delft, March 2024

Curriculum Vitæ

Pratik Vijay Rao

07-08-1992 Born in Bangalore, India.

Education

2009–2011 Pre-University
St. Joseph's Pre-University College
Bangalore, India

2011–2015 Bachelor of Engineering in Mechanical Engineering
R. V. College of Engineering
Bangalore, India

2015–2018 Master of Science in Aerospace Engineering
Delft University of Technology
Delft, the Netherlands
Thesis: Application of the Mixed and Hybrid Finite Element Formulations.
Promotor: dr. M. I. Gerritsma

2019–2024 Doctor of Philosophy (Ph.D.) in Aerospace Engineering
Delft University of Technology
Delft, the Netherlands
Thesis: Verifying and improving the estimation of NO_x-O_3 effects of aviation using Uncertainty Quantification (UQ) techniques
Promotors: Prof. dr. V. Grewe and dr. R. P. Dwight

Professional experience

2018-2019 Junior FEM analyst
VIRO
Vlaardingen, the Netherlands

List of Publications

Peer reviewed journals

3. **P. Rao**, R. P. Dwight, D. Singh, J. Maruhashi, I. C. Dedoussi, V. Grewe, C. Frömming. *The ozone radiative forcing of nitrogen oxide emissions from aviation can be estimated using a probabilistic approach*, under peer review, Communications Earth & Environment (2023).

2. F. Yin, V. Grewe, F. Castino, **P. Rao**, S. Matthes, K. Dahlmann, S. Dietmüller, C. Frömming, H. Yamashita, P. Peter, E. Klingaman, K. P. Shine, B. Lührs, F. Linke, *Predicting the climate impact of aviation for en-route emissions: the algorithmic climate change function submodel ACCF 1.0 of EMAC 2.53*, Geoscientific Model Development **16**, 11 (2023).

1. **P. Rao**, F. Yin, V. Grewe, H. Yamashita, P. Jöckel, S. Matthes, M. Mertens, C. Frömming. *Case Study for Testing the Validity of NO_x-Ozone Algorithmic Climate Change Functions for Optimising Flight Trajectories*, Aerospace **9**, 5 (2022).

Conference contributions

4. **P. Rao**, R. P. Dwight, D. Singh, J. Maruhashi, I. C. Dedoussi, V. Grewe, C. Frömming. *Towards a new surrogate model for predicting short-term NO_x-O_3 effects from aviation using Gaussian processes*, EGU General Assembly 2023, Vienna, 23-28 April 2023.

3. **P. Rao**, F. Yin, V. Grewe, H. Yamashita, P. Jöckel, S. Matthes, M. Mertens, C. Frömming. *The analysis of the climate mitigation potential in terms of O_3-Radiative Forcing from aviation NO_x using O_3 algorithmic climate change functions*, EGU General Assembly 2022, Vienna, 23-27 May 2022.

2. **P. Rao**, F. Yin, V. Grewe, H. Yamashita, P. Jöckel. *The analysis of NO_x-ozone effects from optimised air-traffic using algorithmic climate change functions*, 11^{th} EASN Virtual Conference, Virtual, 1-3 September 2021.

1. **P. Rao**, F. Yin, V. Grewe, H. Yamashita, P. Jöckel. *The use of NO_x-O_3 algorithmic climate change functions for air-traffic optimisation*, 10th EMAC Symposium, Virtual, 31^{st} May to 2^{nd} June 2021.